



CM-P00068868

---

# Calibration and Monitoring of Microstrip Gas Chambers in CMS

---

Dissertation

zur Erlangung des akademischen Grades

Doktor rer. nat.

der formal- und naturwissenschaftlichen Fakultät

der Universität Wien

eingereicht von

Mag. rer. nat. Roman Malina

Genf, im Mai 1999

Thesis-1999-Malina

## Deutsche Kurzfassung der Dissertation

Im Jahr 2005 soll am CERN der  $7 + 7 \text{ TeV}$  Proton-Proton Beschleuniger LHC (Large Hadron Collider) in Betrieb gehen, auf der Suche nach dem Higgs-Teilchen und eventuellen supersymmetrischen Teilchen. Eines der für LHC geplanten Experimente, CMS (Compact Muon Solenoid), implementiert zur Spurrekonstruktion MicroStrip Gas Chambers (MSGCs) in seinem Vertexdetektor, in Kombination mit Silizium Pixel- und Streifendetektoren.

MSGCs sind Gasdetektoren nach dem Prinzip von Vieldrahtproportionalkammern, wobei Anoden und Kathoden als alternierende Goldstreifen auf einem Glassubstrat ausgebildet sind. Mit einem Anoden-Anoden Abstand von  $200 \mu\text{m}$  kann mit dieser Technologie eine Ortsauflösung besser als  $35 \mu\text{m}$  erreicht werden, bei einer im Vergleich zu Halbleiterdetektoren geringeren Anzahl von Auslesekanälen. Ungefähr  $5 \cdot 10^6$  Kanäle über eine aktive Fläche von  $225 \text{ m}^2$  sind in CMS vorgesehen.

Die Herausforderungen beim Einsatz von MSGCs in CMS sind vielseitig. Um die notwendige Detektionseffizienz zu erlangen ist ein hohes Signal/Rauschverhältnis  $S/R > 20$  erforderlich, welches wegen der hohen Teilchenstrahlkollisionsrate von  $40 \text{ MHz}$  in LHC mit einer Elektronik mit kurzer Signalformationszeit erreicht werden muß. Eine Teilchendichte von circa  $5 \text{ kHz/mm}^2$  muß von den Detektoren bewältigt werden. Die in dem Teilchenspektrum enthaltenen Kernfragmente können dabei derart hohe Ionisationsdichten im Detektorgas verursachen, daß es zwischen den Kathoden und Anoden zu Entladungen kommen kann. Diese können die Anoden, die eine Breite von nur  $7 \mu\text{m}$  und eine Dicke von  $0.6 \mu\text{m}$  haben, beschädigen. Es ist essentiell, die Anfälligkeit der MSGCs für solche Beschädigungen zu minimieren.

Die vorliegende Arbeit, die im Rahmen der CERN CMS Tracker Kollaboration durchgeführt wurde, hat zwei Schwerpunkte. Im ersten wurden im Labor und in Teststrahlen (CERN und PSI) die Eigenschaften der MSGCs untersucht und die Parameter festgelegt, die den optimalen Arbeitspunkt der MSGC im Einsatz in CMS darstellen. Weiters wurde die Häufigkeit obiger Entladungen und die Robustheit der MSGCs in einem Teilchenstrahl mit einem Spektrum ähnlich dem bei LHC zu erwartenden ermittelt. Der zweite Teil der Arbeit bestand in der Konzeption und Verwirklichung einer Reihe von Testsystemen, mit deren Hilfe alle 5540 Detektormodule, die in den folgenden Jahren gefertigt werden, getestet werden können, bevor sie in CMS zum Einsatz kommen. Ein Teil der dabei gewonnenen Daten wird in die CMS online Datenbank aufgenommen, um beim laufenden Experiment die Eventrekonstruktion und Datenanalyse zu verbessern.

## Abstract

In the year 2005 the  $7+7$   $TeV$  proton-proton accelerator LHC (Large Hadron Collider) at CERN will embark on the search for the Higgs particle and possible supersymmetric particles. One of the experiments designed for LHC, CMS (the Compact Muon Solenoid), employs MicroStrip Gas Chambers (MSGC's) in its inner tracker, combined with silicon strip- and pixel detectors.

MSGC's are gaseous detectors similar to multiwire proportional chambers, with gold-strips (anodes and cathodes) taking the role of the sense wires and the cathode planes, respectively. With a distance from anode to anode of  $200 \mu m$  a resolution better than  $35 \mu m$  can be obtained, with a relatively low number of read-out channels when compared to semiconductor detectors. The MSGC's in CMS will cover an active area of  $225 m^2$  with around  $5 \cdot 10^6$  read-out channels.

Using MSGC's in CMS is a big challenge. In order to achieve the required detection efficiency, a signal-to-noise ratio of  $S/N > 20$  is necessary and has to be obtained from an electronics with a short shaping time that is capable of digesting the high bunch crossing frequency of  $40 MHz$  at LHC.

The chambers are exposed to a particle flux of around  $5 kHz/mm^2$ . Nuclear fragments present in this radiation environment can generate ionization densities in the gas which are high enough to trigger discharges between anodes and cathodes in the MSGC. It is of primary importance to optimize the resistance of the chambers to damage of the anodes which have a width of only  $7 \mu m$  and a thickness of  $0.6 \mu m$ .

The work presented here was done within the CERN CMS tracker collaboration and concentrates on two main topics. In the first one the properties of MSGC's were explored in the laboratory and in beam tests (CERN and PSI) and the parameters that represent the optimal working point of the MSGC's in CMS were defined. The frequency of the above mentioned discharges and the robustness of the MSGC's were investigated in a beam with a particle spectrum similar to what is expected at LHC. The second topic was the design and development of a series of testing systems, which are capable of testing all 5540 MSGC modules that will be produced in the coming years before being mounted into the tracker structure. Part of the measured parameters will be stored in the CMS online database, in order to optimize event reconstruction and data analysis once the experiment is running.

# Contents

<b>1</b>	<b>Introduction</b>	<b>1</b>
<b>2</b>	<b>Physics at 14 TeV pp Collisions</b>	<b>4</b>
2.1	The Standard Model . . . . .	4
2.1.1	QCD and QED . . . . .	5
2.1.2	Spontaneous Symmetry Breaking . . . . .	6
2.1.3	B physics . . . . .	9
2.2	Beyond the Standard Model . . . . .	10
2.2.1	The Minimal Supersymmetric Model . . . . .	10
2.2.2	The MSSM Higgs Sector . . . . .	10
2.3	Heavy Ion Physics . . . . .	11
<b>3</b>	<b>LHC and CMS</b>	<b>13</b>
3.1	LHC . . . . .	13
3.1.1	The Accelerator Chain . . . . .	14
3.1.2	7+7 TeV . . . . .	14
3.1.3	Experiments at LHC . . . . .	17
3.2	CMS . . . . .	19
3.2.1	Inner Tracker . . . . .	20

<b>CONTENTS</b>	<b>5</b>
3.2.2 Electromagnetic Calorimeter . . . . .	20
3.2.3 Hadronic Calorimeter . . . . .	21
3.2.4 Muon System . . . . .	22
3.2.5 Magnet . . . . .	23
3.2.6 Trigger . . . . .	24
<b>4 The CMS Inner Tracker</b>	<b>25</b>
4.1 Silicon Pixel . . . . .	26
4.2 Silicon Strip . . . . .	27
4.3 Microstrip Gas Chambers . . . . .	28
4.4 Performance of the tracker . . . . .	30
<b>5 Microstrip Gas Chambers</b>	<b>33</b>
5.1 Working Principle of Gaseous Detectors . . . . .	33
5.1.1 The Ionisation Process . . . . .	34
5.1.2 Drift of Electrons . . . . .	36
5.1.3 Charge Amplification . . . . .	37
5.2 The detecting elements . . . . .	39
5.3 The Electronics . . . . .	43
5.3.1 The High Voltage Part . . . . .	43
5.3.2 The Read-Out Chain . . . . .	44
5.4 Analysis of MSGC Signals . . . . .	46
5.5 Basic Performance of the MSGC . . . . .	47
5.5.1 Gain of the MSGC: $\text{gain}(V_c, V_d, Ne\%)$ . . . . .	47
5.5.2 Signal variations with pressure . . . . .	50

<i>CONTENTS</i>	6
5.5.3 Mechanical deformation due to over-pressure . . . . .	52
5.5.4 Effects of high rates . . . . .	53
5.5.4.1 Reduction of gain due to 'charging up' . . . . .	54
5.5.4.2 Reduction of gain due to 'aging' . . . . .	54
5.6 Performance in test beams . . . . .	56
5.6.1 Operation in the LHC environment . . . . .	57
<b>6 Quality Control System</b>	<b>62</b>
6.1 Cosmics telescope . . . . .	64
6.1.1 Description of the Cosmics Set-up . . . . .	64
6.1.2 The testing procedure . . . . .	67
6.1.3 Radioactive Gas . . . . .	69
6.2 XY-Table . . . . .	72
6.2.1 Description of the XY-Table . . . . .	73
6.2.2 The testing procedure . . . . .	75
6.2.3 Results of a test . . . . .	78
6.3 Rod Test Stand . . . . .	82
6.3.1 Description of the Rod Test Stand . . . . .	83
6.3.2 Alignment Capabilities of the Rod Test Stand . . . . .	84
6.4 Pulsing . . . . .	85
6.4.1 Calibration of the Read-out Electronics . . . . .	86
6.5 Summary of Calibration . . . . .	88
<b>7 Conclusions</b>	<b>92</b>
<b>8 Acknowledgements</b>	<b>94</b>

<i>CONTENTS</i>	7
<b>A Appendix</b>	<b>95</b>
A.1 Accelerator Physics . . . . .	96
A.1.1 The beta function $\beta(s)$ . . . . .	96
A.1.2 The emittance $\epsilon$ . . . . .	97
A.2 Minimum gain required for MSGC's in CMS . . . . .	97
A.3 The over-pressure valve . . . . .	98
A.4 Gain Dependence on $V_{cathode}$ and $V_{drift}$ . . . . .	99

# List of Figures

2.1	Total Higgs width . . . . .	7
2.2	Overview of the SM Higgs observability . . . . .	7
2.3	Discovery potential for a SUSY Higgs . . . . .	11
3.1	Cross section of an LHC dipole . . . . .	15
3.2	Integrated particle fluxes . . . . .	17
3.3	Schematic layout of the LHC . . . . .	18
3.4	The CMS detector . . . . .	19
4.1	The CMS Inner Tracker . . . . .	25
4.2	Charge sharing due to a non-zero Lorentz angle . . . . .	27
4.3	The rod concept . . . . .	29
4.4	A $10 \times 25 \text{ cm}^2$ MSGC module . . . . .	30
4.5	Number of layers versus rapidity . . . . .	32
5.1	Experimental cluster size distribution for Argon . . . . .	34
5.2	Estimates of $I$ for some elements . . . . .	36
5.3	Correction of the Lorentz angle . . . . .	37
5.4	Cross section of an MSGC module . . . . .	39
5.5	The electric field in an MSGC . . . . .	40



5.6	The patterning technique . . . . .	41
5.7	Detail of the micro pattern structure . . . . .	42
5.8	Currents spikes measured during operation . . . . .	43
5.9	The resistive network supplying high voltage . . . . .	44
5.10	Schematic picture of the PreMux electronics and read-out chain . . . . .	45
5.11	The schematic circuit of the PreMux . . . . .	46
5.12	Cross-talk between strips . . . . .	47
5.13	The read-out of the anode strips . . . . .	48
5.14	Gain in a Ne/DME=33/67 mixture . . . . .	49
5.15	Dependence of gain on the Ne% . . . . .	50
5.16	Read-out logic of the $3 \times 3 \text{ cm}^2$ MSGC . . . . .	51
5.17	The pressure control system . . . . .	52
5.18	Deformation of the MSGC due to over-pressure . . . . .	53
5.19	The linear behaviour of the deformation . . . . .	54
5.20	Charging up of the substrate . . . . .	55
5.21	Aging behaviour over several years . . . . .	56
5.22	Average cluster size as a function of the Neon concentration . . . . .	57
5.23	Hit efficiency . . . . .	58
5.24	Signal/Noise ratio . . . . .	59
5.25	Spatial resolution of the MSGCs . . . . .	60
5.26	Onset of discharges at high voltages . . . . .	60
5.27	Beam profile of the $350 \text{ MeV } \pi^+$ beam . . . . .	61
5.28	Voltage scan under LHC conditions . . . . .	61
6.1	Schematic view of the cosmos rack . . . . .	65

<i>LIST OF FIGURES</i>	10
6.2 The gas mixing system . . . . .	66
6.3 Automatic gas distribution system . . . . .	67
6.4 Mechanical gas interlock . . . . .	68
6.5 Cosmics test stand, graphical protocol . . . . .	69
6.6 Energy loss spectrum of Kr <sup>83</sup> . . . . .	70
6.7 Simulated signal after pre-amplification and shaping . . . . .	71
6.8 Energy deposited by a MIP . . . . .	72
6.9 XY-table – principle of operation . . . . .	73
6.10 Schematic layout of the XY-table test system . . . . .	73
6.11 The XY-Table with a 10 × 25 cm <sup>2</sup> module . . . . .	75
6.12 Signal and noise of a single strip . . . . .	77
6.13 Gain uniformity of an MSGC . . . . .	79
6.14 Number of particle hits per strip . . . . .	80
6.15 Mechanically deformed module . . . . .	81
6.16 Gain non-uniformity of a mechanically deformed module . . . . .	82
6.17 Field configuration with a floating strip . . . . .	83
6.18 Effect of Fig. 6.17 on detection efficiency . . . . .	84
6.19 The measurement of the rod impedance . . . . .	85
6.20 Schematic layout of the alignment measurement . . . . .	86
6.21 Spatial extension of the area irradiated by the Sr <sup>90</sup> source . . . . .	87
6.22 Pulsing of an anode strip . . . . .	88
6.23 Block diagram of the pulsing setup . . . . .	89
6.24 Response of strips to pulsing . . . . .	89
6.25 Detection of non-functioning strips . . . . .	90

<i>LIST OF FIGURES</i>	11
6.26 Pulse height distribution . . . . .	90
6.27 Calibration of the pulsing setup . . . . .	91
6.28 Calibration of the read-out electronics . . . . .	91
A.1 One simulated LHC bunch crossing . . . . .	95
A.2 $10 \times 10 \text{ cm}^2$ MSGC prototype . . . . .	96
A.3 A particle in an accelerator . . . . .	96
A.4 The over-pressure valve . . . . .	98
A.5 Legend for Fig. 5.14, A.6 and A.7 . . . . .	99
A.6 Gain in Ne/DME mixtures with Ne=25, 42 and 50 % . . . . .	100
A.7 Gain in Ne/DME mixtures with Ne=58, 67 and 75 % . . . . .	101

# Chapter 1

## Introduction

- ) **Particles :**

400 B.C. Democrit brought up the notion of the indivisible entity, the 'atomos'. To date 6 leptons and 6 quarks and the corresponding anti-particles are known as the elementary particles. Are they really the fundamental building blocks of matter ?

- ) **Forces :**

More than 100 years ago Maxwell united electrical and magnetic forces into a common theory. The Standard Model is today an extensively tested theory, and unites electromagnetism, the weak and the strong force. So what about a theory that could eventually incorporate gravity ?

- ) **Symmetries :**

Symmetry relations express the beauty of field theory. Should not every fermionic 'matter-particle' have a bosonic counterpart and should every bosonic force mediating particle have an associated fermionic particle ?

Such are the questions that keep particle physicists busy to date. At CERN, the European laboratory for particle physics <sup>1</sup>, a  $7 + 7 TeV$  proton-proton accelerator – the Large Hadron Collider, LHC – is under construction, and several experiments will look for answers to these questions from the year 2005 onwards.

But the predominant question addresses the well established Standard Model itself. Why do particles have a mass ? One attempt of an answer within the Standard Model is that of spontaneous symmetry breaking. This formalism can give a qualitative explanation. But it also predicts a hitherto unobserved particle, the Higgs-particle. It is the main goal of two of the experiments proposed for LHC to detect this particle.

---

<sup>1</sup>CERN – the 'Centre Europeenne pour la Recherche Nucleaire' in Geneva

As a Doctoral Student at CERN I had the opportunity to work on the preparation of one of these experiments, CMS, the Compact Muon Solenoid. Like most collider experiments it is a cylindrical 'onion'. That is, it combines different detector technologies in concentric layers. The innermost part is the tracker, designed to reconstruct the tracks of particles originating from the collisions. From these tracks the momentum of the particles can be calculated as well as the point from where they came from, i.e. the decay vertices.

The CMS tracker is made with three different detector technologies, the outermost and biggest part consisting of MicroStrip Gas Chambers (MSGCs). These are a few  $mm$  thin gaseous detectors similar to multiwire proportional chambers, with the difference that the wires and cathode planes are represented by anode and cathode gold strips which are etched onto a glass substrate. This allows to space the sensing elements more tightly and thus increase the rate capability of the device.

Indeed, the biggest challenge at LHC will be its extreme particle production rate necessary due to the rareness of the physics processes of interest. The bunch crossings will produce several thousands of particles every  $25\text{ ns}$ . This requires the CMS tracker to be very finely grained, resulting in  $\sim 10^7$  read-out channels covering a surface of  $\sim 300\text{ m}^2$ . In the barrel, the central region,  $\sim 5000$   $10 \times 25\text{ cm}^2$  big MSGC modules will be employed.

Due to the resulting high radiation environment, access to the detector will be very limited once LHC has started. In particular it will not be possible to easily gain access to the detector during a period of shutdown in order to replace some components. Thus, all the employed technologies have to work with very high reliability. This not only poses stringent requirements on the detector technologies themselves but also demands a sophisticated chain of quality control and test stations. Due to the large number of elements to be tested, these have to work in a fully automated way and must minimise user intervention.

Following these lines, the content of this thesis is twofold. In the first part the MSGC technology is described. Measurements taken in the laboratory establish the functional dependence of the gain of the CMS MSGC prototypes as a function of the applied voltages and the used gas mixture, and investigate gain variation due to pressure fluctuations and mechanical deformations of the modules. Long-term studies of aging and charging up under high rates are quoted. By participating in various beam tests the behaviour of the MSGCs under LHC-like irradiation was studied, concentrating on the robustness of this technology against heavily ionising particles.

In the second part the question of quality control and calibration of the MSGCs is addressed. By 'calibration' we mean the determination of the parameters related to the performance of the MSGCs and the creation of a database for all  $\sim 5000$  modules which can be used for optimising the tracker performance by taking into account the specific characteristics of each MSGC. An ensemble of test benches were designed that can measure these parameters and ensure the functionality of every single MSGC module. Their design and performance is described.

The following chapter will give an overview of the physics that can be investigated at LHC. Chapter 3 describes LHC itself and mentions the different sub-detectors of CMS. Chapter 4 gives more details on the inner tracker of CMS, of which the MSGC tracker is part of. Chapter 5 and 6 represent the main part of the thesis and deal with the properties and performance of the MSGCs and with the test and calibration setup designed for these chambers, respectively. The conclusions in chapter 7 summarize the results obtained in this work.

# Chapter 2

## Physics at 14 TeV pp Collisions

The questions that the LHC and its experiments will try to answer are diverse, and address on the one hand open issues of the Standard Model, foremost the origin of mass, i.e. the mechanism of spontaneous symmetry breaking, but also the properties of the top quark and CP-violation in B-meson decays, and on the other hand try to probe the particle spectrum for e.g. supersymmetry, heavy gauge bosons or further quark/lepton families.

### 2.1 The Standard Model

The Standard Model, combining QCD and the electroweak model [1, 2] describes the interactions of all particles with the electromagnetic, weak and strong force [3]. It features a Lagrange density, which, neglecting chirality, has the structure

$$\mathcal{L} = \bar{\psi}i\gamma^\mu D_\mu\psi - m\bar{\psi}\psi - \frac{1}{4}F_{\mu\nu}F^{\mu\nu}. \quad (2.1)$$

Here  $\psi$  represents the fermions and stands for  $u = (u, c, t)$ ,  $d = (d, s, b)$ ,  $l = (e, \mu, \tau)$  and  $\nu = (\nu_e, \nu_\mu, \nu_\tau)$ .  $D_\mu\psi := (\partial_\mu + ieA_\mu)\psi$  is the covariant derivative and  $ieF_{\mu\nu} := [D_\mu, D_\nu]$ . In order to introduce mass terms for the gauge bosons (photon, vector bosons and gluons) represented by  $A$ , but maintain a gauge invariant Lagrange density, Higgs and Kibble had to assume that the vacuum was not invariant and created the Higgs field  $\Phi$  with non-vanishing vacuum expectation value  $\langle 0|\Phi|0\rangle = \frac{v}{\sqrt{2}}$ <sup>1</sup>. The interactions

---

<sup>1</sup>Take the simplest case of a  $U(1)$  symmetry. Under a local gauge transformation  $\Phi \rightarrow U^\dagger(\epsilon)\Phi U(\epsilon) = e^{i\epsilon(x)}\Phi$  leaving the vacuum invariant, the vacuum expectation value of  $\Phi$  would change

between the gauge bosons and the Higgs boson and their respective mass terms are then described by a Lagrangian of the form

$$\mathcal{L}_{Higgs} = (D^\mu \Phi^\dagger) (D_\mu \Phi) - \lambda \left( \Phi^\dagger \Phi - \frac{v^2}{2} \right)^2, \quad (2.2)$$

Mass terms for the fermions and interactions between them and the Higgs boson are introduced by adding another part to the Lagrangian, namely

$$\mathcal{L}_{IH} = Y \Phi \bar{\psi} \psi. \quad (2.3)$$

In the *interaction basis* gauge interactions are diagonal, that is, there are no gauge couplings between different fermion generations. In the *mass basis* Yukawa interactions are diagonal, i.e. the mass eigenstates have, by definition, a well defined mass. The Yukawa interactions have the form

$$-\mathcal{L}_Y = Y^d \bar{Q}_L^I \Phi d_R^I + \text{similarly for } u \text{ and } l, \quad (2.4)$$

with  $\Phi$  the SM Higgs doublet and  $Q_L^I = (u_L^I, d_L^I)^t$ . The flavour (or generation) indices  $i, j$  on  $Y_{ij}$ ,  $Q_{Li}$  and  $d_{Rj}$  are being suppressed. Using the unitary gauge  $\frac{1}{\sqrt{2}}R(x) := e^{i\epsilon(x)\tau}\Phi(x)$  eliminates some arbitrary phases and allows us to write the Higgs field in terms of a hermitian field with vanishing vacuum expectation value plus some constant and we obtain mass terms for the fermions,

$$-\mathcal{L}_M = (M_d) \bar{d}_L^I d_R^I + \text{similarly for } u \text{ and } l, \quad (2.5)$$

where  $M = \frac{v}{\sqrt{2}}Y$ .

With two unitary matrices it is always possible to diagonalise the  $M$ 's, that is,  $V_{dL} M_d V_{dR}^\dagger = M_d^{diag}$ . Thus, we obtain the corresponding mass eigenstates  $d_L = (V_{dL}) d_L^I$ .

### 2.1.1 QCD and QED

The top quark.

The top quark was discovered in 1995 at the CDF and D0 experiments at Fermilab's Tevatron collider [4, 5] where a value of  $m_T \sim 180 \text{ GeV}$  was measured.

At  $\sqrt{s} = 14 \text{ TeV}$  the top quark production cross section should be  $\sim 1 \text{ nb}$  which results in the production of around  $10^7 \text{ } t\bar{t}$  per year even at the initial low luminosity phase of as  $\frac{v}{\sqrt{2}} = \langle 0 | \Phi | 0 \rangle = \langle 0 | e^{i\epsilon(x)} \Phi | 0 \rangle = e^{i\epsilon(x)} \frac{v}{\sqrt{2}}$ . Thus, a non-zero  $v$  requires a non-invariant vacuum.



LHC, thus making it relatively easy to measure the top mass with high precision [6]. Additionally, the determination of its decay branching ratios might even reveal physics beyond the standard model.

CMS would measure  $m_T$  via jets or muons coming from the top decay. The necessary fine granularity of the hadronic calorimeter of  $\Delta\eta \times \Delta\Phi = 0.1 \times 0.1$  is provided by CMS. and also the required precision of the muon momentum determination is well feasible.

### CP-violation.

Doing the same operations that led us to Eq. 2.5, the charged current interaction terms can be written explicitly in the mass basis as

$$-\mathcal{L}_{W^\pm} = \frac{g}{\sqrt{2}} \bar{u}_L \gamma^\mu (V_{uL} V_{dL}^\dagger) d_L W_\mu^\pm + \text{h.c.} \quad (2.6)$$

Here we see explicitly the Cabibbo Kobayashi Maskawa matrix  $V_{CKM} := V_{uL} V_{dL}^\dagger$  [7]. It is not diagonal which allows the  $W^\pm$  bosons to couple to quark mass eigenstates of different generations.  $V_{CKM}$  is unique up to a phase for each generation. Requiring it to have the least number of phases possible, one phase  $\delta_{KM}$  remains, which is the source of CP violation in the Standard Model [7].

Unitarity applied to the first and third column of the CKM matrix,  $V_{ud}V_{ub}^* + V_{cd}V_{cb}^* + V_{td}V_{tb}^* = 0$ , can – after appropriate parametrisation – be approximated in the complex plane by the unitarity triangle [8], whose angles  $(\alpha, \beta, \gamma)$  can be determined experimentally. Measuring  $\sin(2\beta)$  is one of the tasks of CMS (see chapter 2.1.3).

## 2.1.2 Spontaneous Symmetry Breaking

If the mechanism of spontaneous symmetry breaking in the electroweak sector is indeed realized in nature, two scenarios can be imagined:

1. The sector is weakly coupled. This is the scenario described before and leads to one or more Higgs bosons on the below-1  $TeV$ -scale.
2. Symmetry breakdown can occur dynamically by means of e.g. strongly interacting fermion-antifermion pairs, with  $v = \langle 0 | \bar{F}F | 0 \rangle \neq 0$  [9]. Possible candidates are the top quark or techniquarks bound by new technicolor interactions. In the latter case these new "composites" are expected to have a mass around 1  $TeV$  [10].

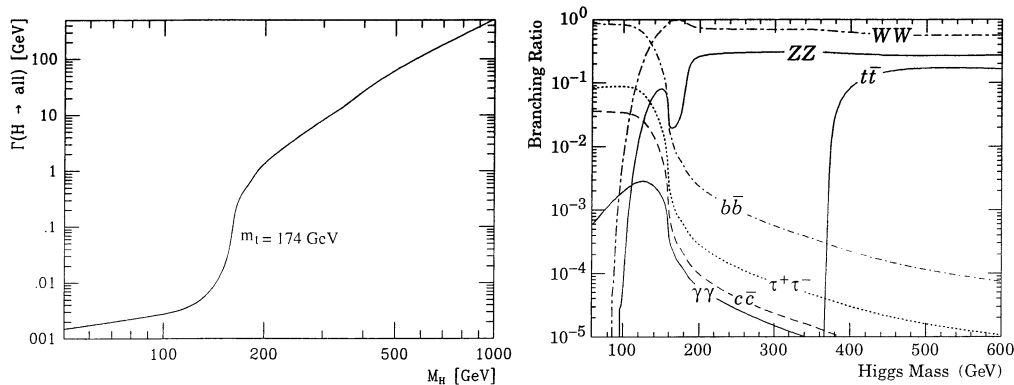


Figure 2.1: Total Higgs width (a) [11] and branching ratios (b) [12] as a function of  $m_H$ .

The Higgs mass enters into electroweak experimental observables through higher order corrections alone, making them only logarithmically sensitive to  $m_H$ . Thus, the standard model does not provide us with a precise prediction of the Higgs mass. An experimental lower bound,  $m_H > 95 \text{ GeV}$ , will be obtained by the LEP experiments before the end of the year,  $m_H \sim 1 \text{ TeV}$  could be inferred as an upper theoretical bound: Bigger values would mean a very large width of the Higgs mass peak,  $\sigma(m_H) \leq 1 \text{ TeV}$ , and would question the interpretation of the Higgs field as a particle.

Table 2.1 gives an overview of the preferred SM-Higgs decay channels as a function of  $m_H$ . CMS has been designed to allow investigations over the entire mass range.

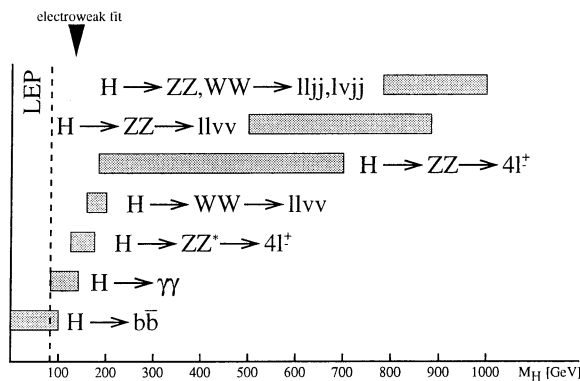


Figure 2.2: Overview of the SM Higgs observability in CMS. The  $m_H$  range below  $95 \text{ GeV}$  will be covered by LEP. A fit to the current electroweak parameters favours a Higgs mass around  $130 \text{ GeV}$ .

Table 2.1: Higgs decay channels for different ranges of  $m_H$ .

mass		main decay channel
	$m_H < 100 \text{ GeV}$	$H \rightarrow b\bar{b}$
$80 \text{ GeV} < m_H < 140 \text{ GeV}$		$H \rightarrow \gamma\gamma$
$120 \text{ GeV} < m_H < 2 m_Z$		$H \rightarrow ZZ^* \rightarrow 4l$
$2 m_Z < m_H < 1 \text{ TeV}$		$H \rightarrow ZZ \rightarrow 4l \text{ or } ll\nu\bar{\nu}$
	$m_H \approx 1 \text{ TeV}$	$H \rightarrow WW, ZZ \rightarrow l\nu jj, lljj$

1.  $H \rightarrow \gamma\gamma$  :

In this scenario the electromagnetic calorimeter (chapter 3.2.2) clearly plays an essential role, being required to provide a large acceptance, good measurement of the photon direction and excellent energy resolution. Good energy resolution can only be obtained with precise calibration, provided in CMS by tracks measured by the inner tracker. The tracker also serves for performing isolation cuts, i.e. making sure that the photon is not a miss-interpreted product of bremsstrahlung radiated from a charged particle track.

As  $\sigma(Z \rightarrow ee) \approx 25 \cdot 10^3 \sigma(H \rightarrow \gamma\gamma)$ , a rejection of electrons of 500/e is required from the electromagnetic calorimeter in order to reduce the  $Z \rightarrow ee$  background to a level of 10% of the  $H \rightarrow \gamma\gamma$  channel [13].

2.  $H \rightarrow b\bar{b}$  :

For  $m_H < 2m_W < m_t$  the branching ratio for  $H \rightarrow b\bar{b}$  is over 90%, as the Higgs couples preferentially to the heaviest possible quarks, which is characteristic for the symmetry breaking sector. Good  $b$ -tagging is important for the detection of this channel.

3.  $H \rightarrow ZZ^* \rightarrow 4l^\pm$  :

For masses below  $2m_Z$  the width of the Higgs boson is small (Fig. 2.1),  $\Gamma_H < 1 \text{ GeV}$ . Thus, excellent energy and momentum resolution for leptons is needed in order not to wash out the production peak. The main reducible<sup>2</sup> backgrounds,  $t\bar{t}$  and  $Zb\bar{b}$ , can be reduced by lepton isolation cuts, the first also by an  $m_Z$  cut, i.e. requiring one of the  $e^+e^-$  or  $\mu^+\mu^-$  pairs to be close to the  $Z$  mass.

<sup>2</sup>The reducible part of the background is due to the finite resolution and hermeticity of the detector and imperfections in particle identification.

4.  $H \rightarrow WW$  :

Observing the polarisation of the decay leptons in the two-lepton rest frame, the Higgs mass cannot be reconstructed but an excess of such events compared to background processes gives evidence of the existence of the Higgs particle.

5.  $H \rightarrow ZZ \rightarrow 4l^\pm$  :

Being similar to the above process, the criterion for easy observation of this channel is a precise energy determination. The 'enemy' is non-resonant ZZ production, but after a few years of running of LHC, a significance of the signal  $< 10$  can be obtained for masses up to  $m_H \approx 500 \text{ GeV}$ .

6.  $H \rightarrow ll\nu\nu$  :

This channel has a distinct signature: Two high- $p_T$  leptons and high missing transverse energy  $E_T^{miss}$ . The difficult background, either irreducible ( $ZZ$ ,  $ZW$ ) or with a large cross section ( $t\bar{t}$ ,  $Z$ +jets), has to be brought under control with appropriate  $E_T^{miss}$  and  $p_T^{lepton}$  cuts, and requiring  $p_T^{miss}$  to be anti-parallel to the combined lepton momentum.

7.  $H \rightarrow WW, ZZ$  :

At a mass of  $m_H \sim 1 \text{ TeV}$  the Higgs peak is very wide,  $\Gamma_H \approx 0.5 \text{ TeV}$ . Kinematic cuts and double forward jet tagging have to be used as the main tools for detecting the signal against a several order higher background.

### 2.1.3 B physics

The main issue in B-physics is the measurement of CP-violation. With a production cross section of  $\sigma_{b\bar{b}} \approx 500 \text{ mb}$  and a resulting  $10^{12} - 10^{13} \text{ } b\bar{b}$  events produced per year, LHC provides sufficient statistics for high precision measurements. The most interesting case is the decay of  $B^0$  and  $\bar{B}^0$  into a common final state  $F$ . CP violation introduces a multiplicative term in the decay rate which is of opposite sign for  $B^0$  and  $\bar{B}^0$ . Thus, this asymmetry can be expressed as

$$A(\alpha, \beta, \gamma) = \frac{\Gamma(B_f^0 \rightarrow F) - \Gamma(\bar{B}_f^0 \rightarrow \bar{F})}{\Gamma(B_f^0 \rightarrow F) + \Gamma(\bar{B}_f^0 \rightarrow \bar{F})}, \quad f = d, s \quad (2.7)$$

which only depends on the angles of the unitarity triangle and the mixing parameter<sup>3</sup>  $x_f$ . The most promising decay channel is  $B_d^0 \rightarrow J/\psi K_s^0$  with  $J/\psi \rightarrow \mu^+\mu^-$  and

<sup>3</sup>  $\frac{x_s}{x_d} = \frac{V_{ts}}{V_{td}}$  measures one side of the unitarity triangle.

$K_s^0 \rightarrow \pi^+\pi^-$ , for which a  $2\mu$  or  $3\mu$  trigger with mass constraints is appropriate. For this channel the asymmetry is a function of  $\beta$ ,

$$A(\beta) = \sin(2\beta) \cdot \frac{x_d}{1 + x_d^2} \quad (2.8)$$

Studies with different  $p_T$  thresholds show that a  $3\sigma$  measurement of  $\sin(2\beta)$  will require  $4 \cdot 10^4 pb^{-1}$ , which is reached after around four years of operation of the LHC, see [14] and references therein.

## 2.2 Beyond the Standard Model

The Standard Model agrees with all confirmed accelerator data, but is not very satisfactory from a theoretical point of view: It does not explain the particle quantum numbers and contains a large number of arbitrary parameters – 3 gauge couplings  $g_{1,2,3}$ , 6  $m_q$ , 3  $m_l$ , 3  $m_\nu$  (?),  $m_W$ ,  $m_H$ ,  $\delta_{KM}$  and 3 mixing angles  $\alpha, \beta, \gamma$ . Moreover, unification with gravity is not obvious. Thus, it does not seem to be the ultimate theory. The Minimal Supersymmetric Standard Model offers an elegant way to automatically cancel infinities in the Feynman diagrams, by imposing a symmetry between Fermion and Boson states and implements a spin 2 boson, which is a necessary ingredient for the construction of a theory of quantum gravity<sup>4</sup>.

### 2.2.1 The Minimal Supersymmetric Model

The minimal supersymmetric extension of the Standard Model (MSSM) [16] assigns a corresponding supersymmetric partner to each of the known particles. In order to give masses to both  $u$ -type and  $d$ -type quarks and charged leptons, two Higgs doublets are needed. If supersymmetry is realized in nature, there is hope that evidence for it will be found at LHC.

### 2.2.2 The MSSM Higgs Sector

The minimal supersymmetric standard model (e.g. [16]) is the  $N = 1$  supersymmetric extension of the Standard Model [3], featuring two Higgs doublets. The resulting

---

<sup>4</sup>The number of free parameters in the MSSM, namely 124, is somewhat higher than in the Standard Model, but the elegance of the supersymmetric principle has to be appreciated [15].

physical degrees of freedom of the fields with non-vanishing vacuum expectation values manifest themselves as the Higgs bosons  $H^\pm$ ,  $h$ ,  $H$ ,  $A$ , where  $H^\pm$  are the charged scalar bosons, and  $h$ ,  $H$ ,  $A$  are the light and heavy scalar and the pseudo-scalar neutral bosons, respectively. At the tree level, that is, calculating only zeroth-order Feynman diagrams, the masses of the five bosons depend only on two parameters which are usually chosen to be  $m_A$  and  $\tan\beta$ , the ratio between the vacuum expectation values of the two Higgs doublets. Fig. 2.3 shows the searchable area in the  $(m_A, \tan\beta)$  plane that can be covered with CMS.

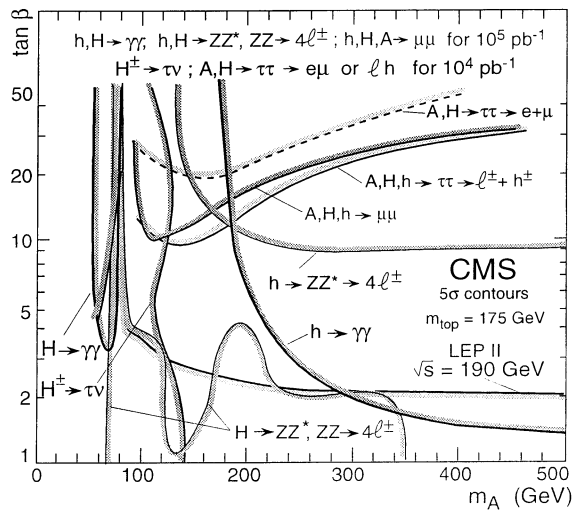


Figure 2.3: Discovery potential for a SUSY Higgs in the CMS detector. The curves indicate up to which combinations of  $m_A$  and  $\tan\beta$  CMS is sensitive to a certain decay channel.  $m_A$  is the mass of the pseudo-scalar boson and  $\tan\beta$  is the ratio between the vacuum expectation values of the two Higgs doublets [17].

## 2.3 Heavy Ion Physics

Matter undergoes phase transitions when subjected to increasing energy densities (temperature, pressure) until at a certain point between a few tens of  $eV$  and several hundred  $keV$  a state can be reached where electrons become fully 'deconfined' from the nuclei. A priori, such an electromagnetic plasma should have an equivalent in QCD. Indeed, finite temperature lattice QCD calculations predict that at  $\rho(E) \approx 1 - 10 \text{ GeV}/fm^3$  a sudden increase in latent heat takes place which might be a sign of a transition of the

hadronic system into a state of deconfinement, dubbed the quark-gluon plasma (QGP) [18]. This density is equivalent to a baryon density 5 to 10 times that of nuclear matter, and is in reach of today's heavy ion accelerators. Nevertheless, up to date no conclusive evidence for the existence of a QGP has been found up to energies of 158  $GeV/nucleon$  at fixed-target Pb-Pb experiments with  $208Pb^{82+}$  at the SPS/CERN.

The LHC will dramatically expand the searchable range for a phase transition point by colliding lead ions with a centre-of-mass energy  $\sqrt{s} > 1000 TeV/nucleon$  (chapter 3.1.2). Experiments will look for various signatures that can reveal the presence of a QGP. The clearest signal will be that of the suppression of heavy quark bound states [19]. As a consequence of the large mass of the c and b quark,  $c\bar{c}$  and  $b\bar{b}$  can only be created at the highest possible collision energies, i.e. during primary nucleon-nucleon collisions and therefore only before a thermal equilibrium is created. Whereas the  $\Upsilon$  state production rate will be less affected by a QGP phase, the production rate for the higher bound states  $\Upsilon'$  and  $\Upsilon''$  should be decreased [20]. If a plasma phase would precede this equilibrium, these vector mesons would be dissolved resulting in a suppression of the  $c\bar{c}$  and  $b\bar{b}$  bound states,  $J/\psi$  and  $\Upsilon$ . The experimental detection of these states is done via the  $\mu\mu$  decay channel, but detector acceptance for  $J/\psi$  decays is negligible. and  $\Upsilon$  production rates will be used for QGP detection. Simulations on the CMS tracker show that the mass resolution for the  $\Upsilon$  can be expected to be  $\sigma \approx 37 MeV$ . The extrapolated cross sections for  $\Upsilon$  production at LHC energies suggest a production of some 1000  $\Upsilon/day$  in pp-collisions. This gives a signal-to-background ratio for  $\Upsilon$  production of 0.1 – 1 in 15 days of data taking with the CMS detector, which is sufficient for detecting a change of production rates when going to the Pb-Pb system.

# Chapter 3

## LHC and CMS

In the previous chapter an overview of the various open questions in physics that will be addressed with the upcoming new accelerator and its associated detectors was given. Now a closer look shall be taken at this machine and the detector in whose development I had the opportunity to take an active part.

### 3.1 LHC

High-energy physics has always been the driving force behind the development of particle accelerators. In the beginning were the electrostatic machines. Inspired by Rutherford, Cockroft and Walton built the Cockroft-Walton generator [21], which, in 1932, could accelerate electrons to  $700\text{ keV}$  and allowed to perform the Nobel-prize winning atom-splitting experiment. At the same time the Van de Graff generator used a mechanical belt to charge the two ends of an accelerating tube. Working with the same principle, still today a Tandem accelerator ('Vivitron') with  $\sim 18\text{ MeV}$  is in operation <sup>1</sup>. A breakthrough was the invention of resonant acceleration, which allowed to repeatedly apply an accelerating field to the particles. This is the operating principle of the linac. Easier to build, the cyclotron was the first instrument using this idea (Ising, Lawrence, 1929) [22]. It was, however, limited by relativistic effects and so the synchrotron was invented, using the principle of betatron acceleration: By tuning the magnetic field it became possible to keep the accelerated particles on a closed orbit, despite their increase in energy [23].

---

<sup>1</sup><http://ireswww.in2p3.fr/ires/recherche/vivitron/vivitron.html>



In 1952 the principle of strong (alternate gradient) focusing was developed, allowing to overcome the stringent precision limitations on the magnetic field gradient for constant-gradient focusing. This paved the way for storage ring colliders, of which the first one was the CERN ISR (Intersecting Storage Rings) in 1972. To date, CERNs Large Electron Positron collider (LEP) is the worlds largest accelerator and will be operating until the year 2000.

The Large Hadron Collider, LHC, is the next step in exploring the domain of particle physics and gaining a deeper understanding in "what it is that keeps the world together" [24].

### 3.1.1 The Accelerator Chain

One of the LHCs big assets is the possibility to use, after several modifications and additions, all of CERNs existing proton accelerators to obtain its supply of pre-accelerated protons [25]. In the beginning of the accelerating chain stands the 50 *MeV* proton linear accelerator (Linac 2), followed by the 1 *GeV* proton synchrotron booster (PSB). The bunches are formed in the 26 *GeV* proton synchrotron (PS) with the correct 25 *ns* bunch spacing by adiabatic capture of a previously debunched beam with a 40 *MHz* RF system. During several cycles the bunches are then transferred to the super proton synchrotron (SPS), filling approximately 1/3 of its circumference, which is the maximum the SPS can handle. After its acceleration to 450 *GeV* with a new superconducting RF system (6 *MV* at 400.8 *MHz*) the beam is then fed into the LHC. This operation is performed 12 times for each of the two beams of the LHC and takes about seven minutes. During the following 20 minutes the protons gain  $\sim 0.5 \text{MeV}/\text{turn}$  and reach the nominal LHC energy of 7 *TeV*.

### 3.1.2 7+7 TeV

The Large Hadron Collider project [26] was approved in 1994. With its 1232 14.2 *m* long 8.4 *T* superconducting dipole magnets the machine will provide proton-proton collisions with a centre-of-mass energy of  $\sqrt{s} = 14 \text{TeV}$  in 25 *ns* intervals. In order to fit into the existing LEP tunnel, the LHC will have the same circumference of 26.6 *km*. The temperature of operation will be below 2°*K*. This is needed in order to have an appreciable safety margin against quenching of the superconducting magnets but also has the positive side effect that the Helium (<sup>4</sup>He) used for the cooling is present in its superfluid phase, which greatly simplifies the mechanical cooling layout and at the same

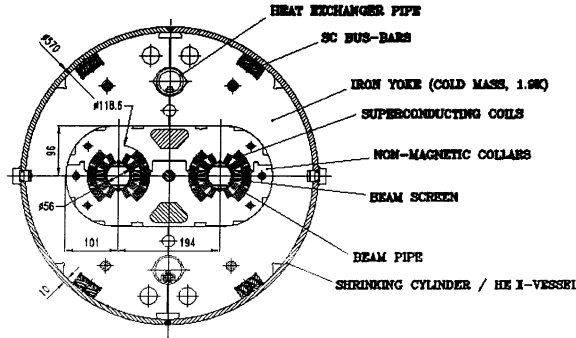


Figure 3.1: Cross section of an LHC dipole superconducting magnet bending the two anti-parallel proton beams in a  $8.4\text{ T}$  magnetic field.

time makes the heat transfer very efficient due to the high heat capacity of superfluid  $^4\text{He}$ . During the first years of running the LHC beams will feature a 'low' luminosity of  $L \sim 10^{33}\text{ cm}^{-2}\text{s}^{-1}$ , after which the nominal ('high') luminosity of  $L \sim 10^{34}\text{ cm}^{-2}\text{s}^{-1}$  will be reached. The luminosity can be calculated from

$$L = \frac{N^2 k_b f \gamma}{4\pi \epsilon_n \beta^*} F \quad (3.1)$$

where  $N = 1.05 \cdot 10^{11}$  is the number of protons per bunch,  $k_b = 2835$  the number of bunches,  $f$  the revolution frequency,  $\gamma$  the relativistic factor,  $\epsilon_n = 3.75\text{ }\mu\text{m} \cdot \text{rad}$  the normalised transverse emittance,  $\beta^* = 0.5\text{ m}$  the value of the betatron function at the interaction point and  $F = 0.9$  the reduction factor at the interaction point (see chapter A.1). At LHC, the maximum attainable luminosity is limited by the beam-beam interaction, which is the unavoidable head-on interaction during collisions and the long-range interaction close to the interaction points when both beams run side by side in a common beam pipe.

During the low luminosity phase the beam current will be limited to  $87\text{ mA}$ , as opposed to  $530\text{ mA}$  nominal value. This phase is necessary as LHC is the first superconducting collider foreseen to operate with large beam currents, and superconducting magnets only tolerate very small beam losses without quenching. Thus the beam halo has to be intercepted in non-superconducting sections of the machine. These collimators will be tested and tuned during the first year of operation.

At  $L = 10^{34}\text{ cm}^{-2}\text{s}^{-1}$  the half-life of the luminosity should be about  $10\text{ h}$ , determined by the collisions of the beams with each other, collisions with residual gas in the beam pipe, imperfections of the machine, and the resulting necessary 'cleaning' of the beam from protons that escape the phase-space window allowed for the bunches.

The optimum duration of data taking depends on this half-life and on the time it takes to refill the accelerator ( $\sim 2 h$ ), and will be around  $7 h$ .

Protons were chosen due to their mass being  $\sim 1800$  times higher than electrons, which are currently being accelerated in the LEP (Large Electron Positron collider). At LEP, the barrier limiting an ever higher acceleration of the electrons is mainly Bremsstrahlung (synchrotron radiation), which increases like  $\Delta E_{brems} \propto E^4/(m^4 r)$  with the particle energy  $E$  [27].  $r$  denotes the bending radius of the particle beam. With the need to put LHC into the same tunnel as LEP, i.e. having  $r$  fixed, the only way to decrease the amount of radiated energy was to increase  $m$ , which is the reason why protons are used.  $\Delta E_{brems}$  will be several  $keV/turn$  at LHC, as compared to  $\sim 3 GeV/turn$  at LEP. Unlike SPS, LHC will not provide  $p\bar{p}$  collisions. Making one beam out of anti-protons would be favourable in terms of beam-beam interactions, but anti-protons are not available in big enough quantities to allow the high luminosities dictated by the smallness of the interaction cross-sections of interest.

LHC will also provide heavy ion (Pb) collisions with a centre-of-mass energy of  $\sqrt{s} = 1148 TeV$  and a luminosity  $L > 10^{27} cm^{-2}s^{-1}$  at  $125 ns$  bunch crossing intervals. The value for  $\sqrt{s}$  corresponds to  $E = 7 TeV/charge$  for  $208Pb^{82+}$  ions, i.e. fully stripped ions. The Pb supply can be provided by a modified version of the already existing Lead-Ion Acceleration Facility (LIAF) [28].

The high luminosity and energy of the proton beams will create a very hostile radiation environment. About 20 proton collisions are expected per bunch crossing (every  $25 ns$ ), creating several thousand particles each. Fig. 3.2 shows the expected neutron and charged hadron dose at different radii from the interaction points that the inner tracker will receive within the foreseen 10 years of LHC operation. In the central region the flux of charged particles is constant per unit of pseudorapidity  $\eta$ ,

$$\eta = \frac{1}{2} \log \frac{E + p_z}{E - p_z} \quad (3.2)$$

but decreases radially in the presence of a magnetic field differently from  $1/r^2$ ,  $r$  denoting the transverse distance from the interaction point. Whereas at  $20 cm$  from the beam spot the occupancy is two times higher than in the absence of a magnetic field, the numbers are equal at  $65 cm$ , and particle density drops faster than  $1/r^2$  for larger radii. Neutron fluxes, on the other hand, are almost constant over the central part of the tracker volume due to their production in the calorimeters (chapter 3.2). This particular flux distribution has a decisive influence on the design of the CMS tracker, which is described in chapter 4.

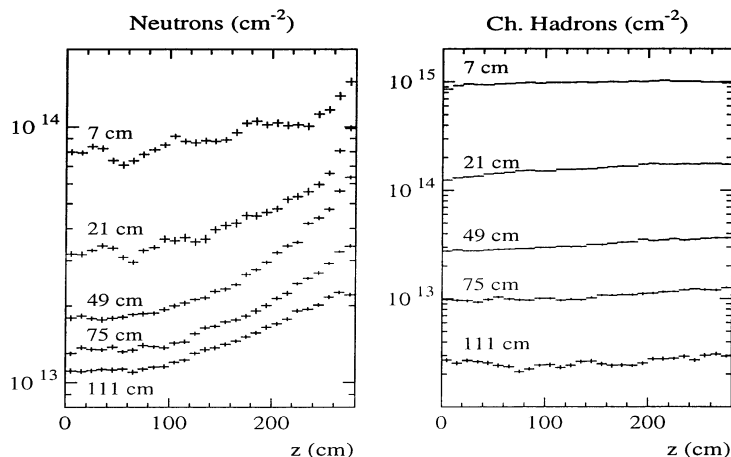


Figure 3.2: Integrated particle fluxes over 10 years of LHC operation at different transverse distances from the interaction point relevant to the tracker.

### 3.1.3 Experiments at LHC

At the four beam intersections foreseen at LHC (Fig. 3.3), four experiments will operate. Two of them, ATLAS [29] and CMS [13] – the latter is described in the following section – are ‘all purpose’ detectors and have as a main task the detection of the Higgs and supersymmetric particles. They are located at the high luminosity low  $\beta$  (explained in chapter A.1) intersection points diametrically opposite each other (Fig. 3.3).

**ATLAS** – A Toroidal Lhc ApparatuS [29] – is the biggest detector system ever conceived for a collider experiment. The inner tracker is housed within a 2 T solenoid, consisting of pixel- and microstrip silicon detectors and straw drift tubes interleaved with transition radiation detectors. The electromagnetic sampling calorimeter uses layers of lead and liquid Argon. The latter, together with copper absorber plates is also used for the endcap hadronic calorimeter, whereas its barrel equivalent is an iron-scintillating tile sampling calorimeter. Superconducting air-core toroids in the outer barrel and the end-caps generate the magnetic field for the muon spectrometer consisting of drift tubes and cathode strip chambers and resistive plate chambers for triggering.

**LHC-B** [30] is a single arm spectrometer and designed to study CP violation and other rare phenomena involving heavy flavours, in particular B-meson decays. A 19 layer silicon strip system performs vertex detection, followed by Micro Cathode Strip Chambers and honeycomb drift chambers improving the tracking performance. An ex-

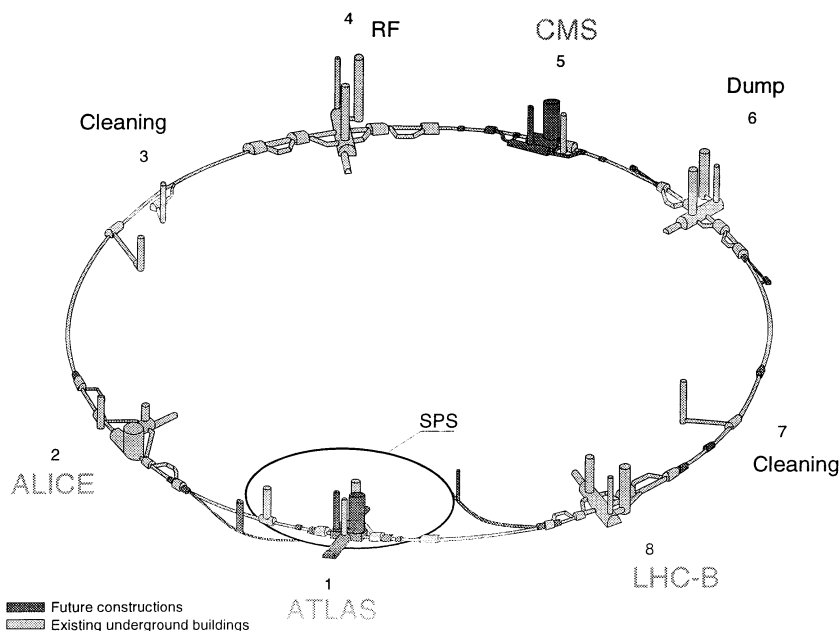


Figure 3.3: Schematic layout of the LHC accelerator complex (26.6 km circumference). Four intersection points host the four experiments that are approved to date.

tensive RICH system made of aerogel,  $C_4F_{10}$  and  $CF_4$  and read out by Hybrid Photon Detectors provides particle identification. The electromagnetic and hadronic calorimeters are in a Shashlik and scintillating tile design, respectively. Multigap resistive plate chambers and cathode pad chambers performs the muon identification and -trigger.

**ALICE** – A Large Ion Collider Experiment [31] – is optimised for analysing the heavy ion collisions that LHC will provide (Pb-Pb at  $\sqrt{s} \sim 2.8 \text{ TeV/nucleon}$ ). The physics of interest is that of the quark-gluon plasma, as described in chapter 2.3. The  $5 \cdot 10^4$  particles created in each Pb-Pb collision ( $dN/d\eta \approx 8000$ ) are detected and identified in an asymmetric detector, comprising a central and a forward part. The first, reusing the L3 magnet, contains a six layer silicon tracker for identifying  $s$ - and  $c$ -quarks by reconstructing their decay vertices, a time projection chamber for track reconstruction, a  $\gamma$  spectrometer similar to the CMS ECAL (see below), Parallel Plate chambers doing time-of-flight measurements and Cherenkov counters, both capable of reconstructing the particle masses. The forward region is made up of a muon detector, 14 planes of

tracking and triggering chambers and a large dipole magnet.

## 3.2 CMS

CMS is one of the two experiments that will search for the Higgs particle in the year 2005. A sketch of this 21.6 *m* long and 14 *m* high cylindrically shaped detector is displayed in Fig. 3.4. Having in mind the broad physics program described in chapter 2, a few considerations specify the baseline requirements of the experiment. A powerful muon system for detecting a possible  $4\mu$  decay channel of the Higgs particle, the best possible electromagnetic calorimeter compatible with the muon system in order to resolve the two photon decay of the Higgs boson and excellent central tracking with high efficiency to provide the necessary momentum resolution and good vertex reconstruction (b-tagging).

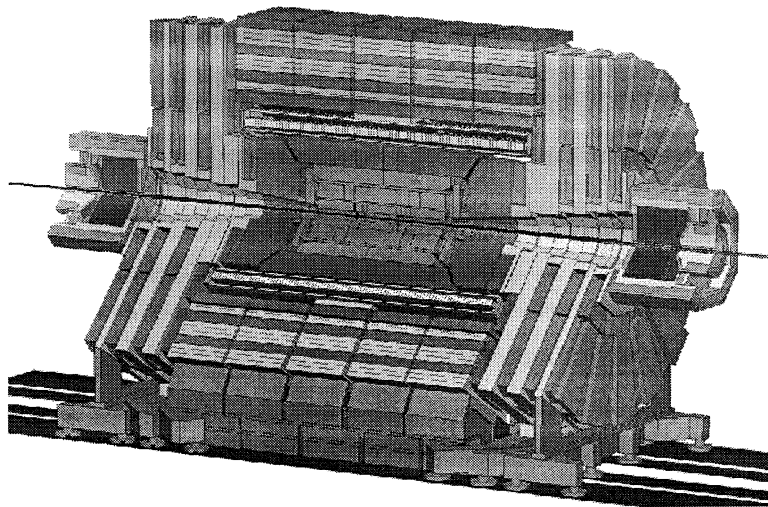


Figure 3.4: The CMS detector. From the inside to the outside: Tracker, ECAL, HCAL, magnet, muon system.

The several sub-detectors that CMS contains are shortly described in the following. A separate chapter is devoted to the inner tracker, which houses the MSGCs that I have been working on for this thesis. More information on many aspects of the different sub-detectors can be found in the Technical Design Reports [32, 33, 34, 35, 36].

### 3.2.1 Inner Tracker

The role of the inner tracker is to measure the curvature of the tracks of the particles produced in the collisions which, combined with an energy measurement or particle identification allows to calculate the momentum of the particles, and to determine which interaction vertex the particles originated in. The tracker is described in detail in chapter 4.

### 3.2.2 Electromagnetic Calorimeter

A calorimeter measures the amount of energy a particle loses when traversing it. Inferring their momentum from measurements in the inner tracker, the mass and thus the type of the particle can be determined. As interaction processes of leptons and hadrons are very different, two different calorimeters – electromagnetic and hadronic – are used for the two types of particle families. There are two principal approaches for building a calorimeter: Either the material in which the particles lose the energy that is being measured and the elements used for measuring the amount of this energy are the same, or the two are different and interleave each other. These two configurations are called 'fully active' and 'sampling' calorimeters, respectively.

The electromagnetic calorimeter (ECAL) at CMS has opted for the fully active configuration, employing  $\text{PbWO}_4$  crystals. This material has several advantages:

- ) It has a short radiation length  $X_0 = 9 \text{ mm}$  and small Moliere radius,
- ) scintillation decay time is short,  
85% of all photons are produced within  $25 \text{ ns}$ .
- ) Also, the crystals are relatively easy to grow ( $140 \text{ h}$  / crystal).

Their disadvantage – a low light yield ( $50 - 80 \gamma/\text{MeV}$ ) has to be compensated by using a sensitive read-out technology. The high magnetic field and the – especially in the forward region – high radiation environment restrict the number of options. In the barrel region silicon avalanche photodiodes (APDs) will be used and vacuum phototriodes in the endcaps. Another critical issue is the temperature sensitivity of the crystals. An increase in temperature of  $1^\circ\text{C}$  leads to a decrease of light emission of  $-2\%$  at room temperature, due to thermal quenching of the scintillation mechanism. Thus the operating temperature has to be kept constant to a tenth of a degree.

The size of the crystals is determined by the Moliere radius. A small radius and a crystal square cross section of  $\sim 22 \times 22 \text{ mm}^2$  allows to resolve the decay process  $\pi^0 \rightarrow 2\gamma$ , where the two photons must not be mistaken as a single one. In order have

a high hermeticity, the length of the crystals was chosen to be  $23\text{ cm}$  ( $25.8 X_0$ ,  $1.1 \lambda$ ). In the forward region the dimensions read  $\sim 25 \times 25 \times 220\text{ mm}^3$ .

A pre-shower detector in the endcap region and optionally also in the barrel completes the ECAL. Placed in front of the crystals its main function is to provide  $\pi^0/\gamma$  separation. It consists of lead converters, in total around  $3 X_0$  thick, followed by silicon strip detectors (pitch  $\sim 2\text{ mm}$ ), which determine the position of the beginning of the electromagnetic shower with a precision of  $\sim 300\ \mu\text{m}$ .

Calibration, essential for obtaining the desired performance of the ECAL, is done with isolated electrons from  $W^\pm$  and  $Z^0$  decays, as the mass of the vector bosons is known to a high precision. In parallel, high- $p_T$  electrons whose momentum was determined by the tracker are used for energy calibration on a crystal-by-crystal basis. A glass fibre system distributing laser pulses will permit monitoring of the lead-tungsten crystals by measuring the radiation induced variations of the transparency of the crystals and possible changes of the quantum efficiency of the APDs.

The energy resolution obtained with this calorimeter is  $\sigma/E = 2.7\%/\sqrt{E} \oplus 0.55\%$  for the barrel region and  $\sigma/E = 5.7\%/\sqrt{E} \oplus 0.55\%$  for  $\eta = 2$  ( $E$  in  $GeV$ ). The possibility of miss-identification of jets and  $\pi^0$ s faking photons is about 15%. These numbers, translated to the most difficult physics for the ECAL, the  $H \rightarrow \gamma\gamma$  decay, yields a mass resolution of  $\Delta m_H < 0.7\text{ GeV}$  for a simulated  $m_H = 100\text{ GeV}$ .

### 3.2.3 Hadronic Calorimeter

The hadronic calorimeter (HCAL) is built with the sampling technology and is, like the ECAL, contained within the magnet. Copper absorbers are interleaved with plastic scintillators with wavelength shifting glass fibre read-out. The barrel region is covered by 10 copper layers with a depth of  $30\text{ mm}$  each, and 10 layers which are  $60\text{ mm}$  deep, forcing each particle to traverse through  $1\text{ m}$  of material, equivalent to 11 interaction lengths. The total depth being determined by the maximum size of the magnet which can, due to logistic limitations, not exceed a diameter  $d > 6.8\text{ m}$ , copper was chosen due to its short interaction length,  $\lambda_I = 15\text{ cm}$ . The low  $Z$  of copper also keeps the multiple scattering, which affects momentum resolution, to a minimum.

The same technology of alternating copper and scintillator layers is employed by the forward region, featuring 19 absorber plates with scintillator layers in between and covering the region  $1.3 < \pm\eta < 3.0$ .



Calorimetry also aims at covering the very forward region,  $3.0 < \pm\eta < 5.0$  in order to improve the measurement of the missing transverse energy and to identify and reconstruct very forward jets. Due to an average particle multiplicity of  $\sim 5700$  per bunch crossing the region  $4.5 < \pm\eta < 5.0$  will experience a particle density of  $\rho \approx 6.0 \text{ MHz/cm}^2$ . The forward calorimeter and its read-out must be able to withstand the resulting neutron fluxes. The technique chosen consists of a copper block with embedded quartz fibres reading out the produced Cherenkov radiation. Using this calorimeter to achieve a hermeticity down to  $|\eta| \approx 5.0$ ,  $E_T^{miss}$  can be reduced by an order of magnitude in the  $20 - 120 \text{ GeV}$  energy range.

The importance of the HCAL is twofold. It has to measure hadronic jets and missing transverse energy. Both are essential to detect a high mass standard model Higgs particle through its  $ll\nu\nu$ ,  $lljj$  and  $l\nu jj$  decay channels. Significant  $E_T^{miss}$  is also part of the signatures of supersymmetric particle production. With the design described above a single particle energy resolution of  $\sigma/E = k/\sqrt{E} + 0.05$ ,  $E$  in  $\text{GeV}$ , can be obtained, with  $k$  ranging from 0.65 to 1.0 for rapidities  $\eta$  ranging from 0.0 to 4.0.

### 3.2.4 Muon System

Particles that reach the muon detectors have traversed 16 interaction lengths on their way. Thus their probability of being muons is very high. As one of the key signatures for the existence of the Higgs particle is its decay  $H \rightarrow 4\mu$ , the hermeticity of the muon detector has to be as large as possible, resulting in a longitudinal coverage up to  $|\eta| < 2.4$ .

The barrel region contains four interleaving layers of muon stations and iron layers, which form the return yoke of the magnet (see below). Each muon station itself consists of 60-70 drift chambers with a wire length of  $2.5 \text{ m}$  and a diameter of the drift volume of  $2 \text{ cm}$ , keeping the time of drift below  $400 \text{ ns}$ .

The two endcap regions are covered by four layers of disks, where the first layer is segmented into three concentric rings of which the innermost is offset by  $\sim 1 \text{ m}$  towards the interaction point. Cathode Strip Chambers (CSCs) are the detecting elements chosen for the endcap regions. Six layers of CSCs are stacked in each disk. They are multiwire proportional chambers, in which one cathode plane consists of strips orthogonal to the anode wires, providing full three-dimensional space points with accuracies around  $\sim 100 \mu\text{m}$ .

When looking for the  $H \rightarrow 4\mu$ , it will be the muon chambers that generate the trigger. While one CSC has an uncertainty in its time measurement that exceeds the 25 ns window of one bunch crossing, it is possible to achieve a very high efficiency in tagging the relevant bunch crossing by combining the time measurements from several muon stations. Indeed, combining all four endcap disks, the correct bunch crossing assignment is obtained with a probability higher than 99%.

The main role in triggering, though, is played by resistive plate chambers (RPCs) which are found in each layer in the barrel and the endcaps. These are gaseous parallel-plate detectors with time resolution comparable to scintillators. The drift of the electrons of the  $e^-$ /ion-pairs created in the 2 mm gas gap by traversing particles induces a signal on the pick-up anodes outside the gas volume within below 15 ns. Due to the high rates in LHC they cannot be operated in the commonly used streamer mode, but will stay in the avalanche regime. Space information is obtained by segmenting the anodes.

### 3.2.5 Magnet

In order to interfere the least possible with the operation of the ECAL and HCAL and allow the best possible performance, the magnet forms a layer outside the calorimeters, instead of only surrounding the tracker. Not only does the magnet generate a high magnetic field of 4 T, but it also does this with very high uniformity over all the enclosed volume. This allows very good transverse momentum measurements (chapter 4.4).

The magnet coil is 13 m long and has an inner diameter of 5.9 m. It produces a solenoidal field. The superconducting cable is made of three different layers, optimising electrical and mechanical characteristics. 36 strands of NbTi filaments make a Rutherford type cable which is embedded in aluminium, for stabilisation and heat transfer in the event of a quench, i.e. a transition from the superconducting to the normal state in a localised region of the coil. A further layer of aluminium alloy reinforces the structure and carries the axial force generated by the magnetic field. This allows a critical current  $I_c = 62.5 \text{ kA}$  at  $T = 4.2 \text{ K}$ ,  $B = 5 \text{ T}$ . Ramp-up time will be around 4 hours, whereas in case of a quench the total stored energy in the cold mass of 2.7 GJ can be dumped in less than 5 minutes.

The magnetic flux is returned via a 1.5 m thick saturated iron yoke (1.8 T) embedding the muon stations. The high homogeneous magnetic field over a diameter of 5.9 m

allows an excellent momentum resolution for charged leptons and hadrons of about 1% at 100  $GeV$ , while at the same time keeping the first level trigger rate for  $p_T > 20 GeV$  muons at a digestible level by bending lower momentum muons into a circle inside the volume of the magnet.

### 3.2.6 Trigger

Reading out all the data generated in  $\sim 10^9$  collisions each second, each one filling  $9.8 \cdot 10^7$  read-out channels of the detector would produce a data flow too high to cope with. Using a sophisticated trigger and read-out system the data rate can be reduced substantially. The data acquisition process can be broken down into four main elements: The first two, the front-end detector electronics and the calorimeter and muon first level triggers are read out for each bunch crossing and stored in a  $\sim 3 \mu s$  pipeline. They already provide rough information on what types of events have happened during the bunch crossing. The other two, a high bandwidth read-out network ( $\sim 500 Gbit/s$ ) and powerful on-line event filter system ( $\sim 10^7$  MIPS), replace the second and third level trigger. With this configuration, the first level trigger achieves a reduction from 40  $MHz$  to 100  $kHz$ , and the on-line filter farm further reduces the actual number of events that are fully reconstructed to around 100  $Hz$ .

# Chapter 4

## The CMS Inner Tracker

New physics is expected to be encountered at LHC. In order to be prepared for the detection of unknown particles, CMS has to be able to identify and measure particles over a broad range of energies. For measuring their momentum and determining their point of origin, CMS will be equipped with an extensive tracking system contained in a 4  $T$  magnetic field.

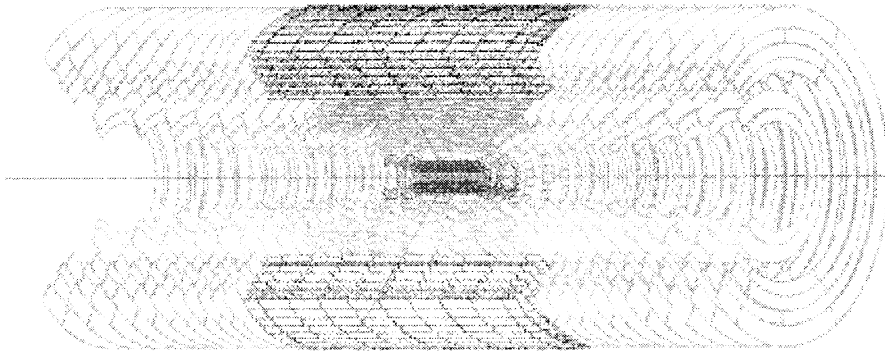


Figure 4.1: The CMS Inner Tracker, with a length of 6  $m$  and a diameter of 2.6  $m$  [32].

The physics objectives have already been presented in chapter 2. They put stringent performance requirements on the inner tracker. One of the possible decay channels for the Higgs particle is its decay into vector bosons, which themselves can decay into leptons. Thus, for a precise determination of the Higgs mass, excellent momentum resolution for leptons above a few  $GeV$  is needed. The tracks of electrons,

Table 4.1: Three different detector technologies will be used for the CMS tracker, each one providing the radiation hardness and fine granularity required by the intense particle flux (Fig. 3.2) and at the same time keeping the necessary number of read-out channels as low as possible while offering a good track resolution.

	radius	area	# channels	resolution	$\int$ flux (10 yr LHC)
Silicon Pixel	4 – 11.5 cm	$< 1 m^2$	$4 \cdot 10^7$	15 $\mu m$	$\sim 10^{15} cm^{-2}$
Silicon Strip	21 – 63 cm	$\sim 75 m^2$	$5.4 \cdot 10^6$	25 $\mu m$	$\sim 10^{14} cm^{-2}$
MSGCs	68 – 123 cm	$\sim 225 m^2$	$6.6 \cdot 10^6$	35 $\mu m$	$\sim 10^{13} cm^{-2}$

though, might be highly affected by the material of the tracker due to the emission of Bremsstrahlung and multiple scattering. Hence, the tracker has to be made out of as little material as possible. But recognising this Higgs decay in a background that is larger by several orders of magnitude is not an easy task. All four leptons have to be detected with high efficiency and have to be identified as being indeed isolated leptons. This requirement and the necessity of a low cell occupancy despite the expected high particle flux ask for a high granularity of the detecting elements. Also, radiation hardness for up to ten years of operation is of high importance.

The solution adopted for CMS comprises three different detector technologies, see Fig. 4.1. Closest to the beam pipe are Silicon Pixel detectors, followed by Silicon Strip detectors. The outermost region is made up of Microstrip Gas Chambers. Table 4.1 gives the details of the three types of detectors in the CMS tracker.

## 4.1 Silicon Pixel

Silicon pixel detectors will be mounted very close to the beam pipe. During the first years when LHC will not run at full luminosity, two layers will be placed at radii of 4 and 7 cm. In a second phase, the innermost layer will be replaced by layer at a radius of 11.5 cm. Two disks in each of the forward direction increase the rapidity coverage up to  $\eta = 2.4$ . The whole pixel subsystem forms a 100 cm long cylinder, with – depending on the above configuration – roughly 20 to 30 million read-out channels, and covers an area of 0.4 – 0.6  $m^2$ .

The material chosen is an n-type Silicon substrate with n<sup>+</sup> implants for electron collection. Due to the high radiation dose the detector is exposed to, type inversion

will take place. n-pixel readout has the advantage that the depleted region will then be on the pixel side. The presence of a non-zero drift angle (Lorentz angle, see chapter 5.1.2) is used to increase the detector resolution, as follows.

The pixel size is  $150 \mu\text{m} \times 150 \mu\text{m}$ . This would yield an intrinsic resolution of  $150 \mu\text{m}/\sqrt{12} \sim 45 \mu\text{m}$ . The drift angle for electrons in Silicon in a magnetic field of

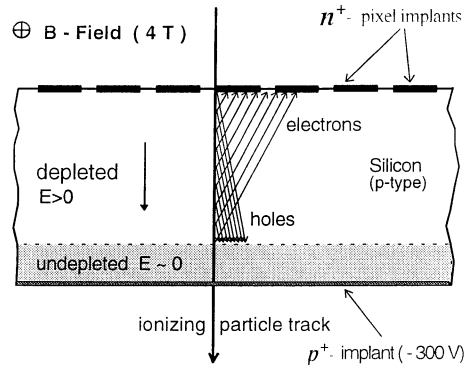


Figure 4.2: Charge sharing due to a non-zero Lorentz angle appreciably increases the spatial resolution of the Si-pixel detectors.

$4 T$  is  $32^\circ$ , spreading the electrons that are produced in a depleted depth of  $250 \mu\text{m}$  of Silicon over  $250 \times \tan(32^\circ) \sim 150 \mu\text{m}$ , causing charge sharing between pads (Fig. 4.2). The result is a hit resolution of  $10 - 15 \mu\text{m}$  in the  $(r\phi)$ -direction, and between  $50$  and  $100 \mu\text{m}$  in the  $z$ -direction measured by the barrel modules. Tilting the detectors in the end-cap regions by  $20^\circ$  will permit to reach a similar resolution of  $15 - 20 \mu\text{m}$  [32].

Keeping the silicon cold is important to limit the noise induced by leakage currents, but mainly to reduce the effect of reverse-annealing after the onset of irradiation, where formerly inactive defects in the material become active and trap the electrons or holes. Thus, once the detector is in operation, it will be maintained at a temperature of  $-10^\circ\text{C}$ .

## 4.2 Silicon Strip

The intermediate region of the tracker, ranging from  $r = 21 \text{ cm}$  to  $r = 63 \text{ cm}$ , is equipped with Silicon Microstrip detectors. The barrel segment consists of five cylindrical layers and six 'mini-disks' at higher rapidities, the two end-cap regions are made of 10 disks each. The former employs rectangularly shaped modules, whereas wedge

shaped modules are used in the latter. Two layers in each of the barrel and the two forward regions are equipped with small-angle stereo modules allowing to obtain true space-points of the tracks.

The substrate is  $300\ \mu\text{m}$  thick n-type silicon. The pitch of the micro pattern varies from  $60$  to  $270\ \mu\text{m}$ , for the different layers, strip lengths range between  $7$  and  $12\ \text{cm}$ . The dimensions were chosen such that the average cell occupancy is on the order of one per cent. The stereo modules consist of two single modules, one rotated by an angle of  $100\ \text{mrad}$  with respect to the other. All modules are tilted by  $19^\circ$  in order to compensate for the Lorentz angle (see also chapter 5.1.2).

A module with  $50\ \mu\text{m}$  pitch reaches a spatial resolution of  $11\ \mu\text{m}$  in the  $(r\phi)$ -direction, with stereo modules having  $100\ \mu\text{m}$  pitch a resolution of  $34\ \mu\text{m}$  can be obtained. Additionally, the stereo modules measure the  $z$ -coordinate of the tracks with a precision of  $\sim 320\ \mu\text{m}$ .

Signal-to-noise ratios of  $\leq 25$  can be reached for non-irradiated detectors<sup>1</sup>. Irradiation, however, increases the inter-strip capacitance and reduces the charge collection efficiency such that the signal-to noise ratio would be reduced by a factor 2-3 after 10 years operation at LHC. Over-depletion, that is an increase of the bias voltage to values higher than the full depletion point, can partly counterbalance the effect and keep the reduction of the signal-to-noise ratio within 20%. Full efficiency is already obtained for signal-to-noise values of 10.

Together with the pixel detectors, the silicon strip detectors will operate at a temperature of  $-10^\circ\text{C}$ . A thin heat shield will isolate them from the surrounding microstrip gas chambers, which will operate at ambient temperature ( $18^\circ\text{C}$ ).

### 4.3 Microstrip Gas Chambers

The CMS tracker is completed by MicroStrip Gas Chambers. They have the difficult task of covering an area of  $\sim 240\ \text{m}^2$  while at the same time providing a spatial resolution better than  $50\ \mu\text{m}$ . Robust track identification with several thousand tracks per event requires a low cell occupancy and thus small cell sizes. This is also imperative for a good momentum resolution, which in addition asks for many measured points per track. Financial constraints limit the number of readout channels available to fulfil this task.

MSGCs were found to be a good solution. The use of gas as ionising and

---

<sup>1</sup>when operated at a bias voltage of  $\sim 200\ \text{V}$ .

drifting medium (see chapter 5) introduces diffusion of the electrons, spreading the charge liberated by traversing particles over several strips and allows to interpolate the position between strips to a precision much better than  $pitch/\sqrt{12}$ . The MSGC technology also features a sufficiently fast charge collection time of  $\sim 50$  ns, which limits the signal pile-up to two bunch crossings (chapter 3.1.2).

The barrel region with an extension along the beam axis of 240 cm consists of 6 cylindrical layers, at equally spaced radial distances from the interaction point ranging from 68 cm to 123 cm. Layers 1, 4 and 6 will be equipped with stereo modules. Similarly to the above mentioned Silicon Strip stereo modules, these are two independent modules assembled one on top of the other and slightly rotated with respect to the other which allow a two-dimensional determination of the track position.

Along each cylindrical layer, every five modules are grouped longitudinally on superstructures called rods (Fig. 4.3). These are light-weight carbon fibre frames on which the modules are aligned before being inserted into the over-all supporting structure. They carry cooling pipes and distribute the high and low voltages as well as the

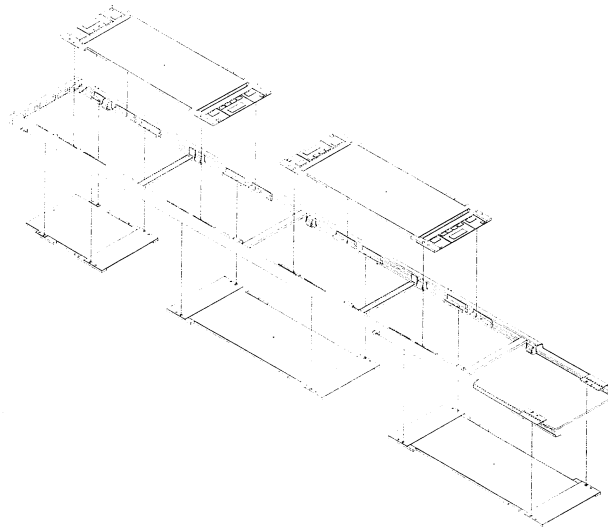


Figure 4.3: The rod concept: Several barrel MSGC modules are mounted on a rigid yet light-weight carbon fibre structure that integrates cabling and cooling. These so-called 'rod's are then inserted into the barrel structure.

control and signal cables to the single modules. The barrel region will house 736 such rods, holding a total of 5540 MSGC modules.

The two forward regions will be covered with 11 disks of MSGCs. A disk consists of



4 concentric rings, each holding around 100 modules. These are wedge shaped with smaller widths closer to the beam pipe.

Table 4.2 gives an overview of the different types of MSGCs that will be used in the barrel region of the CMS tracker. Strip lengths of 12.5 and 25 *cm* are used in order to keep the cell occupancy below a few percent. The work in this thesis only deals with prototypes of modules designed for the *barrel* region of the CMS tracker, and thus, whenever 'MSGC' or 'module' or 'chamber' is written, 'barrel MSGC', 'barrel module' and 'barrel chamber', respectively, should be understood. A picture of a  $10 \times 25 \text{ cm}^2$  MSGC module is shown in Fig. 4.4.

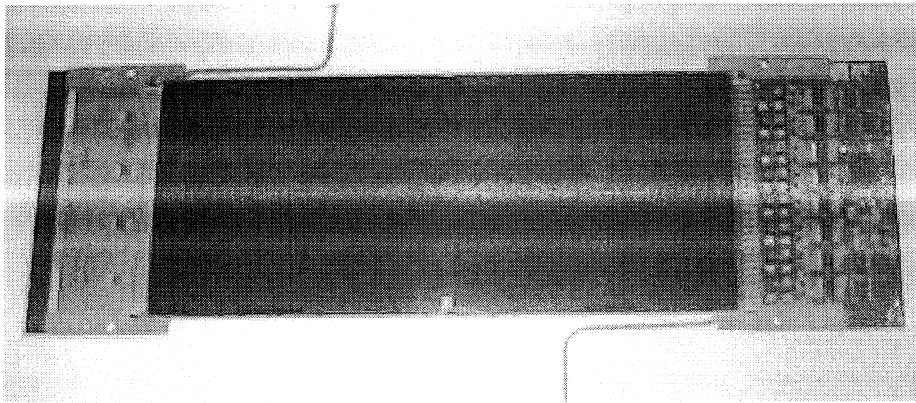


Figure 4.4: A  $10 \times 25 \text{ cm}^2$  MSGC module. In the right side the high voltage hybrid can be seen, the left side shows the low voltage hybrid with the four PreMux chips, each reading out 128 strips.

## 4.4 Performance of the tracker

At the time of the assembly of the detector, each of the three subsystems is aligned mechanically, for the MSGCs also a system as described in chapter 6.3 is used. The precise position of the modules within the tracker is recorded with laser beams. The final alignment, however, will be done online once CMS is in operation, using high energetic lepton tracks.

With the adopted solution for CMS as described previously, the position of the track of each particle traversing the tracker is measured at least eight times within the tracker (Fig. 4.5a), without putting an excessive amount of material in its way: the material encountered by a traversing particle does not exceed 0.9 radiation lengths (Fig. 4.5b).

Table 4.2: The different types of barrel MSGC modules used in CMS. The 'two-dimensional' configurations are made of two layers of MSGCs, the second layer being rotated with respect to the first. In the  $z$ -direction, a spatial resolution of  $300 \mu m$  is sufficient, which allows to enlarge the pitch of the stereo modules to  $400 \mu m$  and halve the number of electronics channels.

type	module length [mm]	strip length [mm]	# strips
1-dim	250	250	512
	125	125	512
2-dim	250	$2 \times 125$	$2 \times 512$
	250	250	$2 \times 256$
	125	125	$2 \times 256$
	250	$2 \times 125$	$2 \times 2 \times 256$

This is important for ensuring a good momentum resolution by reducing the amount of multiple scattering. A second aspect is the production of Bremsstrahlung photons which could reach the electromagnetic calorimeter (ECAL) surrounding the tracker. An excessive amount of Bremsstrahlung would limit the capabilities of the ECAL to detect especially the decay  $H \rightarrow \gamma\gamma$ . For the same reason, an additional shielding surrounds the whole tracker.

To be successful in pursuing the physics goals as described in chapter 2, the following requirements are imposed on the tracker:

- ) reconstruction efficiency  $> 98 \%$ ,
- ) rate of erroneously reconstructed tracks  $< 1 \%$ ,
- ) momentum resolution around  $\Delta p_T/p_T = 0.15 p_T [TeV/c]$ .

To allow the desired track reconstruction efficiency, each of the three technologies used in the tracker has to deliver a hit efficiency of  $\geq 97 \%$ . Furthermore, the Silicon Strip and MSGC modules are mounted in the tracker with a slight overlap so that particles cannot escape undetected through insensitive 'cracks'. The tracker covers the whole rapidity range up to  $-2.5 < \eta < 2.5$ . In this volume the trajectory of each traversing particle is sampled between 8 and 13 times, where more than half of them are true space points <sup>2</sup>. Together with the high magnetic field of  $4 T$  and the good spatial resolution of the detectors as described in this chapter this makes a

---

<sup>2</sup>This is true for particles with  $p_T > 0.8 GeV$ . Particles with lower momentum do not escape the magnetic field but spiral into the end-caps.

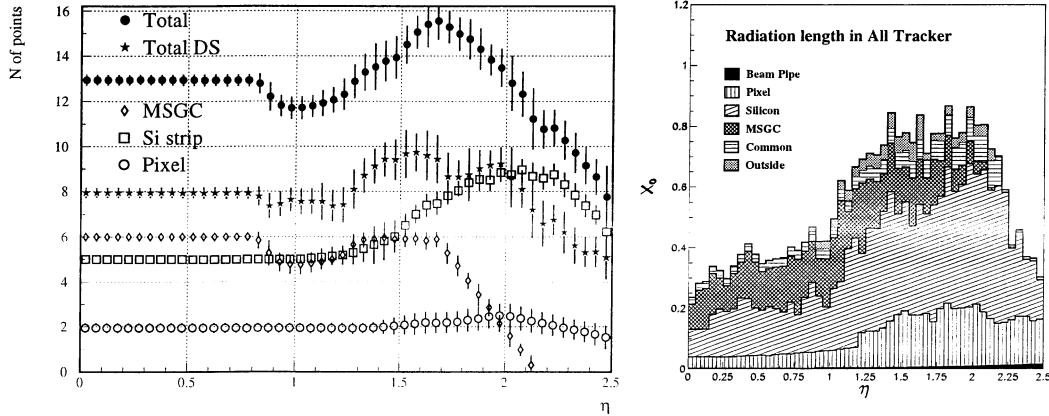


Figure 4.5: Number of layers versus rapidity: The position of the track of each particle traversing the tracker is measured at least eight times to allow precise momentum reconstruction. Still, the necessary material does not exceed 0.9 radiation lengths.

Table 4.3: Reconstruction efficiencies of the tracker for different particles above a min.  $p_T$ .

	min. $p_T$	$eff_{reconstr.}$
muons	1 $GeV$	98 %
charged hadrons	10 $GeV$	95 %
	1 $GeV$	85 %
electrons	10 $GeV$	70 %

momentum resolution  $\Delta p_T/p_T = 0.15 p_T \oplus 0.5 [TeV/c]$  possible for  $|\eta| \leq 1.6$ , gradually degrading by a factor 4 when  $\eta$  approaches 2.5. In combination with the muon chamber system the momentum resolution for muons with  $p > 100 GeV$  can be parametrised as  $\Delta p/p \approx 0.045 \sqrt{p} [TeV]$  for  $\eta \leq 2.0$ , resulting in a momentum resolution better than 10% even at 4  $TeV$ .

The fine granularity of the detecting elements is also crucial for disentangling the tracks of the several thousand particles created in each collision. This situation is illustrated in a simulated bunch crossing shown in Fig. A.1. Transverse impact parameter resolution is better than  $35 \mu m$ , in the direction of the beam it ranges from 40 to  $200 \mu m$  in both cases for particles up to  $\eta \leq 2.5$  and  $p_T > 10 GeV$ . The reconstruction efficiencies for various particles is given in Table 4.3.

# Chapter 5

## Microstrip Gas Chambers

In 1968 Charpak [37] introduced the multiwire proportional chamber (MWPC). Basically representing a series of parallel wires, each acting like the wire in a proportional drift tube, the MWPC allowed to determine the space-like position of the track of a traversing particle. First prototypes already achieved a resolution of a few  $100 \mu m$ . In 1978 a  $10 \times 10 \text{ cm}^2$  chamber was built that featured a resolution of  $60 \mu m$  [38]. During the last decades MWPCs have become a well established detector technology. In one form or the other, they can be found in all four LEP experiments at CERN and have operated reliably for almost ten years.

In 1988 Oed [39] proposed a new detector technology. Starting from the experience gained with MWPCs he developed a miniaturised form of this device. Sense wires suspended in the gas are replaced by metal strips that are etched on a glass substrate in a photolithographic process. Thus, the distance between wires could be reduced from a former  $1 \text{ mm}$  to a few  $100 \mu m$  without encountering problems due to electrostatic forces between the wires. This allows the new technology to deal with much higher particle densities, as the occupancy of the particle sensing elements is kept low.

### 5.1 Working Principle of Gaseous Detectors

Electrically charged particles traversing a medium interact inelastically with the atoms of the medium, thereby losing energy along their path. These interactions are of electromagnetic nature, since the strong and weak interaction probabilities are many orders of magnitude smaller. Depending on the mass and initial energy of the incident

particle, the probability for different electromagnetic interaction processes can vary.

One way is the collision of a particle with the atoms of the medium leading to excitation of the atoms (possibly followed by the emission of photons) and ionisation. It is these processes that create the primary electrons which trigger the signal formation in the MSGCs.

### 5.1.1 The Ionisation Process

A charged particle loses some of its kinetic energy by knocking out one or more electrons from the atoms it encounters when traversing matter. In a gaseous medium, typically a few tens of eV are necessary to produce one electron-ion pair, around 10 times more than what is needed in a semiconductor. The primary electrons themselves can have enough energy to further ionise atoms, usually close to the original track <sup>1</sup>. These newly liberated electrons, together with electrons emitted from atoms in metastable states created by the original particle are called secondary electrons.

They form clusters with a cluster size distribution that can be determined by Monte Carlo simulations or experimentally, by e.g. [40] (see Fig. 5.1). The number of

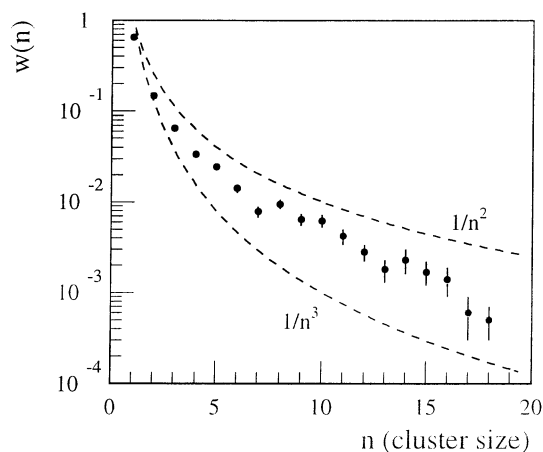


Figure 5.1: Experimental cluster size distribution for Argon as determined by [40].

clusters  $k$  produced by a particle traversing a certain length  $L$  of gas follows a Poisson

<sup>1</sup>High energetic electrons (Delta electrons) and photons can create electron-ion pairs at much larger distances – an unwanted effect whose occurrence can be reduced by adding so-called quenchers to the gas (see later).

distribution

$$P(L/\lambda, k) = \frac{(L/\lambda)^k}{k!} \exp(-L/k), \quad (5.1)$$

where  $\lambda$  is the mean free path between collisions,  $\lambda = 1/(N\sigma)$ , with  $N$  the density of electrons in the medium and  $\sigma$  the interaction cross section per electron. Thus, once cluster size and number-of-clusters distributions are known, the energy loss distribution  $F(E)$  of a traversing particle can be obtained by convoluting the two distributions.

Following general arguments, Landau [41] determined an analytic expression by making the ansatz

$$\frac{\partial}{\partial x} F(x, \Delta) = \int_0^\infty F(E) [F(x, \Delta - E) - F(x, \Delta)] dE, \quad (5.2)$$

where  $F(x, \Delta)$  denotes the probability that a particle loses the energy  $\Delta$  over a path length  $x$ . Inserting for  $F(x, \Delta)$  its Laplace representation  $\bar{F}(x, p) = \int F(x, \Delta) e^{-p\Delta} d\Delta$ , the differential equation can be solved. Using the  $d\sigma/dE \sim 1/E^2$  for Rutherford scattering<sup>2</sup> in order to calculate  $F(E)$  analytically, Landau obtained a general expression for the energy loss distribution: It can be expressed with a generic function  $\Phi$ .

$$F(x, \Delta) = \Phi\left(\frac{\Delta - \Delta_{mp}}{\xi}\right), \quad (5.3)$$

with  $\Delta_{mp}$  being the most probable value of the energy loss, and  $\xi = x \cdot \rho \cdot Z/A \cdot 1/\beta^2 \cdot 0.1536 \text{ MeV}/(g/cm^2)$  being the width of the distribution.

$\Phi(\lambda)$  can be approximated as

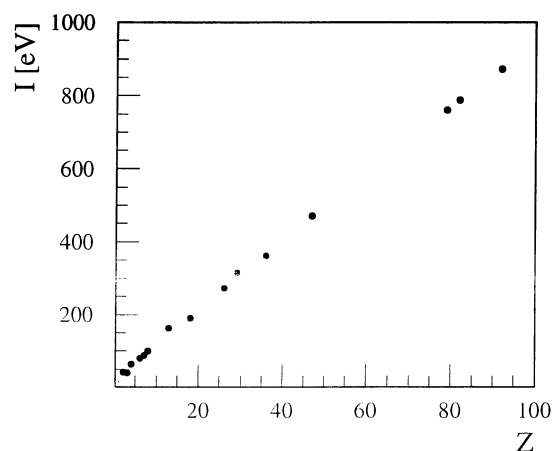
$$\Phi(\lambda) = \frac{1}{\sqrt{2\pi}} \exp\left(-\frac{1}{2}(x + \exp(-x))\right). \quad (5.4)$$

The average energy loss of a particle traversing a medium has been calculated by Bethe in 1930 and is expressed in the Bethe-Bloch formula [42],

$$\frac{dE}{dx} = \frac{4\pi N_0 \rho e^4 Z}{mc^2 A \beta^2} z^2 \left( \log \frac{2mc^2}{I} \beta^2 \gamma^2 - \beta^2 - \frac{\delta(\beta)}{2} \right). \quad (5.5)$$

$I$  is the mean energy necessary to produce one electron/ion pair, and is shown in Fig. 5.2.

<sup>2</sup>This expression is valid if the energy of the traversing particle is much higher than the highest atomic binding energies of the medium. In this case the traversing particle sees the electrons as free electrons in the collisions.

Figure 5.2: Estimates of  $I$  for some elements [43].

### 5.1.2 Drift of Electrons

The common theme among all drift chambers is the three step sequence "creation of primary electrons – moving of these electrons to a multiplication region – and multiplication and signal detection".

The movement of the electrons is governed by the electric field in the chamber (the drift field) and – possibly – a magnetic field present in the detector. The general equation of motion can be written as

$$m\dot{\mathbf{v}} = e\mathbf{E} + e(\mathbf{v} \times \mathbf{B}) - R\mathbf{v}, \quad (5.6)$$

where the friction term  $R$  is a function of the mean free path of the particle in the gas. When we look for the steady state  $\dot{\mathbf{v}} = 0$ , and define  $\tau = m/R$  a constant of dimension time and  $\omega = (e/m) |\mathbf{B}|$  the cyclotron frequency, Eq. 5.6 reduces to a set of linear equations in  $(v_x, v_y, v_z)$ :

$$M\mathbf{v} = e/m \mathbf{E}, \quad (5.7)$$

where  $(e/m) M^{-1}$  is a tensor, called the mobility. Explicitly writing out and inverting  $M$  we get

$$\mathbf{v} = \frac{e}{m} \tau |E| \frac{1}{1 + (\omega\tau)^2} (\mathbf{e} + \omega\tau(\mathbf{e} \times \mathbf{b}) + (\omega\tau)^2(\mathbf{e} \cdot \mathbf{b})\mathbf{b}). \quad (5.8)$$

where  $\mathbf{e}$  and  $\mathbf{b}$  are the unit vectors in direction  $\mathbf{E}$  and  $\mathbf{B}$ , respectively.

In the absence of a magnetic field,  $\mathbf{v}$  is parallel to  $\mathbf{E}$  and the mobility tensor reduces

to a scalar  $\mu = |\mathbf{v}| / |\mathbf{E}| = e/m \tau$ . From the microscopic point of view, the electron scatters isotropically on many atoms along its way. Between collisions it gets accelerated by the electric field. If  $\tau$  denotes the time between collisions, the electron gains in speed by  $\Delta v = (e/m)E\tau$ , which compares with the macroscopic considerations above and gives an interpretation of  $\tau$  as the mean time between collisions.

In the case of the CMS barrel region, a solenoid produces a magnetic field parallel to the axis of the detector and orthogonal to the electric field in the MSGCs,  $(\mathbf{e} \cdot \mathbf{b}) = 0$ . Let  $\mathbf{B} = (0, 0, B_z)$  and  $\mathbf{E} = (E_x, 0, 0)$ , and we get from Eq. 5.8

$$v_z = 0, \quad \tan \psi := \frac{v_y}{v_x} = -\omega\tau. \quad (5.9)$$

$\psi$  is called the Lorentz angle. It is the angle between the electric field and the actual direction of movement of the drifting electrons. We see that this angle does not depend on a rotation of the coordinate system in the  $(x, y)$ -plane, or equivalently, on a rotation of  $\mathbf{E}$  in this plane. Thus, by tilting the MSGCs in CMS by an angle  $\psi$ , it is possible to make the drifting electrons move on a path parallel to the track of the original particle coming from the interaction point. This improves the position resolution of the detector, as illustrated in Fig. 5.3.

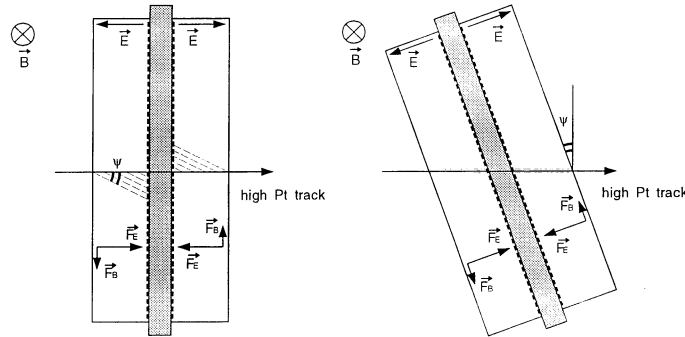


Figure 5.3: Correction of the Lorentz angle in the barrel MSGCs. By tilting the chambers the position resolution can be improved [32].

### 5.1.3 Charge Amplification

The closer the drifting electrons come to the positively charged electrodes, the more they become accelerated by the electric field which increases with decreasing distance  $r$  to the wire as  $E \sim 1/r$ . Thus, if only the electron is sufficiently close to the wire, it can



gain enough energy between collisions with the gas atoms to collide inelastically and liberate another electron in the gas which itself can ionise further atoms, and charge multiplication sets in. This avalanche continues to grow and move towards the anode until all electrons are collected by the wire, and the ions are left over. This process takes only fractions of a nanosecond.

Different scenarios of avalanche development depending on the strength of the electric field are possible: When the field is too low, electrons and ions recombine before the electrons can reach the wire. In an intermediate region the amount of charge in the avalanche is proportional to the number of electrons that started the avalanche. If the field strength is very high, the increasing space charge of the positive ions reduces the effective field, and proportionality is lost. Increasing the field even further gets the chamber first into the streamer regime and then lead to a breakdown, i.e. a complete discharge of the chamber [44].

The proportional regime is characterised by an increase of electrons in the avalanche proportional to the number of existing electrons, the change per path length being  $\Delta N = N\alpha \cdot \Delta s$ , where  $\alpha$ , the so-called Townsend coefficient, depends on the interaction cross sections of the gas. Integrating from the furthest distance from the wire  $s_{min}$  where amplification sets in, up to the wire radius  $a$ , we get the ratio of total to initial number of electrons.

$$\frac{N}{N_0} = \exp \int_{s_{min}}^a \alpha(s) ds. \quad (5.10)$$

Assuming  $\alpha$  to be proportional to  $E$ ,  $\alpha = \beta E$ , and substituting  $ds \rightarrow dE$  via  $E = k/r$  in Eq. 5.10, Diethorn [45] derived an expression for the gain  $G = N/N_0$

$$\ln G = \beta k \ln \frac{k}{aE_{min}}. \quad (5.11)$$

The factor of proportionality  $\beta$  between  $\alpha$  and  $E$  can be interpreted in the following way: The potential difference  $\Delta V$  between  $a$  and  $s_{min}$  is

$$\Delta V = \int_a^{s_{min}} E(r) dr = k \ln \frac{s_{min}}{a} = k \ln \frac{k}{aE_{min}}. \quad (5.12)$$

If the average energy to liberate one electron is  $I$ ,  $Z = \Delta V/I$  generations of electrons are produced, with a total number of  $G = 2^Z$  electrons. Inserting Eq. 5.12 into the expression for  $Z$  and using Eq. 5.11, we get  $\beta = \ln 2 / I$ . We see that in this model, the Townsend coefficient is proportional to  $E/I$ .

## 5.2 The detecting elements

Fig. 5.4 shows the cross section of an MSGC. On a glass substrate with an area of up to  $10 \times 25 \text{ cm}^2$  a strip micro pattern is etched. Above the substrate a 3 mm high gap filled with gas serves as the ionisation medium. The micro pattern consists of an alternating series of gold strips, being anodes and cathodes, 7 and 93  $\mu\text{m}$  wide, respectively, and up to 25 cm long. Their thickness is  $\sim 0.6 \mu\text{m}$ .

The drift plane that together with the substrate and the PEEK<sup>3</sup> frame, delimits the

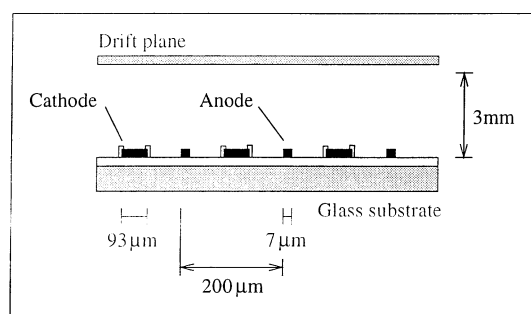


Figure 5.4: Cross section of an MSGC module.

gas volume, is made of metalised carbon fibre. A high electric field between drift plane and substrate makes the electrons liberated by a traversing ionising particle drift towards the substrate. There, a negative field from the cathodes to the anodes focuses the electrons towards the anodes where the electron multiplication takes place. The signal induced by the resulting ions drifting in the opposite direction is read out from the anodes. Fig. 5.5 shows a sketch of the electric field lines in the MSGC.

The substrate is made of glass (Desag D263). Being an insulator it has the disadvantage of charging up when an electric field is applied to the cathodes for electron multiplication. This is due to the fact that not all field lines emerging from the anodes reach the cathodes but end on the substrate. Thus, ions following these field lines end up on the substrate, reducing the original electric field. This can reduce the gas gain by up to a factor 4 [47]. The process is a short term effect and reversible, but much slower than the response time of the detector and harmful side effects are non-uniformities in gain which are introduced over the active chamber volume.

In order to reduce the decrease in gain to  $\sim 10\%$ , a thin conductive layer is deposited onto the substrate before etching the strip pattern onto it. This is achieved

<sup>3</sup>Poly Ether Ether Ketone

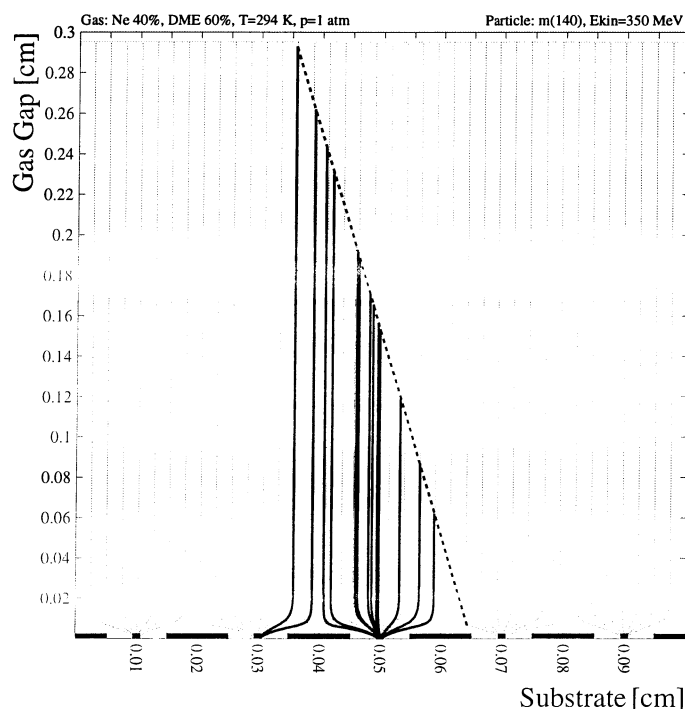


Figure 5.5: The electric field in an MSGC. Electrons of ionised atoms along the track drift along the field lines towards the anodes. (Field simulation using Garfield [46])

by sputtering a less than  $1 \mu\text{m}$  thin layer of Pestov glass – a semiconductive glass with electronic conductivity – onto the substrate. Unfortunately such a conductive layer reduces the gain of the chamber by modifying the electric field near the electrodes, which has to be compensated by operating the chamber at higher voltages. It has been shown that with the highest surface resistivities of  $\sim 10^{16} \Omega/\square$  compatible with the goal of keeping the charging-up effect lower than  $\sim 10\%$ , a moderate increase of  $\Delta V_{\text{cathode}} = 15 \text{ V}$  is sufficient to maintain the desired gain [47].

The anode and cathode strips are made of gold. Advantages are a low resistivity ( $< 40 \Omega/\text{cm}$ ), which reduces signal attenuation along the strips and reduces noise, and its chemical inertness: Gold does not react with the ions produced during the multiplication process, and also makes it difficult for polymers originating in the gas to attach to the strips. Thus, this choice of material helps to drastically reduce aging of the MSGCs (see chapter ??).

The patterning technique chosen for etching the electrode structure is a succession of photolithographical definition of the strip pattern, metal deposition and

chemical lifting off of the unwanted metal (see Fig. 5.6).

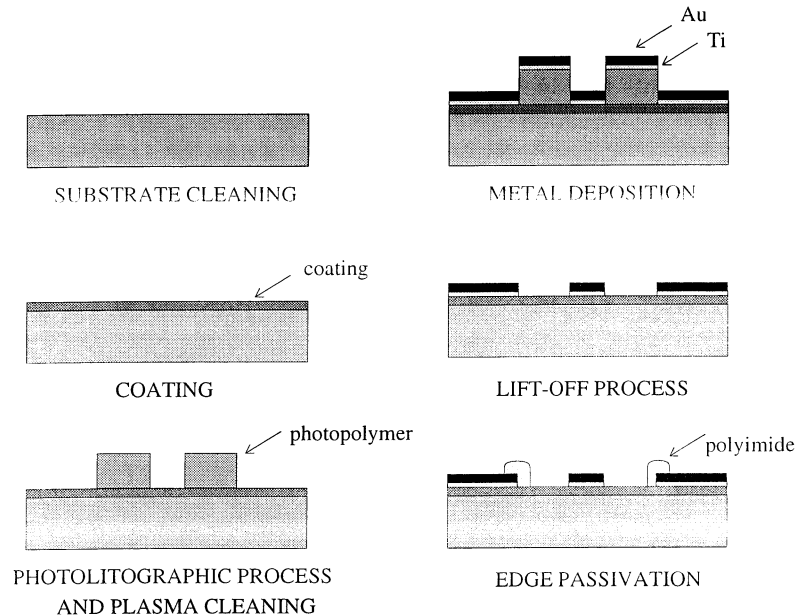


Figure 5.6: The patterning technique: Before the metal deposition a photopolymer covers the areas of the already coated substrate which should be left blank. It is then chemically washed away (lift-off process). In a last step the critical edges of the pattern structure are passivated [32].

On the edges of the micro pattern strips the electric field gradient takes its maximum values. There, electrons can be extracted and initiate a discharge of the whole cathode to the anode, which could – in extreme cases – damage the anode. The probability of discharges limits the range of safe operating voltages. In order to increase the safety margin, both ends of the strips are 'passivated': besides rounding off the far end of the anodes (Fig. 5.7) a  $200\ \mu\text{m}$  wide polyimide layer is added on top of the gold pattern, at the detector border across all strips. This material has a very high dielectric strength of  $\sim 30\ \text{kV/mm}$ . Similarly, all cathode edges are covered by a few  $\mu\text{m}$  thin layer (Fig. 5.4) - this prevents electron extraction but does not alter the electric field at the anodes significantly [48].

The gas used in the active volume of the chambers is a mixture of neon and DME <sup>4</sup>, in the ratio  $\text{Ne/DME} = 40/60$ . Several considerations had to be made before choosing

<sup>4</sup>DME ... Di-Methyl Ether.

Ionisation density = number of primary clusters  $\times$  cluster size =  $60 \times 3\ \text{e}^-/\text{cm}$  at  $2\ \text{GeV}/c$

Ionisation potential =  $10\ \text{eV}$ .

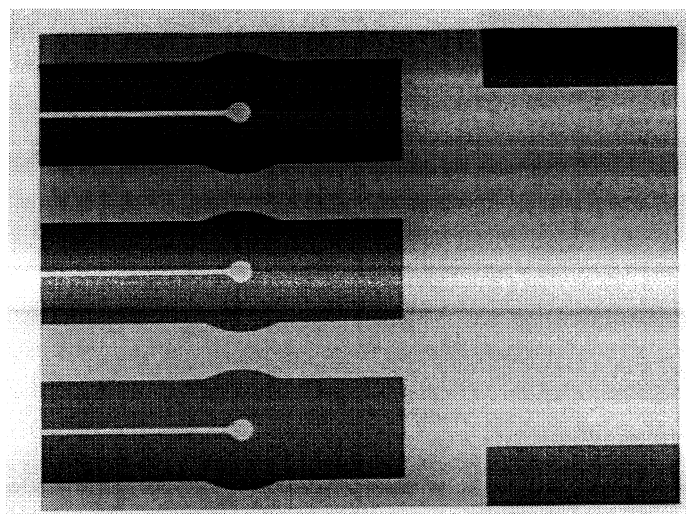


Figure 5.7: Detail of the micro pattern structure: the anode edges are rounded to reduce the risk of discharges [32].

this mixture:

- $dE/dx$  and gas gain high enough for an acceptable signal-to-noise ratio,
- fast primary charge collection but small Lorentz angle,
- the least possible aging,
- lowest possible working voltages and maximum safety margin.

The best compromise considering all the above requirements was found to be a mixture Ne/DME=40/60. The total primary charge liberated by a minimum ionising particle in this gas is  $\sim 40 e^-$ , as compared to  $\sim 60 e^-$  in pure DME. but high gains can be reached at lower voltages and thus full efficiency at LHC running conditions is already obtained at  $V_{cathode} = 520 V$ .

At this operating point the safety margin is around  $100 V$  (see chapter 5.6). This is due to the fact that DME is a very effective UV photon absorber, whereas Neon, as opposed to Argon or Xenon, is a moderate UV scintillator [49]. The danger with UV photons is, that they can extract electrons from the metal electrodes, which induce discharges in the case where electrodes are very close to each other, like it is the case in MSGCs. But also the production of polymers in the avalanche plasma, and thus aging by electrode coating, is catalysed by UV photons. However, the use of DME brings some complications. Apart from being a poisonous and flammable gas and thus must be treated with special care, it is also highly chemically reactive, which compels the

use of stainless steel tubes, special epoxy glue <sup>5</sup> and crystalline PEEK for the chamber frame and gas system sealings.

## 5.3 The Electronics

### 5.3.1 The High Voltage Part

Discharges of the cathodes to the anodes constitute the main physical process that can limit the lifetime of the MSGCs at high rates with heavily ionising particles. 512 cathode strips are supplied with a voltage  $V_{cathode} = 520 V$  at nominal working conditions. The capacitance of the 25 cm long strips is 8 nF. In case of a discharge of the cathodes, the energy stored in the whole detector capacitance would thus be sufficient to destroy the anodes which have a diameter of only  $7 \times 0.6 \mu m^2$  [48]. In order to reduce the charge that is released in such an event, the cathodes are subdivided into groups of 16, each group being connected to high voltage via a 100 kΩ resistor (see Fig. 5.9). Fig. 5.8 shows two current spikes in an MSGC recorded during operation in

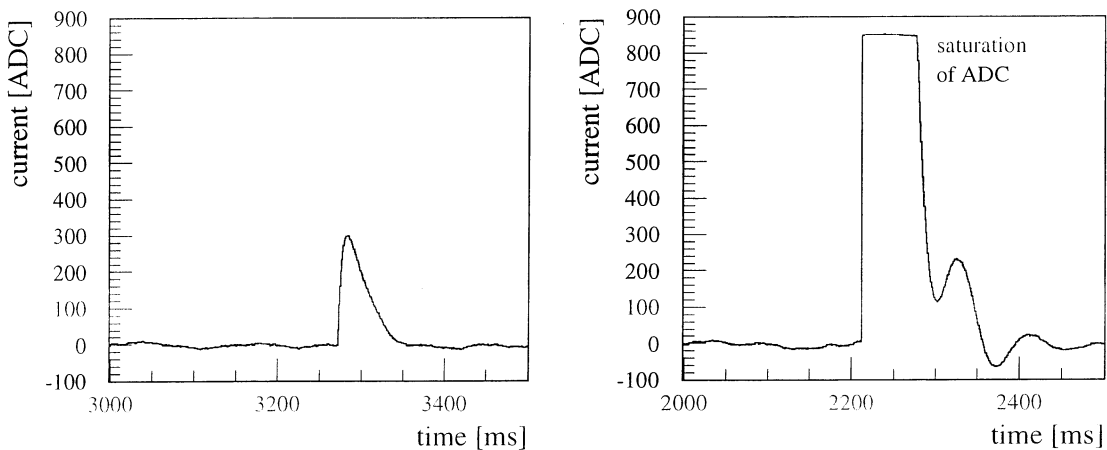


Figure 5.8: Currents spikes measured during operation of the chamber in a 350 MeV  $\pi^+$  beam. (a) is a current spike corresponding to a streamer triggered by the passage of a nuclear fragment, (b) shows a discharge of a group of 16 cathodes.

a beam similar to the secondary particle spectrum at LHC. For the final power supply system that will be used in CMS, each group of 16 cathodes will be equipped with a

<sup>5</sup>Araldite 2011, produced by CIBA, GB. See also [50]

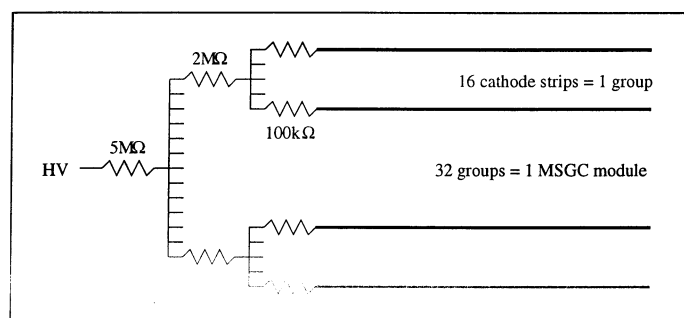


Figure 5.9: The resistive network supplying high voltage to the cathodes.

remotely operable switch, to allow single groups to be turned off in case of faults like e.g. electrical shorts between anodes and cathodes that develop during operation of the detector.

The drift plane is fed with  $3500\text{ V}$  over a  $50\text{ M}\Omega$  protection resistor. Cathode- and drift current will both be monitored to a precision of  $\sim 1\text{ nA}$  by the power supplies (C.A.E.N. SY694 systems).

### 5.3.2 The Read-Out Chain

Each strip is connected to a charge sensitive amplifier with a time constant of  $50\text{ ns}$ . As a first level trigger decision can take up to  $3\ \mu\text{s}$ , the analog signals have to be temporarily stored in a pipeline. A deconvolution algorithm can then reconstruct the appropriate amount of charge collected by the strip for the bunch crossing of interest. Via a multiplexer the pulse-height of all 512 strips is then sequentially transferred to optical converters and sent to the underground counting room via  $100\text{ m}$  long fibre optic links.

There, the Front End Driver (FED) digitises the analog data, performs pedestal subtraction and keeps the information available for the higher level data acquisition. Eventually some cluster finding algorithm could be implemented in order to reduce storage and data transfer requirements. A detailed discussion of the electronics can be found in [51].

To date, this electronics has been developed and is in its test phase [52]. However, the MSGC modules that were investigated for this thesis have not yet been equipped with the new electronics. Instead, the non-radiation hard PreMux electronics was used, which is in its main features (amplifier, shaper) equivalent to the final electronics, and

only lacks the deconvolution circuit for bunch crossing identification.

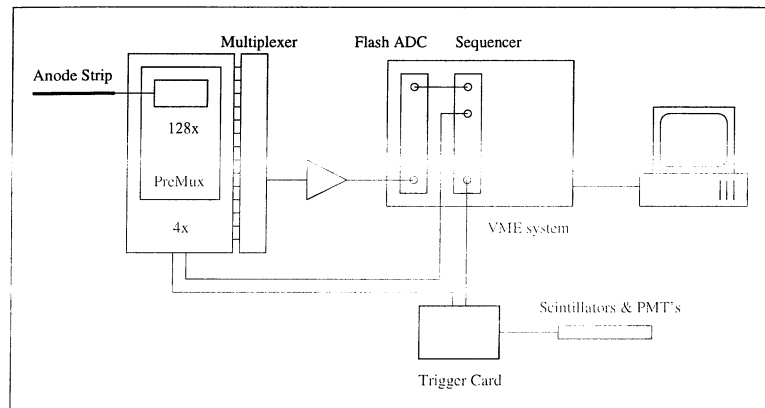


Figure 5.10: Schematic picture of the PreMux electronics and read-out chain employed by all the MSGCs used in the laboratory and test beams during this thesis.

The on-board electronics of each MSGC contains four PreMux128 chips, each reading out 128 anode strips. Each channel features a pre-amplifier, a shaper and a double correlated sampler. An analog multiplexer transfers the pulse height information of all channels to the VME based 1 MHz Flash ADC ('Sirocco') via a differential ECL cable. The whole chain is controlled by a sequencer, which itself is timed by the external trigger system. Both the flash ADC and the sequencer have been developed at LEPSI, France [53].

The charge sensitive pre-amplifier produces an output of  $5\text{ mV}$  for every 24000 electrons generated at the anode. In order to shorten the resulting signal, a shaper is used, whose output peaks at  $\sim 45\text{ ns}$  after the avalanche creation at the anode. The purpose of the double correlated sampler is the following: Two samples of the output of the shaper are taken – one at the expected time of the peak of the signal and one  $800\text{ ns}$  after, when no signal is present – and stored intermediately in two capacitors ( $2\text{ pF}$  each). By looking at the difference between the charges stored in these capacitors, the anodic charge can be deduced, while errors due to e.g. radio frequency interference can be eliminated (see Fig. 5.11). This difference in charge is then again amplified and sent to the external ADC.



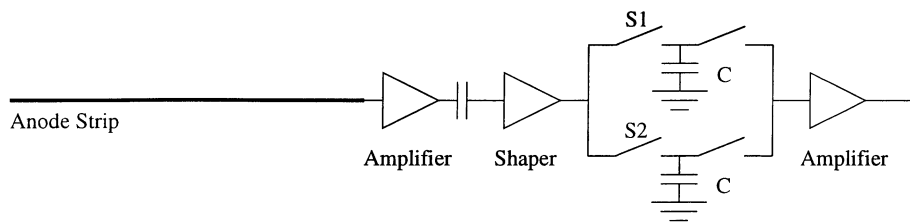


Figure 5.11: The schematic circuit of the PreMux with the switches  $S1$  and  $S2$  double correlated sampling is performed.

## 5.4 Analysis of MSGC Signals

At each trigger the 512 anode strips are read out sequentially and the output is digitised. In order to obtain information on where the triggering particle has traversed the chamber, several steps of signal processing are necessary.

1. **Baseline jumps:** In a first pass events in which more than ten consecutive readout channels show increased ADC values are marked as 'bad', as they are manifestations of so-called base line jumps of the pre-amplifier electronics, caused by pickup noise or mismatch of timing signals.
2. **Pedestal subtraction:** An overall ADC offset per event is subtracted from the data represented by  $512 \times 2$  bytes per event.
3. **Common Mode subtraction:** The pre-amplifiers connected to the strips are grouped in units of 128 onto one read-out hybrid, the PreMux chip, of which there are four for each MSGC. Naturally they can vary from each other and show individual base line shifts. Thus, for each group containing 128 strips a common mean is calculated and subtracted from the data.
4. **Noise calculation:** For each strip the pedestal and common mode subtracted RMS of its ADC value over all events is calculated. This gives the noise for each strip.
5. **Hit finding:** Each traversing particle creates a cluster: Due to charge diffusion not only one strip gives a signal but several adjacent strips share the signal. In analysis terms a cluster is defined as the maximal group of strips with a Signal/Noise  $> 3$  that contains at least one strip with a Signal/Noise  $> 6$ . The ADC values of all these strips are added and give the total 'cluster charge'.

6. **Crosstalk correction:** As seen in Fig. 5.9, cathodes are connected in groups of 16 to the high voltage. When a signal is created on one anode by the ions moving towards the corresponding cathode, charge is drawn from that cathode, which is replaced by charge that the cathode 'borrows' from the 15 other cathodes in its group. Thus, signals of the opposite sign are induced on the anodes belonging to those cathodes, which shifts the base line of the ADC signals. This cross talk is corrected for during the analysis as graphically illustrated by Fig. 5.12.
7. **Iteration:** Pedestal, common mode and noise calculation for each strip are calculated over all events in which that strip is not hit. As a hit is only detected by the analysis after the above values are calculated, which themselves are 'disturbed' by non-detected hits, an iterative procedure is used which repeats the above sequence of points 1-5, until no new hits are identified during the iteration.

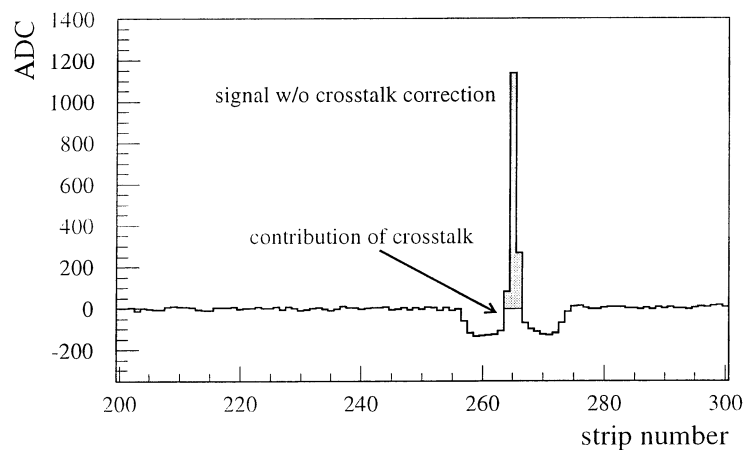


Figure 5.12: Cross-talk between strips corresponding to the same group of 16 cathodes.

## 5.5 Basic Performance of the MSGC

### 5.5.1 Gain of the MSGC: $\text{gain}(V_c, V_d, Ne\%)$

The role of various factors influencing the gain of the MSGC was investigated, using a  $3 \times 3 \text{ cm}^2$  small MSGC built with the same materials and featuring the same geometry of the strip pattern as the chambers that will be used in CMS. The electronics connected

to the chamber was PreShape32 with Laben 5185 pre-amplifiers. The chamber was irradiated with an  $\text{Fe}^{55}$  source. For the gain measurements the pulse height of the signals was measured with an oscilloscope and converted into the equivalent gain of the chamber using the formula

$$\text{gain} = \frac{650}{bd \cdot ct \cdot n_p} \cdot \text{pulseheight}[mV], \quad (5.13)$$

where  $bd = 0.65$  denotes the ballistic deficit due to the shaping of the signal,  $ct = 0.8$  is the capacitive crosstalk between two strips, and  $n_p = 200$  is the number of primary electrons created on average in the gas by the photons from the  $\text{Fe}^{55}$  source. In order to restore the baseline of the read out channel shortly after the creation of the signal by the avalanche process, the signal is shaped, i.e. its tail is suppressed, and thus the pre-amplifier only sees part of the whole charge of the avalanche. The difference between the amplified charge and the total charge collected by the strip is called the 'ballistic deficit'.

In order to collect all the electrons created liberated in the gas by the incident photons, four anode wires were grouped together before being fed into the pre-amplifier. Two wires on each side of the group of four were used as a veto: Whenever a signal was detected on these wires, the event was rejected, because the size of the electron shower would, in such a case, have been bigger than the area covered by the four read-out wires (see Fig. 5.13). A proportional tube was inserted into the gas system at the

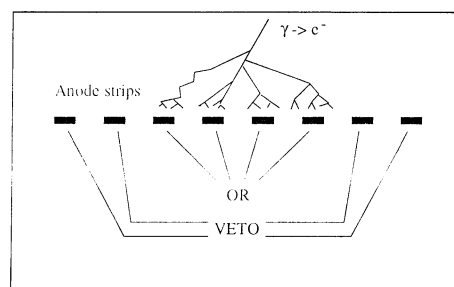


Figure 5.13: The read-out of the anode strips. Only events whose avalanche was localised to not more than the group of four connected strips were recorded.

output of the MSGC to monitor the consistency of the gas mixture by measuring the gain within the proportional tube.

In Fig. 5.14 we can see a graphical representation of the gain as a function of drift- and cathode voltage, taken with a gas mixture  $\text{Ne}/\text{DME}=33/67$ . Several mixing ratios

have been investigated, and the results are summarised in the appendix, Fig. A.6 and Fig. A.7. The left plots shows the exponential change of gain with the cathode voltage, with different symbols indicating different drift voltages, the right plot shows  $\text{gain} = \text{gain}(V_d)_{V_c=\text{const}}$ . Fig. A.5 is the legend explaining the different symbols.

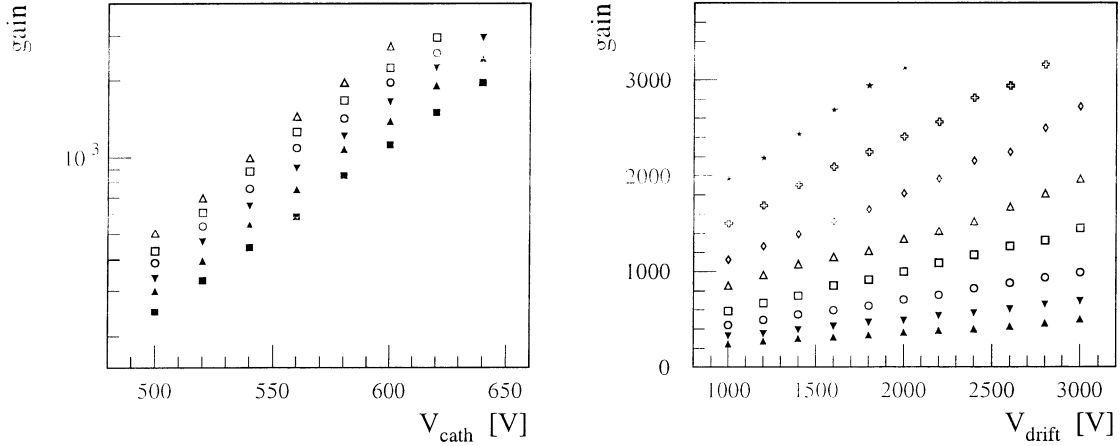


Figure 5.14: Gain in a Ne/DME=33/67 mixture. See the text.

Choosing one working point ( $V_{cathode}, V_{drift}$ ) and varying the Neon/DME ratio, we observe an exponential dependence of the gain on the Neon concentration,

$$\text{gain} = 111.2 \cdot \exp 0.0411 \cdot Ne\% . \quad (5.14)$$

Fig. 5.15a shows the corresponding fit. The same behaviour was also observed with a proportional tube (Fig. 5.15b). Thus, making the ansatz

$$\text{gain}(V_c, V_d, Ne\%) = N \cdot e^{p \cdot Ne\%} \cdot e^{a \cdot (V_c + b \cdot V_d)} , \quad (5.15)$$

and performing a three dimensional fit to all the data, we obtain

$$\text{gain}(V_c, V_d, Ne\%) = 1.89 \cdot 10^{-2} \cdot e^{0.0405 \cdot Ne\%} \cdot e^{0.0152 \cdot (V_c + 0.030 \cdot V_d)} , \quad (5.16)$$

which deviates not more than 10% from the data (corrections for pressure variations during the time of measurement have not been done). We see that for the chosen geometry the field gradient responsible for the gas amplification is determined by a combination of cathode- and drift voltage where the drift voltage has an influence of about 3%.

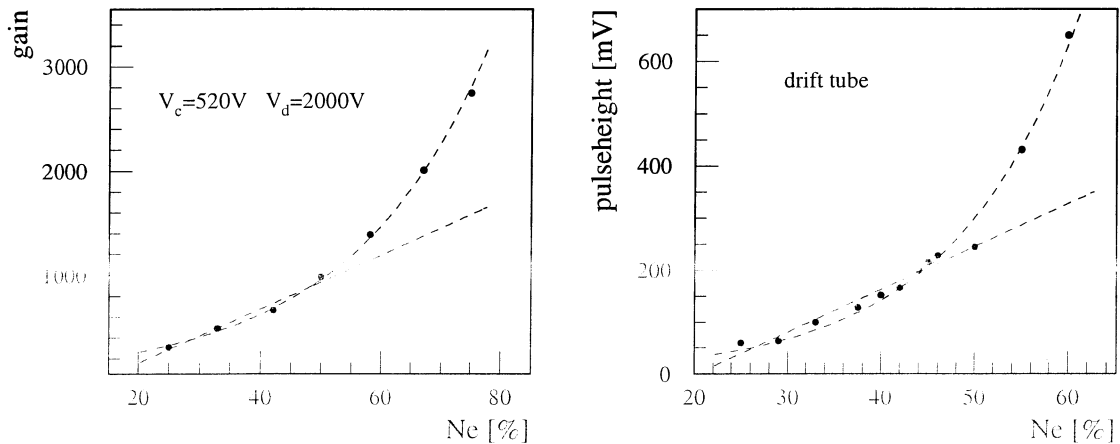


Figure 5.15: Dependence of gain on the Ne%. (a) MSGC, (b) drift tube.

### 5.5.2 Signal variations with pressure

The MSGCs when operated are exposed to fluctuations of the pressure of the gas due to changes of the atmospheric conditions. Thus, to guarantee good performance also under the worst possible working conditions, the effect of changing pressure on the performance of the chamber has to be determined.

Two effects influence the behaviour of the signal: An increase of pressure leads to a reduction of gain due to a reduction of the mean free path between collisions. Less secondary ionisation can occur because the electrons have less space to gain sufficient energy in the electric field to ionise gas atoms. At the same an increase of pressure leads to an increase of primary ionisation due to a higher gas density. The first effect reduces the gain exponentially, the second increases the signal amplitude linearly with increasing pressure. In everyday life, however, pressure changes due to fluctuations of atmospheric conditions are rather small, so that both effects go approximately linearly with the pressure, and, as the results will show, almost counterbalance each other.

The measurements were done with a VME setup using a LeCroy 1182 ADC. The schematics of the setup is depicted in Fig. 5.16. The chamber under test was flushed with a constant gas flow of 3 l/h. By reducing the opening of the output of the chamber with a needle valve, the pressure in the chamber could be increased, as shown in Fig. 5.17a. An electronic micro-manometer gave precise pressure readings between 1 and 25 mbar.

Three different working points ( $V_{cathode}, V_{drift}$ ) were chosen with gains of 1000, 2000

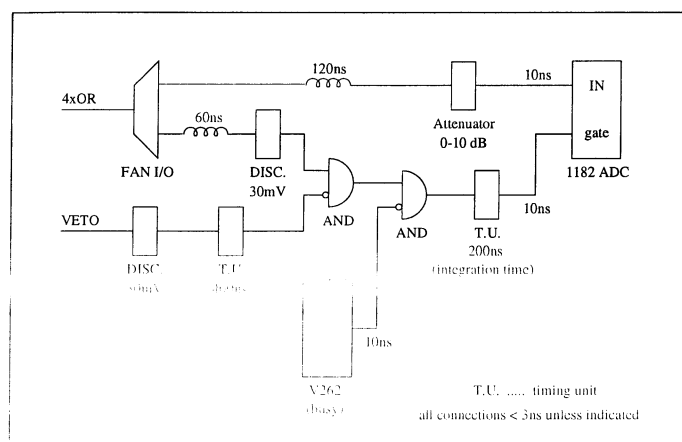


Figure 5.16: Read-out logic of the  $3 \times 3 \text{ cm}^2$  MSGC. The inputs '4xOR' and 'VETO' come from the two groups of strips depicted in Fig. 5.13.

Table 5.1: The gain variations with pressure for different nominal gains. The quoted values give the decrease of signal in % / *mbar*

Ne%	gain=1000	gain=2000	gain=3000
33%	-0.22%	-0.26%	-0.25%
50%	-0.29%	-0.27%	-0.27%
67%	-0.15%	-0.16%	-0.19%

and 3000 for each of the gas mixtures Ne/DME=33/67, 50/50 and 67/33. The drift plane of the chamber was reinforced by a plate of Vetronite in order to suppress possible mechanical deformations of the gas volume by pressure differences. For each initial gain in each gas mixture, the signal was measured as a function of pressure.

Table 5.1 gives the results for different combinations of gain and Ne/DME ratio: The numbers give the signal drop in percent of the initial gain per *mbar*. It is seen that the influence of pressure differences up to 20 *mbar* are rather small, on average about  $-0.2\% / \text{mbar}$ .

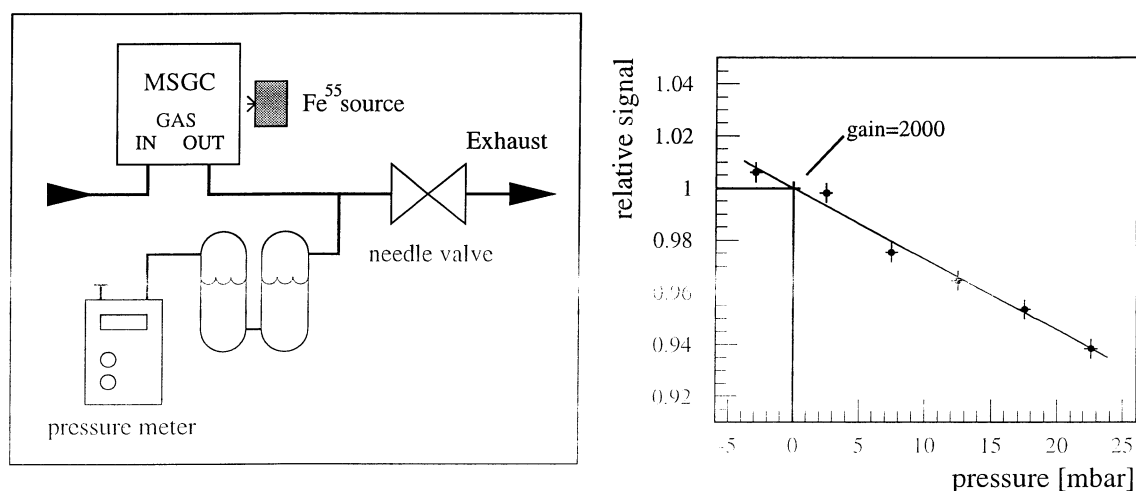


Figure 5.17: The pressure control system (a), and the decrease of the signal for increasing pressure for a Ne/DME=50/50 mixture at initial gain=2000 at 0 mbar over-pressure (b).

### 5.5.3 Mechanical deformation due to over-pressure

More significant than the effect it has on the gas is the effect over-pressure has on the electrical field in the chamber by mechanically altering the geometry of the chamber. The deformation of the PEEK drift plane and of the glass substrate of a  $10 \times 10 \text{ cm}^2$  MSGC (Fig. A.2) as a function of gas over-pressure was investigated. The chamber was put under a microscope and with the gas output closed, a static pressure of 1 and 2 mbar was applied at the input. The microscope was focused onto the drift plane at various points across the surface of the plane, and the deformation of the plane was read off the adjustment screw of the microscope.

Such deformations influence the gain uniformity of the module. The electric field around the anodes is determined by a combination of drift- and cathode voltage (Eq. 5.16). Enlarging the distance between electrodes and drift-plane has the same effect as reducing the drift voltage while leaving the chamber geometry unaltered and thus will decrease the field strength of the drift field and reduce the amplification. Fig. 5.18 shows the measured deformation across the chamber of both the PEEK drift plane and the glass substrate. The deformation increases linearly with the applied over-pressure (Fig. 5.19). Using Eq. 5.17 it is possible to calculate the displacement  $\delta$  of the centre of the drift plane and the glass substrate,

$$\text{deformation } \delta = \frac{C_3 b^4}{E d^3} p, \quad (5.17)$$

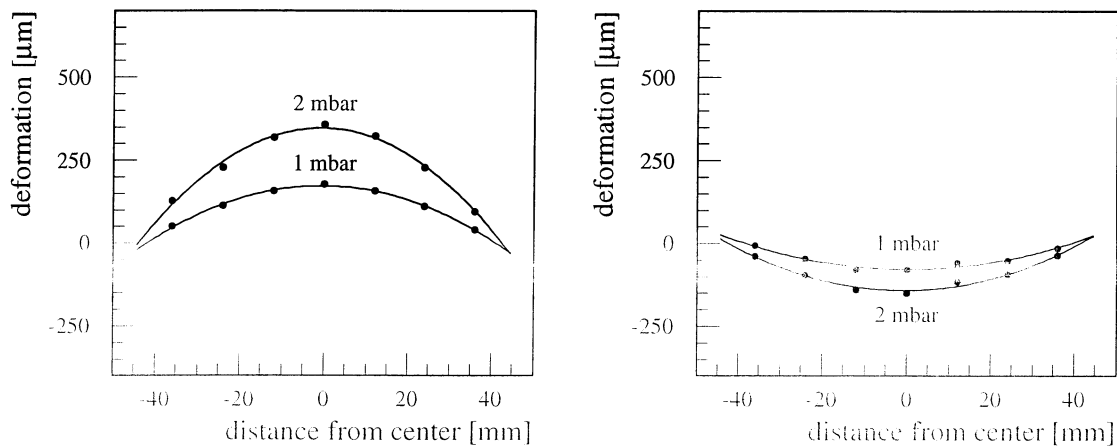


Figure 5.18: Deformation of the MSGC due to over-pressure. (a) PEEK drift plane, (b) 300  $\mu\text{m}$  glass substrate.

where  $C_3$  is a form factor,  $C_3 = 0.0138$  for quadratic plates,  $b$  is the size of the plate,  $d$  its thickness,  $E$  Young's modulus and  $p$  the applied pressure. With  $b = 10 \text{ cm}$ ,  $d = 300 \mu\text{m}$  and  $E = 70 \cdot 10^9 \text{ Pa}$ <sup>6</sup>, this gives a displacement of  $74 \mu\text{m}/\text{mbar}$ , which is well in accordance with the experimentally measured value of  $78 \mu\text{m}$  at  $1 \text{ mbar}$ .

Finite elements calculations [54] recommend using a drift plane made of carbon fibre epoxy to give more rigidity to the module. This material has a thermal expansion coefficient similar to the glass substrate, which helps avoid a bi-metal-like bending of the chamber when temperature fluctuates.

An example of an MSGC which exhibited a significant non-uniformity in gain is investigated in chapter 6.2.

#### 5.5.4 Effects of high rates

At LHC, the detectors will be faced with an extremely high flux of particles. Near the anodes, each particle generates a lot of gas ions, which drift along the field lines to the cathodes. Two known scenarios where these ions can have negative effects on the performance of the chamber are described in the following. Both lead to a reduction of gain of the chamber. Charging up of the substrate happens one on a time scale of

<sup>6</sup>For PEEK,  $E = 3.85 \text{ GPa}$ , for Vetronite  $E = 23 \text{ GPa}$ .



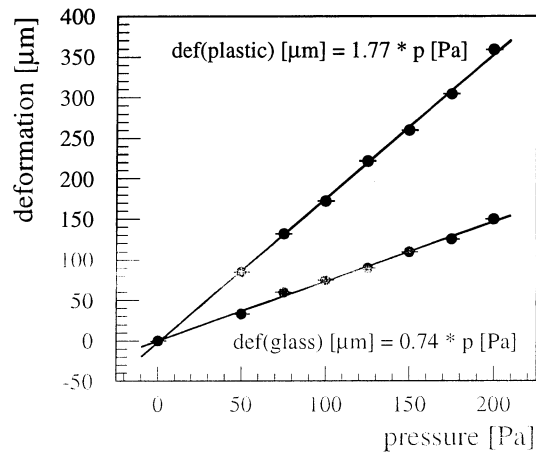


Figure 5.19: The linear behaviour of the deformation as a function of overpressure at the centre of the chamber.

seconds, aging of the electrodes during several years.

#### 5.5.4.1 Reduction of gain due to 'charging up'

The MSGCs, coming as close as 60 *cm* to the interaction point will be exposed to a rate of particles of up to 6 *kHz/mm*<sup>2</sup>, each particle producing an avalanche close to the substrate. Thus, charging up of the substrate can become a substantial problem. It is addressed with a thin layer of slightly conductive material that is sputtered onto the substrate to allow a 'draining' of the charge that lands on the substrate, as described in chapter 5.2. Fig. 5.20 shows that this coating indeed gives a substantial safety margin against charging up as compared to uncoated substrates: In the laboratory, an X-ray source with a rate of 100 *kHz/mm*<sup>2</sup> was pointed onto the chamber, and no decrease in signal current – which would indicate a gain reduction – could be observed.

#### 5.5.4.2 Reduction of gain due to 'aging'

Aging is an important issue when developing a new detector technology. Even more so for the MSGCs at CMS: The detector will be operated continuously for several years without the possibility of having access and changing parts. Thus, all technologies must work in a predictable way, and not deteriorate excessively during operation.

Aging in wire chambers and thus also in MSGCs denotes the effect of constantly

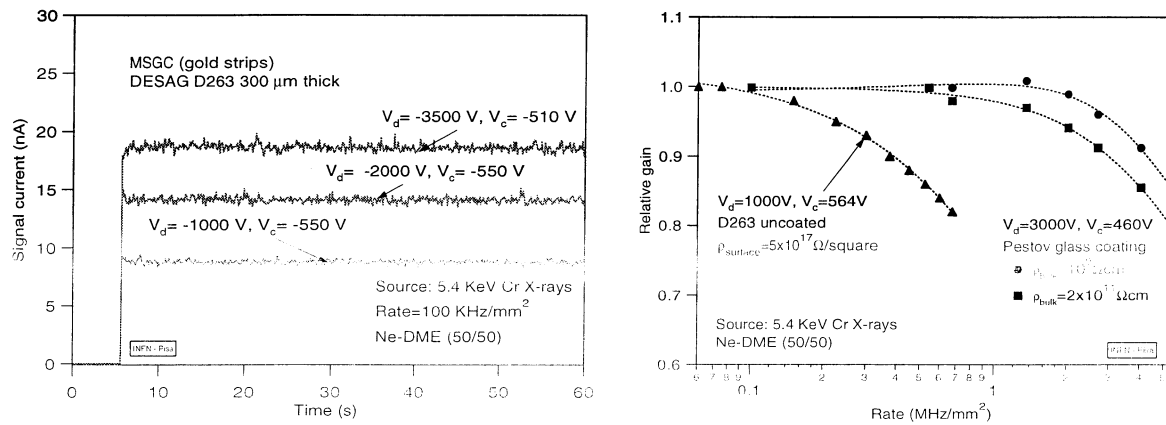


Figure 5.20: Charging up of the substrate would lead to a reduction in gain after the onset of irradiation. Coating of the substrate makes the MSGCs immune to this effect up to rates well exceeding the rates expected at LHC [47].

decreasing gain of a chamber over a long period (i.e. more than hours) of time. It is due to a growing layer of insulating material that gets deposited along the readout strips. The material consists mainly of polymerised organic compounds that originate from the gas. In the course of operation of the chamber, gas molecules become ionised in the avalanche and UV-light and can fuse together. As this happens in the vicinity of the anodes, they become deposited there. Being insulating, they can charge up and cause a weakening of the field gradient close to the anode strips and thus a reduction of gain.

For the MSGCs at CMS certain measures are taken to reduce the effect of aging as much as possible:

- lowest possible gas gain to minimise the charge produced at the strips
- gold strips, as gold is chemically inert and makes attachment difficult
- a gas mixture that does not lead to polymerisation: Neon produces little and DME absorbs very well UV photons, and on the other hand is difficult to polymerise.
- clean gases and distribution system and only tested materials and glue used for chamber construction.

In the laboratory [32], more than four years of operation at LHC were simulated with a high intensity  $\text{Fe}^{55}$  source (Fig. 5.21). The maximum current density at LHC that the MSGCs will experience is  $\rho_I = 70 \cdot 10^3 e^-/\text{particle} \times 10^4 \text{ particles}/s/\text{mm}^2 = 0.1 \text{ nA}/\text{mm}^2$ . The current density achieved in the lab was  $1.4 \text{ nA}/\text{mm}^2$ , giving an

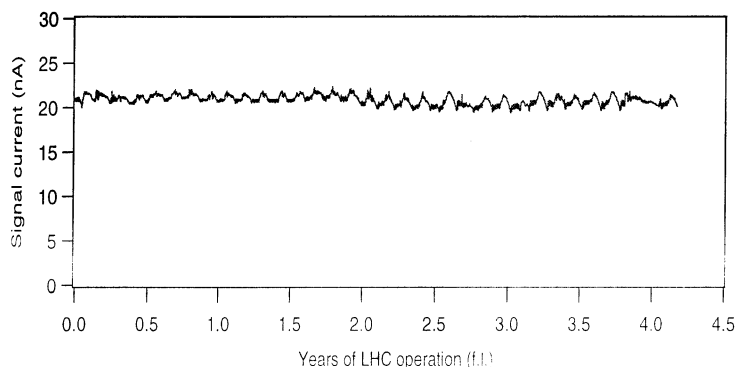


Figure 5.21: Aging behaviour over several years of integrated charge at LHC conditions. The fluctuations are due to day/night changes of temperature [32].

acceleration factor of 14. As the test lasted for 35 days, it covered a time equivalent to 4.2 years of operation at LHC (one nominal LHC year =  $10^7$  s).

## 5.6 Performance in test beams

The cluster size has been determined as a function of the neon concentration in the gas at working points with full detection efficiency [32]. Fig. 5.22 shows a linear increase of the cluster size as a function of the Neon concentration  $\Delta_{cluster} = 1.6 + 0.015 \cdot Ne\%$ . This is attributed to a higher diffusion in the noble gas than in the DME.

The nominal working point of the MSGCs at LHC :

In order to have full tracking efficiency, the MSGCs have to be operated at a working point with a signal-to-noise ratio of at least 20 (see Fig. 5.23). The electronics that is used to date, as described in chapter 5.3, does not have the deconvolution circuit built in that will be used in CMS for bunch crossing identification. This circuit will reduce the signal-to-noise ratio by a factor 2.2 [55], [56]. Thus, the working point with the current electronics is chosen to give a signal-to-noise ratio of  $S/N = 44$ . This can be achieved with a gain of  $\sim 1700$  (chapter A.2), which is reached with a drift voltage of  $V_{drift} = 3500$  V and a cathode voltage  $V_{cathode} = 520$  V in a Neon/DME mixture  $Ne/DME = 40/60$  (Fig. 5.24).

The hit resolution was determined in a test beam: Several MSGCs were aligned to track the traversing particles. In the offline analysis tracks were then fitted through

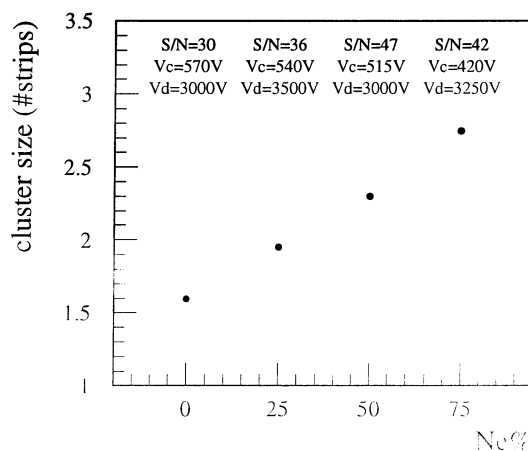


Figure 5.22: Average cluster size as a function of the Neon concentration and the operating point [32]. For a definition of the cluster size see chapter 5.4.

the data of all the chambers except one, whose data was compared to the extrapolated data from the fit. Fig. 5.25 shows the residual between the measured points and the extrapolated fit. The width of the distribution is  $\sim 35 \mu\text{m}$ . Deconvoluting the error on the fitted track that is introduced by the described method from the above distribution, an intrinsic track resolution of  $30.5 \pm 0.4 \mu\text{m}$  [57].

### 5.6.1 Operation in the LHC environment

From the above results we conclude that the MSGC technology fulfils all the requirements for purposeful operation in CMS as described in chapter 4.3. One important aspect has not been discussed yet. At LHC, the detectors in the inner tracker are faced with an extremely high flux of particles. The fluxes of particles that are expected to traverse the MSGCs has been shown in chapter 3.1.2. It contains mainly of MIPs (minimum ionising particles), but also a non-negligible fraction of nuclear fragments. When such particles reach the amplification region of the chamber, they can induce a streamer, which is an extended region where the gas is highly ionised. When this region is large enough to extend from an anode to a cathode, a discharge (Fig. 5.8) of this cathode to the anode can be triggered which may damage the micro pattern structure.

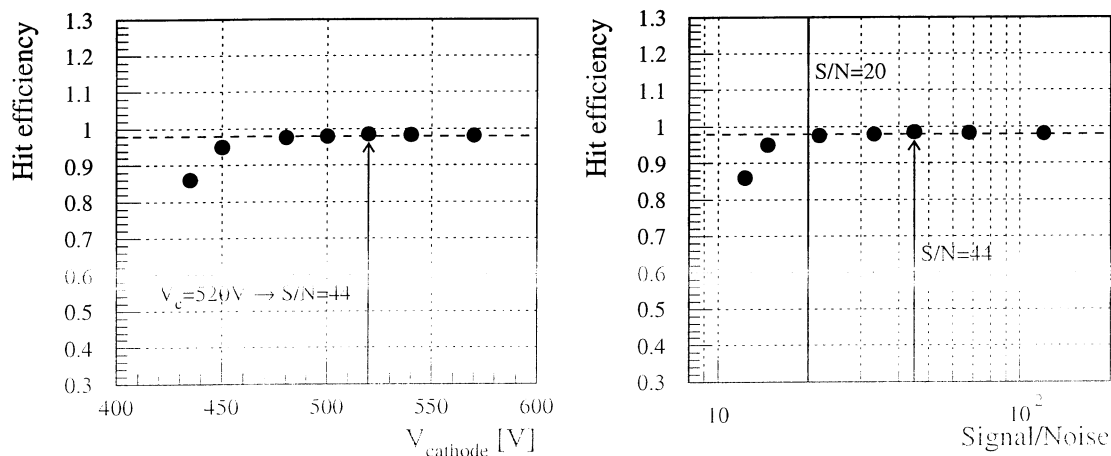


Figure 5.23: Hit efficiency for different operating points.  $V_{drift} = 3500$  V, Ne/DME=33/67 [32].

Tests in the laboratory have been performed with an  $Am^{241}$  5.5 MeV  $\alpha$ -source, showing that the threshold at which the frequency of sparking starts to increase dramatically is as high as  $V_{cathode} \sim 700$  V in a Ne/DME=33/67 mixture (Fig. 5.26).

It is of major interest to understand the robustness of the MSGC technology. In order to address this question of 'survivability' in a hostile radiation environment, tests in a beam providing such conditions were performed in Summer 1997 and continued in 1998 at the Paul Scherrer Institute (PSI) close to Zürich. At the  $\pi M1$  facility, a 350 MeV  $\pi^+$  beam with a proton contamination of a few percent and a flux of  $\sim 5$  kHz/mm<sup>2</sup> provided a radiation environment that was qualitatively and quantitatively comparable to LHC conditions [59]. Fig. 5.27 the noise of a chamber for all strips and the beam profile as measured by that chamber. Strips that are broken are clearly seen in the beam profile as they do not count any hits. For those strips the noise is also reduced: the capacitive noise (chapter A.2) does not contribute to the total noise of a channel, which is thus reduced by up to 30%.

The tests at PSI lasted for more than one month, and exposed the MSGCs to a dose of particles equivalent to  $\sim 14$  days of peak intensity at LHC, while operating at the nominal working point,  $S/N = 44$ . Comparing the noise pattern before and after the irradiation, no damage of the MSGCs could be observed (Fig. 5.27b). 10 years of operation at LHC are equivalent to  $5 \times 10^7$  s running at the peak LHC luminosity <sup>7</sup>.

<sup>7</sup>The first two years at LHC will feature a luminosity that is reduced by a factor 10. The average luminosity per day is a factor 2 lower than the nominal peak luminosity. LHC will operate  $3 \times 60$  days

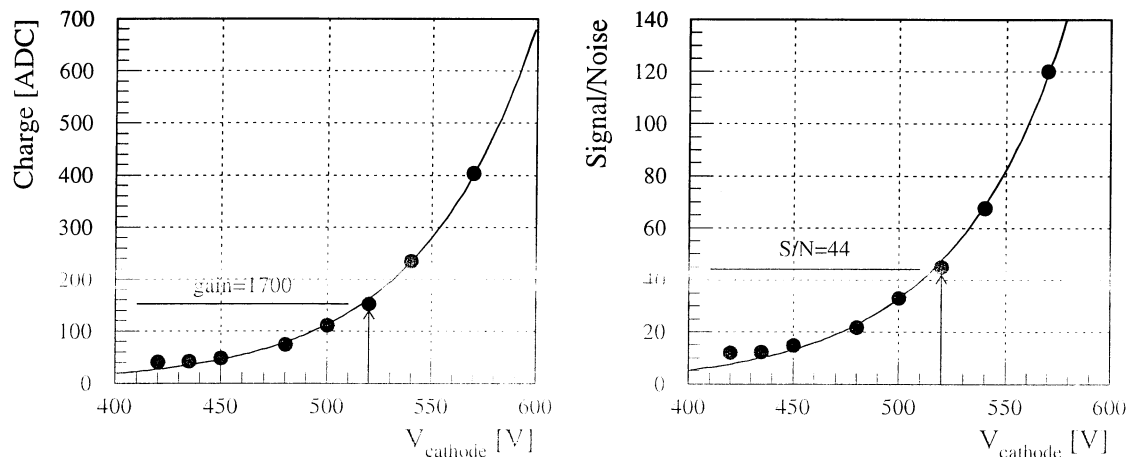


Figure 5.24: Signal/Noise ratio obtainable with CMS MSGC prototypes. Same operating conditions as in Fig. 5.23 [32].

Doing the brave extrapolation of the fact that less than one strip has been damaged in 14 days of operation, we can expect less than 40 defects per module within the full 10 years at LHC. This is less than 8% of the total number of strips. To get a more precise answer, a test with several tens of modules is planned for 1999. In order for CMS to operate up to expectations, the fraction of damages should not exceed 2%, as described in chapter 4.4.

Under the same conditions, a voltage scan was performed, to probe the regime of gain above the nominal working point (Fig. 5.28). The behaviour of the chamber was as expected and no damage of the micro pattern structure could be observed.

---

per year, 20 hours per day. Thus, the integrated luminosity equals  $\sim 5 \times 10^7$  s at peak luminosity.

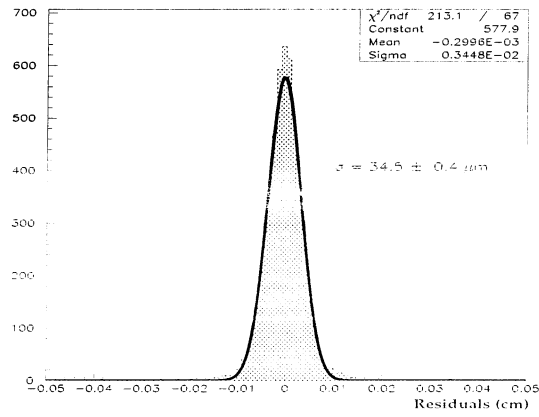


Figure 5.25: Spatial resolution of the MSGCs – deconvoluting the error of the track definition, the intrinsic resolution is  $\sim 30 \mu m$  [57].

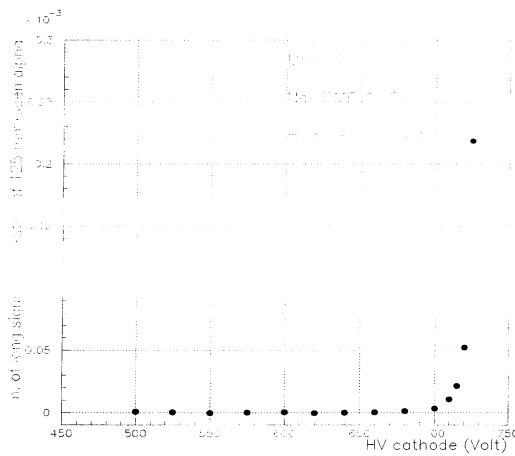


Figure 5.26: Onset of discharges at high voltages. Measurements were done with an  $Am^{241}$   $\alpha$ -source [58]. For cathode voltages higher than 700 V corresponding to gains well above  $10^4$ , discharges between anodes and cathodes can be induced.

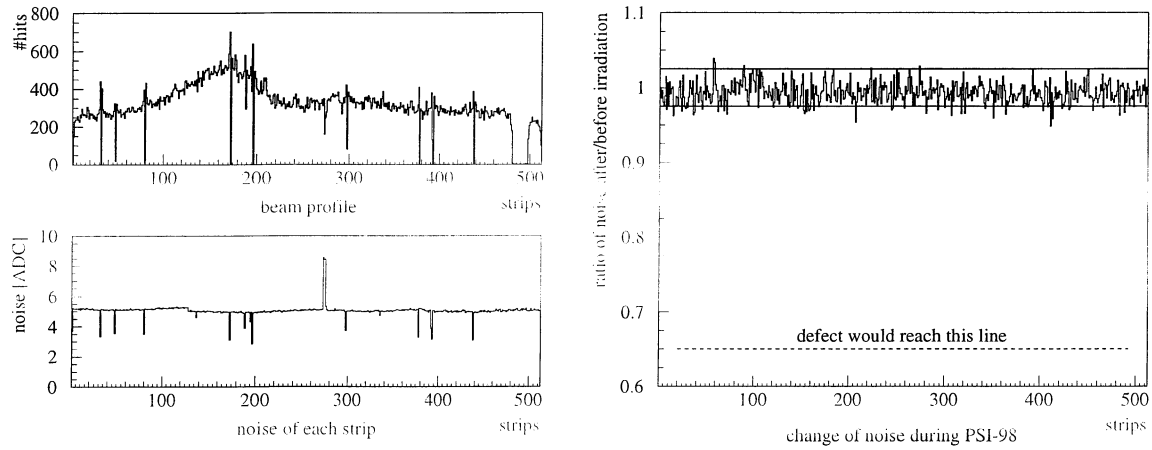


Figure 5.27: Beam profile of the 350 MeV  $\pi^+$  beam at PSI as measured by the MSGC and noise for each of the 512 channels (a). The ratio of noise (b) before and after irradiation shows no sign of deterioration of the MSGC.

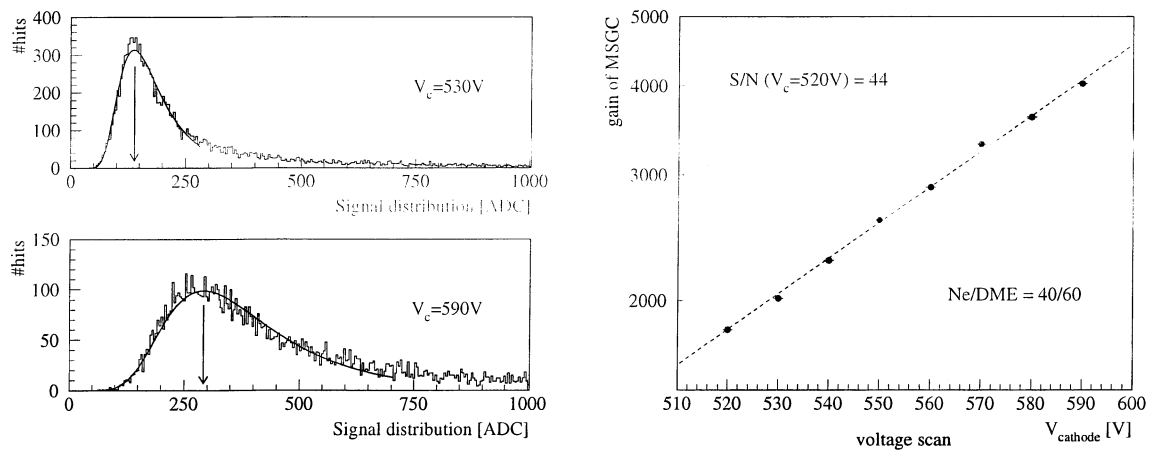


Figure 5.28: Voltage scan under LHC conditions. The MSGC functioned up to expectations and no strip damage was observed.



# Chapter 6

## Quality Control System

In the year 2000 mass production of the Microstrip Gas Chamber modules will start.  $\sim 10.000$  of them will be fitted into the CMS tracker, about half of those in the barrel region. Every single one of these modules has to undergo an extensive series of tests, scanning for faults, surveying the parameters that are important for the performance of the module in the CMS experiment and storing them in a database for later calibration and optimisation of the tracker.

Construction of the barrel part of the tracker will start in the year 2001. Thus, within one year, all 5540 MSGC modules and 736 rods have to be tested. Several laboratories including CERN will participate in this task and CERN will provide all the testing equipment. As one third of the modules and all rods will be inspected at CERN, our quality control system has to be capable of testing around 5 MSGC modules and two rods per day. The large number of modules requires a maximum of automation of the whole test chain, from data-taking to analysis and evaluation of the obtained results. This chapter presents the various setups that have been designed within the framework of this thesis.

Before assembly of the single module, the quality of the gold strips on the substrate is investigated by optical inspection and possible shorts between anodes and cathodes are detected electrically. Also, the resistivity of the substrate itself is measured. Then, substrate, frame and drift plane are glued together and the whole chamber is tested for leak tightness and mechanical precision of assembly. The electronic components - pre-amplifier chain and high voltage distribution - are tested and bonded to the chamber, completing the MSGC module. This module is then tested again with respect to

leakage current and shorts between anodes and cathodes, as well as the quality of the bonding.

At each of the MSGC test centres the modules have to undergo several further tests. Their task is to

- ) check whether each module can work at the nominal CMS working point,
- ) establish the various operational parameters of the single MSGC module,
- ) combine modules onto rods and test the integrity of this new subsystem,
- ) measure the mechanical alignment of the modules with respect to the rod.

The outcome of these tests do not only serve for assuring that all modules operate properly, but several parameters are entered into a database for later use when running the CMS experiment.

It is for example of primary interest for the track reconstruction algorithms to know which of the five million channels are working and what signal-to-noise ratio each strip-preamplifier combination features in order to assign the correct weight to each recorded hit. Also, global characteristics are important like the behaviour of each chamber in terms of gain as a function of high voltage to allow a fine tuning of the tracker for obtaining its maximum performance. Furthermore, the geometrical properties – the alignment of the modules and the knowledge of their exact position in the tracker – are crucial for excellent momentum resolution.

For these quality controls and chamber and rod characterisation three principal test stations are foreseen, whose design was part of the work for this thesis. They are described according to the chronological order in which an MSGC module is analysed with them.

1. **Cosmic telescope:** 5+5 freshly assembled modules are mounted into two racks, one module on top of the other, and sandwiched between two scintillators (Fig. 6.1). During  $\sim 2$  days cathode- and drift voltages are slowly ramped up for the first time in their life, while the current drawn by the cathodes and the drift plane are monitored, which determines whether each of the modules can properly operate at the nominal CMS working point. By triggering on cosmic rays and doing track finding, a first impression on their sensitivity can be gained.
2. **XY-table:** This test bench controls one module at a time (Fig. 6.9). A  $\text{Sr}^{90}$   $\beta$ -source moving in small steps irradiates the active surface of the MSGC, working at the nominal operating point. This allows to measure gain uniformity and position and number of misbehaving strip/preamplifier channels.

- Rod test stand:** A rod, fully equipped with already tested MSGCs is mounted onto a precision bench. A radioactive source similar to the one used by the XY-Table scans along the rod over the MSGC modules. The data taken allows to determine the relative alignment of the modules with respect to the rod, and also reveals whether electric connections are done properly. The gas leak tightness of the assembly is investigated as well.

## 6.1 Cosmics telescope

Once an MSGC is assembled and tested for gas leaks, its robustness to high voltage has to be established. As this is the first time when the high voltage applied to the micro pattern structure is ramped up to the nominal operating point, the task is a very delicate one, and will take around two days for each module.

When air enters the chamber during production or transport, a thin film of humidity might become deposited over the substrate, leading to a high leakage current of up to a few  $\mu A$  between anodes and cathodes. This will be attempted to be cured, but experience has shown that up to several days of flushing with nitrogen might be needed to 'dry' the chamber.

### 6.1.1 Description of the Cosmics Set-up

The testing of a single module will span a time of somewhat less than two days, as described in the next section. Needing a through-put of five chambers per day, this implies that the test stand has to be capable of testing 10 modules simultaneously. This goal is achieved by having two racks with five chambers each operating in parallel. One 'rack' is depicted in Fig. 6.1. Between two scintillators, five MSGCs operate in parallel, with independent gas and high voltage settings. By monitoring cathode- and drift current and detecting current spikes, several 'features' of the MSGC modules can be tested: A constant high leakage current can reveal moisture in the chamber which can be cured by letting the chamber dry under nitrogen for some more time. Up to three days flushing at a rate of 5 l/h might be required. Triggering on the cosmic rays allows to get a first picture of the dependence of the chamber gain on the voltage settings while approaching and surpassing the nominal operating point. Insufficiently robust chambers, that is chambers that tend to spark spontaneously or where sparks

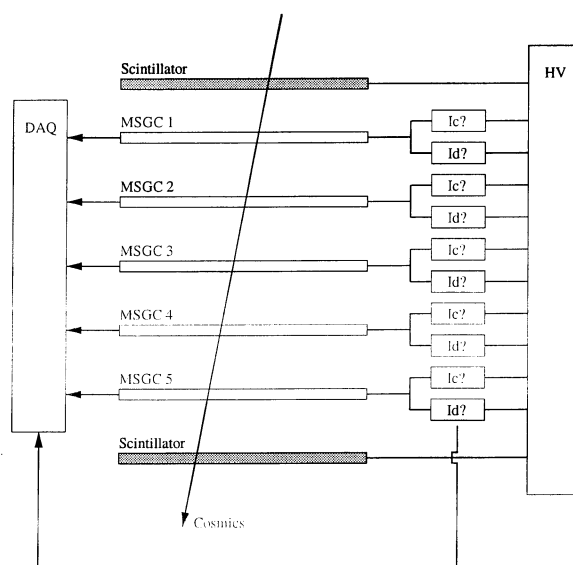


Figure 6.1: Schematic view of the cosmic rack: Five MSGCs are sandwiched between scintillators. Cathode- and drift current are monitored while exposing the chambers to cosmic rays.

can be induced by the charge liberated by cosmic rays, can be identified.

The **gas mixing system** designed for the cosmic rack is shown in Fig. 6.2. Its purpose is to provide nitrogen, the neon-DME mixture, and eventually a radioactive gas mixture to a number of 'cosmic racks'. Three main valves and five flow meters, all electronically controlled, ensure a constant supply of all the gas mixtures needed for the cosmic racks. Three over-pressure valves (see chapter A.4), calibrated for 30 *mbar*, can absorb sudden pressure fluctuations when opening a valve or changing the gas flow or composition.

The whole system can be computer controlled, including logging of all operations and parameter changes, as well as raising warnings and alarms and halting the system in case parameters like pressure or gas composition exceed their nominal values by specifiable thresholds.

Also, each **cosmic rack** has an electronically controlled gas distribution system (Fig. 6.3). Electronic valves at the chamber input allow to choose one out of the three gases independently for each module.

To prevent over-pressure, over-pressure valves calibrated for 3 *mbar* are put in parallel with the chambers, one over-pressure valve for each gas line. A flow meter

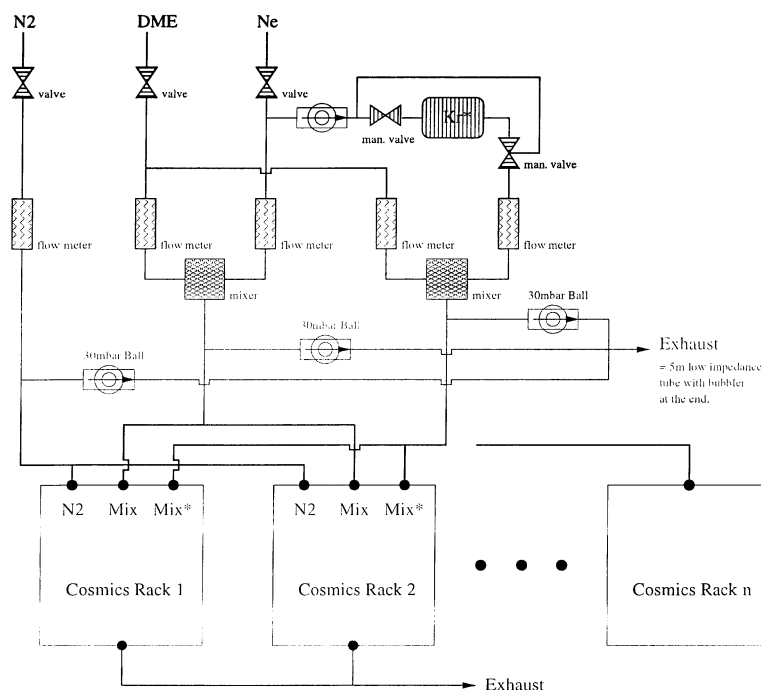


Figure 6.2: The gas mixing system for the cosmic racks.

in series with them measures whether they are open, and can thus give feedback on the operation of the gas system to the computer control. This feedback serves a triple purpose:

1. **Detection of pressure build-up in the chambers.**

By having an exact pressure release point of the over-pressure valves and measuring the flow passing through them, the main gas system can readily be instructed by how much to reduce the gas flow in order to maintain low pressure in all chambers.

2. **Control of the functioning of the electronic valves.**

When a valve at a chamber input is opened, i.e., when another chamber is linked to a gas supply line, e.g. nitrogen, the flow for this gas is automatically increased by 3 l/h by the main gas supply system, in order to guarantee a constant amount of gas flow in all chambers. If the electronic valve would show a failure, and remain closed, the thereby created over-pressure would be sensed by the flow meter and an alarm would be issued.

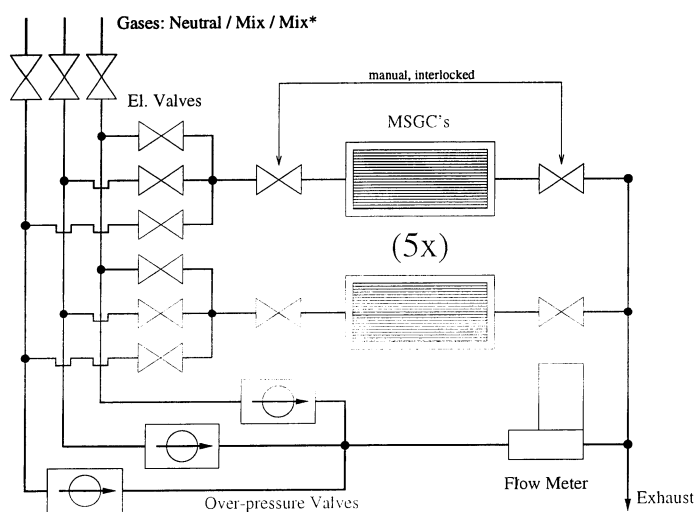


Figure 6.3: Automatic gas distribution system of the cosmic rack. Every MSGC can be operated independently.

### 3. Measurement of the gas impedance of each MSGC.

By temporarily closing all valves at the chamber inputs of the cosmic rack except one, and instructing the main gas supply system to slowly increase the flow until a over-pressure valve opens, the exact flow that generates 3 *mbar* of over-pressure in the chamber can be determined, which can be used to e.g. detect, whether gas connections are not made properly or whether a chamber leaks or, inversely, features a too high gas impedance due to a mechanical defect.

## 6.1.2 The testing procedure

The test procedure can be broken down into into several phases.

1. Flushing the chamber gas volume with nitrogen to remove possible humidity and solvents that remained from the industrial production.
2. Slowly ramping up cathode- and drift voltage to the nominal working point ( $V_c = 520\text{ V}$ ,  $V_d = 3500\text{ V}$ ) while monitoring the corresponding currents.
3. Staying at this operating point and monitoring eventual current spikes.
4. Increasing the voltages by 20 % for probing the safety margin.

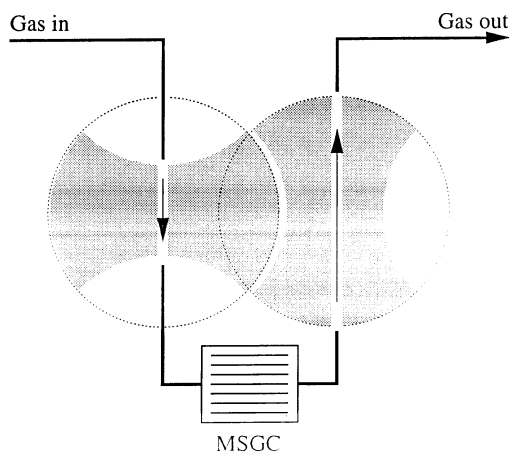


Figure 6.4: Mechanical gas interlock between gas in- and output of the MSGC. The two manual valves at the input and output of each MSGC open or close when rotated by  $90^\circ$ . Their handles are shaped in a way that the output can only be closed once the input is closed, and that the input can only be opened *after* the output, avoiding damage to the chambers resulting from miss-manipulation.

5. Changing the gas to the nominal Ne/DME=40/60 mixture and repeating steps 2, 3 and 4.
6. Steps 2 and 3 can be repeated with a radioactive ( $\gamma$ -emitting) gas, described below.

A graphical representation of this test procedure that spans 42 hours in case of flawless operation of the chamber module, is depicted in Fig. 6.5.

In order to perform the current measurements on the  $5 \times 2$  high voltage channels of each cosmic rack and to detect current spikes, a pico-amperometer has been developed<sup>1</sup> which can measure currents down to  $\sim 100$  pA at voltages of up to 7 kV, largely sufficient for MSGCs. Thus, even smallest precursors to strip or drift plane discharges can be registered. During the moments where the voltages are increased, small discharges (i.e. discharges of less than a full strip) can be tolerated, whereas the five hours of continuous operation each at the nominal working point and 20% above must not

<sup>1</sup>Marcos Gaspar, private communication and <http://home.cern.ch/~gasparm>

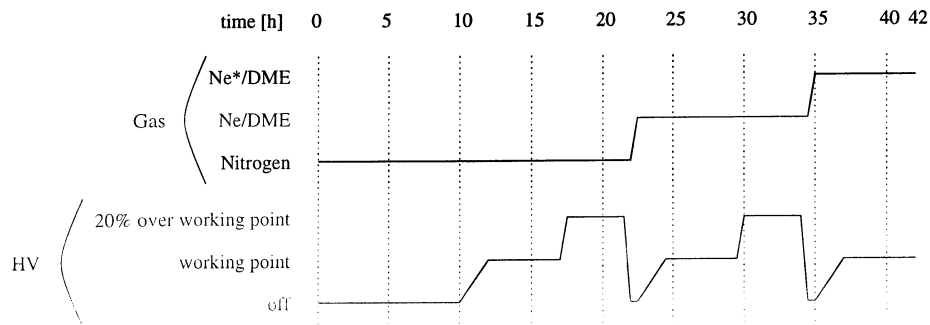


Figure 6.5: Cosmics test stand, graphical protocol: While monitoring the chamber currents, the HV-operating point is probed for various gases. Gas and high voltage settings as well as the current monitoring are computer controlled.

reveal any instabilities.

When running with Ne/DME as opposed to nitrogen, the chamber is sensitive to particles, especially heavily ionising fragments created by hadronic showers originating from interactions of energetic cosmic rays in the material surrounding the Cosmic Rack. The created huge signal might mimic a spontaneous discharge of a strip similar to Fig. 5.8. These processes though are very rare and we will tolerate one non-destructive discharge while operating the chambers with Ne/DME. For every chamber a 'spark profile' is determined, i.e. a three dimensional histogram showing the discharge size and frequency as a function of the high voltage.

### 6.1.3 Radioactive Gas

A novel way for testing the integrity of the strips of an MSGC module and finding its gain is under investigation. Radioactive gas can be flushed through the chambers. The decaying isotopes generate signals in the chamber that can be read out. This gives

- ) a rough picture of the gain uniformity of the chamber
- ) indicate the position of non-functioning strips.

The absolute gain of the chamber cannot be determined, as the results depend strongly on the amount of radioactivity within the gas. It was foreseen a part of this thesis to implement such a system on the Cosmics Rack, but due to unforeseen technical problems of the Isolde complex, no time for the production of an adequate source was found yet.



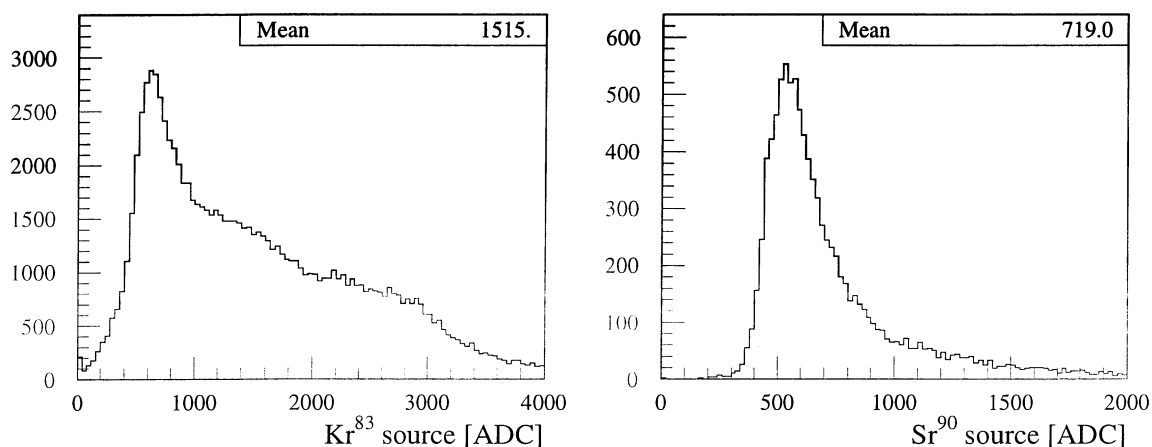


Figure 6.6: Energy loss spectrum of  $\text{Kr}^{83}$  (a) and  $\text{Sr}^{90}$  (b) measured by an MSGC. The signal obtained with the Krypton source was attenuated by 9 dB before being fed into the ADC, thus an average signal comparable to (b) would be a factor 2.8 higher.

The source is used in the following way: It is placed into the gas system and consists of a mylar foil with embedded  $\text{Rb}_{37}^{83}$  atoms. These decay into  $\text{Kr}_{36}^{83}$  with a decay time of 86.2 days and are taken away by the gas and transported into the MSGCs. The metastable  $\text{Kr}_{36}^{83}$  itself decays with a half life of 1.8 hours thereby releasing a 32 keV and a 9 keV photon within a time window of 150 ns.

We have performed tests with a  $\text{Kr}^{83}$  source on the chamber presented in chapter 5.5 and compared it to the  $\text{Sr}^{90}$  source used for the XY-Table. Fig. 6.6a and b show the energy loss spectrum as recorded by the MSGC.

It has to be noted that with the used chamber it was possible to synchronise the read-out of the chamber with the Krypton decays, similarly to the setup described in Fig. 5.16. This will not be possible when using the final APV electronics, which can only be triggered with an external clock which in the final CMS detector will be synchronised with the LHC bunch crossing frequency. In order to see whether it is feasible to use radioactive gas also in that case, it has to be calculated how many disintegrations we would need per second in order to get an average signal-to-noise ratio of, say, 5, which is high enough to distinguish a good strip from a broken one. Thus we ask for a measured average signal of  $\sim 25$  ADC values.

- ) The APV electronics is very similar to the PreMux electronics used to date (see chapter 5.3.2), and all measurements done with the PreMux electronics will be valid for the APV read-out. For the former we know, that the  $\text{Sr}^{90}$  peak is at  $\sim 80$  ADC

counts for one strip. Thus, deducing from Fig. 6.6 the average  $\text{Kr}^{83}$  signal would be a factor 6 higher, around 480 *ADC* counts.

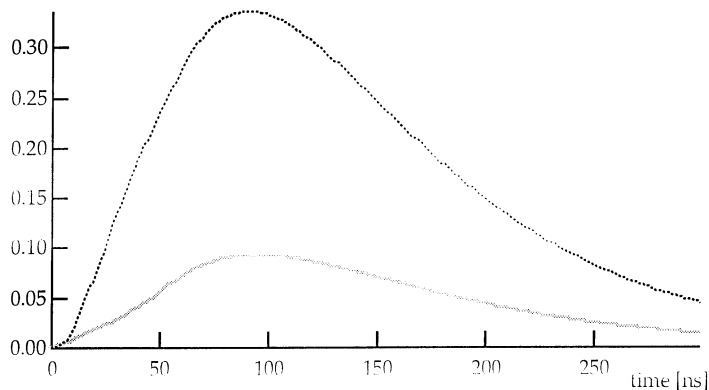


Figure 6.7: Simulated signal after pre-amplification and shaping [51]. The lower curve represents a signal produced by an avalanche with  $\sim 40,000$  electrons, which is created by a MIP under nominal operating conditions, the higher curve corresponds to four times more input charge. An average signal produced by the photons from the  $\text{Kr}^{83}$  source would be a factor six higher than the signal produced by a MIP (see the text).

- ) The electrons of the  $\text{Sr}^{90}$  source deposit a similar amount of energy in the chamber as a MIP, which can be seen by comparing Fig. 5.28 and Fig. 6.12. In the first case, the landau curve peaks at  $\sim 150$  *ADC* counts, in the latter it is 80 *ADC* counts for a single strip, corresponding to 120 *ADC* counts for the full avalanche distributed on more than one strip. Simulations (Fig. 6.8) confirm that result. Thus, the energy deposited by the Krypton source is about six times higher than that deposited by a MIP.
- ) The shape of the signal that is fed into the sampling circuits of the PreMux and the APV after pre-amplification and shaping is shown in Fig. 6.7. An average shaped and pre-amplified signal from the Krypton source would be  $\sim 1.5$  times higher than the upper curve in that plot, with a peak corresponding to  $\sim 480$  *ADC* counts. Thus, sampling this signal randomly once within every 500 *ns* after its creation by an avalanche process, we would measure an average of  $\sim 200$  *ADC* counts, or around 25 when sampling within 4  $\mu\text{s}$ <sup>2</sup>. The latter corresponds to randomly reading out the chambers with a continuous activity of the radioactive gas of 250 *kBq* per strip, or 128 *MBq* per

<sup>2</sup>We scale down 'by eye', simply continuing the signal to longer times by setting it to zero for times bigger than 500 *ns*.

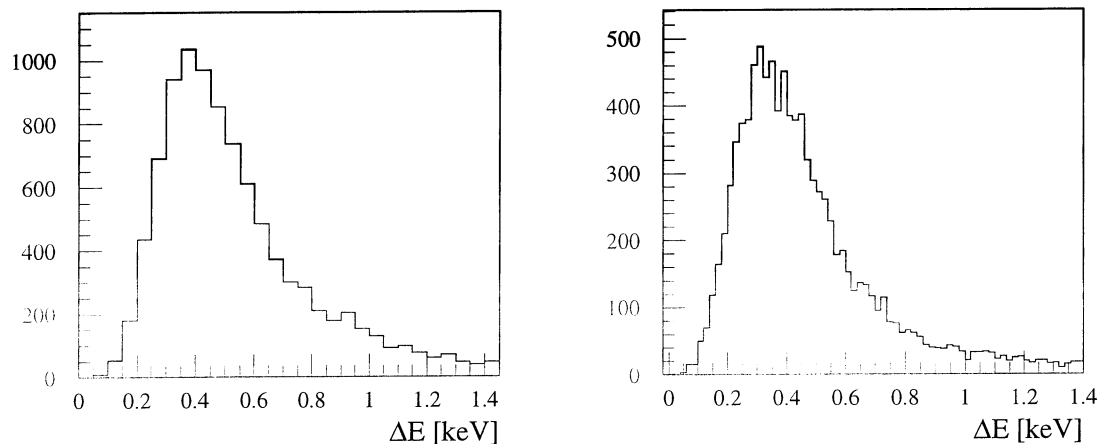


Figure 6.8: Energy deposited by a MIP ( $350 \text{ MeV } \pi^+$ ) (a) and  $2.2 \text{ MeV } e^-$  from the  $\text{Sr}^{90}$  source (b) in  $3 \text{ mm}$  of NE/DME=40/60 gas mixture. Simulations were done using Garfield [16]

chamber (512 strips). The Cosmics Rack will operate up to 10 chambers in parallel, thus requiring a 10 times higher activity of the gas.

The gas is enriched with  $\text{Kr}^{83}$  in a small steel cell that measures  $10 \text{ cm}$  in length and  $5 \text{ cm}$  in diameter. Thus, with a gas flow of  $10 \text{ l/h} \approx 3 \text{ cm}^3/\text{s}$ , each unit volume of gas takes  $\sim 1 \text{ min}$  to traverse the source, accumulating 60 times the activity of the Krypton of the source. It's way from there to the chambers might take  $\sim 10 \text{ min}$ , during which about 10% of the Krypton decay.

Thus, a radioactive source of  $\sim 20 \text{ MBq}$  should be adequate for our purposes. Taking into consideration a half life of the source of less than three months, it should be substantially stronger. Consequently, we have submitted the wish for a  $100 \text{ MBq}$   $\text{Rb}^{83}$  source to Isolde and should obtain it still in the first half of this year.

## 6.2 XY-Table

The next and most important step in the quality control of the MSGCs is to establish the response of the detectors to ionising particles. This means determining the gain of the chamber, measuring the noise to obtain the signal-to-noise ratio and thus ultimately knowing the detection efficiency (Fig. 5.23), which is crucial for the performance of the whole tracker.

The XY-Table can determine the performance of each single strip, in terms of integrity, i.e. "is the strip functional along its entire length?", noise of the strip and the corresponding pre-amplifier and gain, thus yielding a gain uniformity curve of the chamber.

### 6.2.1 Description of the XY-Table

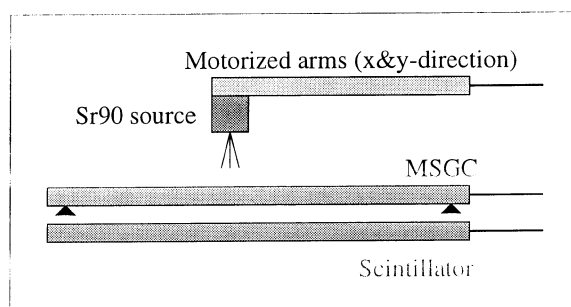


Figure 6.9: XY-table – principle of operation: A  $Sr^{90}$ -source is moved across the active surface of the MSGC. Triggering on electrons traversing the chamber with a scintillator, the anode strips are read out.

The gain uniformity measurement of an MSGC is performed by scanning a  $Sr^{90}$ -source over the active surface of the MSGC and recording the response of the single strips.

Several components have been developed and assembled (Fig. 6.10):

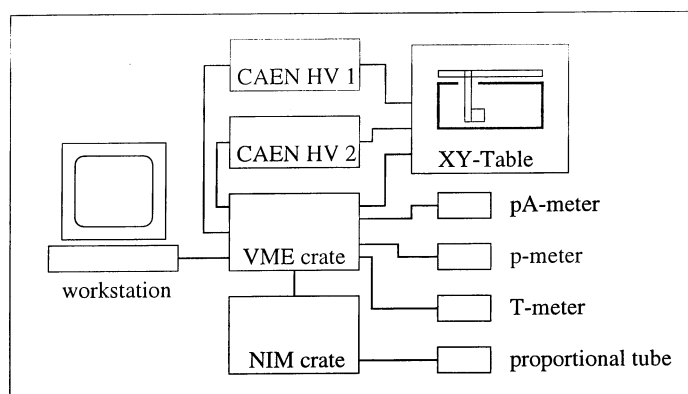


Figure 6.10: Schematic layout of the XY-table test system.

1. An aluminium tray holds the support for an MSGC module and two motorised arms that move the  $3.7 \text{ MBq Sr}^{90}$ -source over the module (Fig. 6.9). It also houses a  $10 \times 25 \text{ cm}^2$  scintillator and photomultiplier for triggering as well as the circuit containing the trigger electronics. With a background rate of  $\sim 1 \text{ Hz}$ , a single scintillator proved to be sufficient for triggering and no coincidence was needed. Despite of a thickness of only  $5 \text{ mm}$ , the uniformity of the response of the scintillator is  $\sim 1\%$ .
2. The read-out of the chamber electronics (Premux to date) is done with a Sirocco and a sequencer (CAEN) and a FIC (CES). This electronics has already been described in chapter 5.3.
3. Two gas mixing systems have been built. A rather simple one using three HITEC flow meters was used for all the measurements taken in this thesis, while a parallel system featuring pressure sensors and gas purity controls is currently being adapted for use with the XY-table.
4. After being used in the MSGC, the gas is fed through proportional counter in order to provide a way of monitoring the gas quality and allow for eventual renormalisation of the MSGC gain due to pressure or temperature fluctuations.
5. Sensors are monitored periodically to log atmospheric pressure and temperature.
6. Two high voltage supplies (CAEN SY127 and CAEN SY694) provide the voltages  $V_{\text{cathode}}$  and  $V_{\text{drift}}$  for the MSGC as well as high tension for the proportional tube and the scintillator.
7. Drift- and cathode current are monitored with the same devices as used for the cosmics setup described above.

The electronics (with the exception of the HV supplies) is housed in a VME and a NIM carte. Via Ethernet the FIC in the VME crate is connected to a SUN workstation with a  $9 \text{ GB}$  hard disk for temporarily storing the data and analysing it.

Fig. 6.11 shows a picture of the test stand and the user interface.

The whole test sequence is fully automated. With the push of a button the high voltages are ramped up and a chamber scan is performed. One scan takes up to one hour. This time depends on the desired precision of the test, i.e. the amount of data to be taken and on the read-out electronics. To date, the final electronics, which will require a different read-out scheme, is not yet ready, and thus no effort has been taken

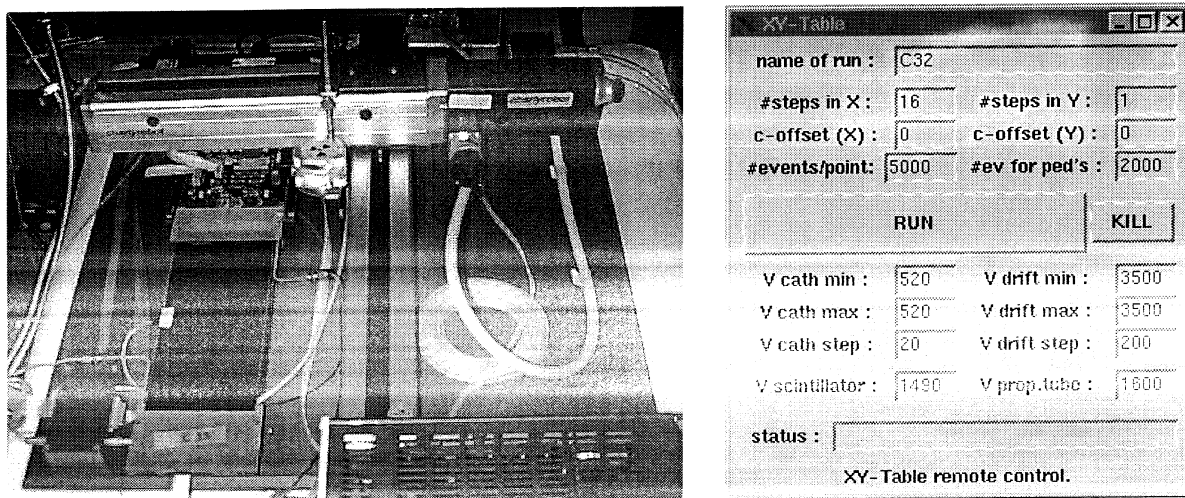


Figure 6.11: The XY-Table with a  $10 \times 25 \text{ cm}^2$  module under test and a screen shot of the user interface.

to maximise the speed of the data acquisition. The event rate is limited to  $\sim 100 \text{ Hz}$ , which can easily be increased by an order of magnitude with the APV electronics, and the main bottleneck, the slow Ethernet connection used for transferring the data to the analysis station, can be trivially overcome by using a dedicated cable. Once data acquisition has finished the analysis program is launched, which produces a graphical output, and the operator is informed via e-mail or his portable phone that the XY-table is ready to test the next MSGC or that the current module has not passed the test criteria which are described in the following section.

### 6.2.2 The testing procedure

The XY-table test station addresses several questions concerning the proper functioning of the MSGC modules. There are mechanical issues, like the quality of the bonding of all the 512 strips to the read-out electronics, the integrity of the strips along their entire length, electronics related issues like the noise of each channel and features concerning the charge amplification in the gas, like the uniformity of the gain across the active volume of the chamber. The noise of each strip/pre-amplifier combination can also be determined with a fully equipped cosmics test stand. But as there will be several test centres, some might opt for a less sophisticated cosmics test stand in order not to over-strain their financial budget. This option would refrain from reading out all the

$\sim 10$  MSGCs on the cosmics telescope(s), but only measure chamber currents. In that case the XY-table would be the main tool to determine the strip and electronics noise.

The test of a chamber is divided into several steps, of which only the first two require manual intervention. Apart from the installation of a chamber onto the XY-table, the whole sequence is computer controlled.

1. Put MSGC module onto XY-table, connect gas, high voltage- and read-out cables.
2. 15 minutes of purging the chamber with  $N_2$ /DME.  
The gas volume in the chamber is exchanged 30 times, at a flow of 3 l/h.
3. All strips are pulsed at three different distances to the electronics to check the electronics for uniform behaviour and the integrity of the strips and their connection to the electronics (see chapter 6.4). This takes a few minutes.
4. The chambers are assumed to be tested with the cosmics setup (chapter 6.1) and proven to reliably stand high voltage, thus cathode- and drift voltages are ramped up to the operating point in a single step, with  $\Delta V_{cathode} = 20$  V/s and  $\Delta V_{drift} = 200$  V/s.
5. Data is taken with a proportional tube that is connected to the gas system in series with the MSGC module to monitor the gas composition and to give reference values for the gas amplification.
6. The  $Si^{90}$  source is scanned over the chamber, in one of the modes described in the next section. Temperature and atmospheric pressure are logged, and fluctuations in cathode- and drift current are monitored.
7. Once the scan with the radioactive source has finished, the gas is tested again with the proportional tube to ensure that all strips of the MSGC module were tested under the same conditions.
8. Cathode- and drift voltages are ramped down again and the collected data is analysed offline.

A scan across the strips is performed in steps of 30-50 strips (6 – 10 mm). At each position the radioactive source illuminates an area – around 80 strips wide – with a Gaussian intensity distribution. 5000 to 10000 events are recorded at each position.

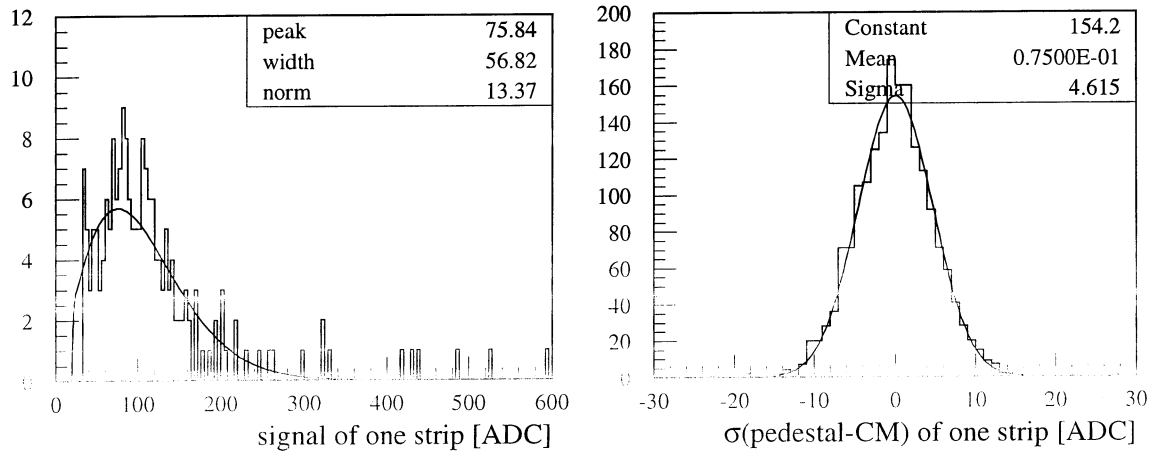


Figure 6.12: Signal and noise of a single strip as measured by the XY-table. (a) shows the quasi-landau  $E_{loss}$  distribution of the electrons from the  $\text{Sr}^{90}$  source in ADC counts, (b) shows the noise of a strip, i.e. the ADC distribution when reading out a strip without irradiating.

A typical test of an MSGC would consist in scanning the radioactive source across the 512 strips, at one given distance from the electronics. This gives all the important information that is necessary to classify a chamber as being usable in CMS. Nevertheless, several further testing schemes can be applied, in case the 'standard' scan has revealed imperfections.

A scan along the strips can be performed, either in combination with a scan across the strips, in order to give a fully two-dimensional picture of the gain of the chamber as a function of the position in the active volume, or at fixed X-position, i.e., along a given strip. The latter testing method can be used for determining the attenuation of the signal along the strips. Although this is not a main issue when using gold strips, it can be performed periodically to ensure a constant quality of the substrate production and pattern etching technique of the manufacturer.

It is also possible to irradiate the MSGC at a single point. This can be used in case critical regions of a chamber are to be investigated, e.g. the edges, or when the exact position of the defect in a broken strip has to be determined.

Separately, or in combination with any of the above scanning schemes, a high voltage scan can be performed. The results of such an investigation are analysed automatically, too, and can verify whether the gain of a chamber exhibits the expected exponential behaviour with changing cathode voltage or whether unexpected phenomena occur.



The difficult working environment at LHC and the necessity for excellent physics performance of the CMS tracker put stringent quality requirements on each MSGC module. In order to guarantee good momentum resolution, not more than 10 channels out of 512, i.e., less than 2 %, must be defect. This number includes broken strips and bonding errors as well as noisy electronics channels. A strip broken in the middle counts as half a broken strip, and 'noisy' means that a channel exhibits at least three times the noise of an average channel.

The uniformity of the gain is more difficult to quantify, and thresholds can only be set once several tens of modules have been tested and a rough picture of the quality distribution of the manufactured modules has been obtained. To date only one chamber with non-uniformity has been found (see Fig. 6.16 and compare to Fig. 6.13), and there the poor performance was obvious at a first glance.

### 6.2.3 Results of a test

The XY-table gives information on most of the properties of a chamber that are also determined in a test beam, like average Landau distribution of the energy loss of particles in the chamber, noise of each strip and thus signal-to-noise ratio of the MSGC, and the current drawn by the cathodes and drift plane during operation. These parameters are illustrated in Fig. 6.13-Fig. 6.14.

In Fig. 6.12a the signal distribution of one single strip-preamplifier channel is shown. Plotting the peak of this distribution versus the strip number for all strips, we obtain a characterisation of the gain uniformity of the whole chamber as seen in Fig. 6.13 In this plot the average signal is around 80 *ADC* counts. Dividing this number by the average noise per strip,  $\sim 5$  *ADC* counts, does not give a value comparable to the  $S/N = 44$ , typical for the chambers at that working point. Several factors have to be taken into account:

- ) The gain of the gas mixture used in that chamber,  $Ne/DME = 1/2$ , is 30% lower than for the  $Ne/DME = 2/3$  chosen for CMS.
- ) The average cluster size is around 2.2 strips, a typical signal looking like Fig. 5.12. Thus, one strip only sees about 60 – 70% of the whole deposited charge.
- ) Finally, cross-talk (chapter 5.4) has not been corrected for, which would give an up to 10% increase in signal.

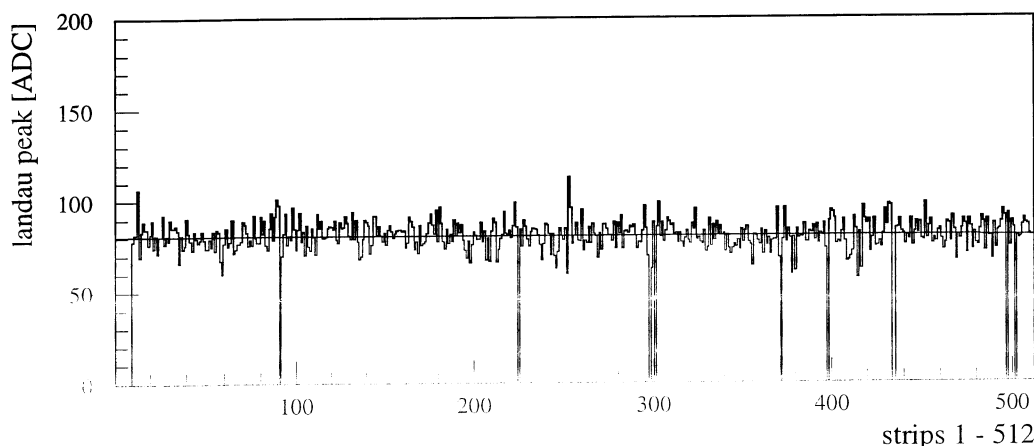


Figure 6.13: Gain uniformity of an MSGC. The most probable ADC value versus strip number of each strip is shown. Typical strip to strip fluctuations are  $\sim 10\%$  in this measurement, partly due to the statistical size of the data set, which will improve significantly with the faster read-out chain designed for the final electronics.

### What defines a 'good' module for CMS ?

The CMS tracker has to fulfil stringent requirements in order to fully exploit the physics potential that the LHC will offer (chapter 5.6). These translate for the MSGCs in a high signal-to-noise ratio in order to obtain the necessary hit efficiency (Fig. 5.23) and a small fraction of malfunctioning strips to not to decrease the spatial resolution of the chamber.

Quantitatively, these requirements can be summarised in few points:

#### 1. Overall gain (HV-scan) :

The gain at the nominal working point ( $V_c = 520 V$ ,  $V_d = 3500 V$ ) must be such, that a signal-to-noise ratio of at least 20 with the final APV electronics results. This requires an average strip response of  $\sim 80 ADC$  counts.

Within statistical accuracy there must not be a noticeable deviation from an exponential dependence of the gain on the cathode voltage, over a range  $440 V < V_c < 600 V$ .

#### 2. Gain/strip $\rightarrow$ uniformity :

Strip-to-strip variations in amplification have values typically below 15%, including the statistical measurement errors of the XY-Table. Thus, a global variation

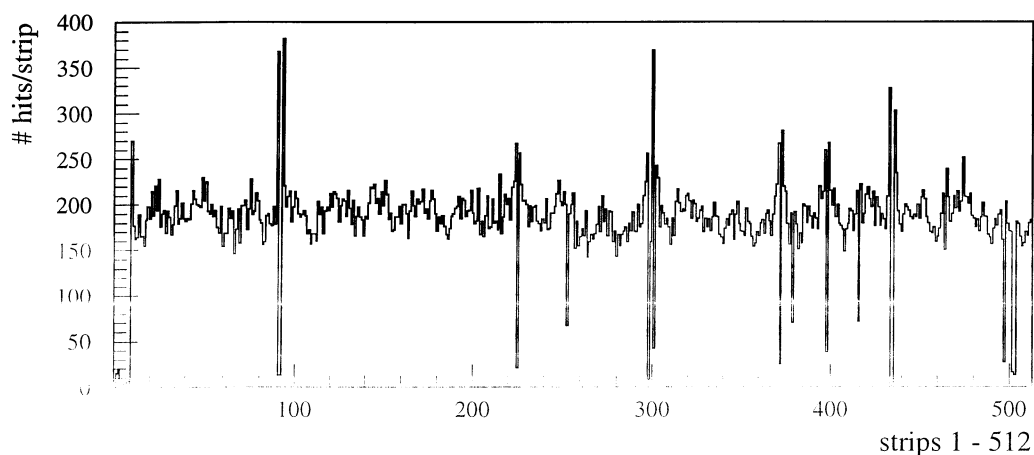


Figure 6.14: Number of particle hits per strip. The periodic non-uniformity of the irradiation intensity reveals the 20 different  $\text{Sr}^{90}$ -source positions during the scan. The effect of an increased counting rate on some strips is explained in Fig. 6.18.

in gain – an obvious case is depicted in Fig. 6.16 – also should not exceed this value.

### 3. Noise of chamber :

The average noise per strip must not exceed 5.5 *ADC* counts and the number of base-line jumps (chapter 5.4) must not exceed 2% of the total number of recorded events.<sup>3</sup>

### 4. Noise → fraction of broken channels :

The sum of broken and noisy channels must not exceed 2%, where we define a channel as noisy, when its noise is more than 20% than the average chamber noise. A strip is marked as (partially) broken, when its noise lies below 90% of the average chamber noise *or* when the number of hits it registers is low (see next point).

It has to be noted, though, that a broken channel does *not* necessarily reduce the hit efficiency of the chamber. When an anode breaks, the electrical field lines change direction in such a way (Fig. 6.17), that all the charge is still collected on the neighbouring strips and thus, the traversing particle is still detected (see Fig. 6.18). Nevertheless, the resolution of the chamber around that strip is reduced, and thus the position of the broken strip should be known in order to assign a lower weight to the hit when performing the track reconstruction.

<sup>3</sup>It remains to be seen whether the latter is an issue with the APV electronics.

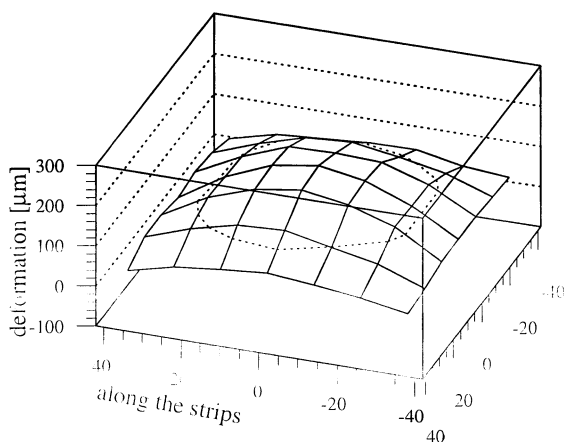


Figure 6.15: Mechanically deformed module. One case of a module was found where the drift plane showed a 'balloon-like' inflation with a maximum deformation at the centre of the chamber of over  $200 \mu\text{m}$ . This can be due to an improper gluing of the drift plane or a damage through excessive pressure differences during transport.

#### 5. Number of hits/strip $\rightarrow$ efficiency :

A look at Fig. 6.14 shows that inefficient strips are easily detected by looking at the number of hits the strip recorded during a scan. Comparison with Fig. 6.13 shows that a strip can be defined as 'dead', when it records less than 30% of the number of hits of an average strip.

If this number lies between 30 and 65%, the strip is marked as being only partly efficient (which counts as 1/2 broken strip).

#### 6. Currents under irradiation :

The radiation flux of the  $\text{Sr}^{90}$  source,  $3.7 \text{ MBq}$ , is too low to significantly alter the cathode current drawn by the chamber under irradiation. Nevertheless, cathode- and drift current are monitored to detect spontaneous or cosmic rays induced discharges between strips. Sparking chambers should not be encountered, as they are singled out with a prior test using the cosmic telescope.

Based on the outcome of each test, the MSGCs will be accepted and mounted into the tracker structure, or rejected. In the latter case the test can help in deciding how to improve the chamber performance, if possible.

For each module, the characteristics as described above are automatically stored in a CMS-wide database [60], for calibration and event reconstruction algorithms.

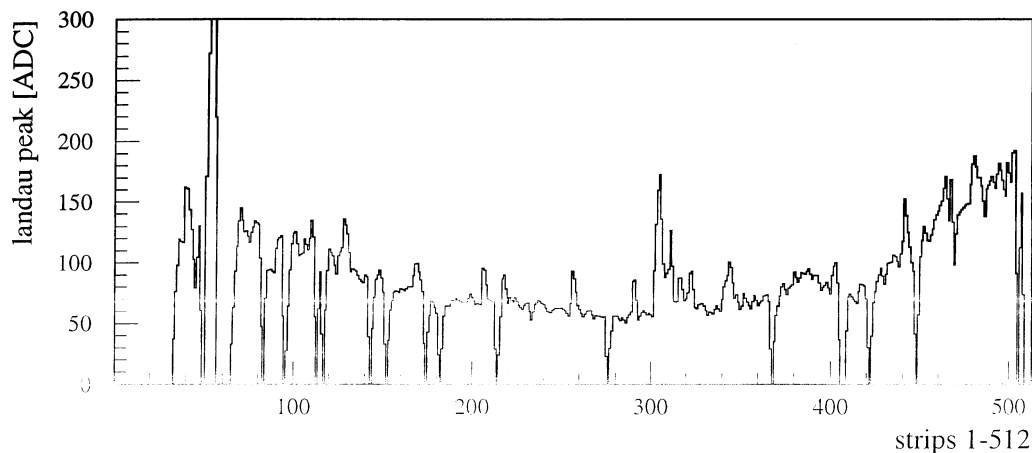


Figure 6.10: Gain non-uniformity of a mechanically deformed module.

Furthermore, comparing MSGC characteristics like gain and gain-versus-voltage behaviour obtained from the XY-Table, it is possible to group similar modules onto one rod (see below) in order to obtain the most homogeneous performance of the tracker.

### 6.3 Rod Test Stand

A rod is a carbon-fibre structure (Fig. 4.3) that contains five or nine<sup>4</sup> MSGC modules supplying them with low- and high voltage and gas. It also carries the cooling pipes. All the necessary connectors, including the read-out cables, are interfaced from one side of the rod. The Rod Test Stand must make sure that all these connections are done properly<sup>5</sup>.

The barrel part of the MSGC tracker will consist of 736 rods, which are supported by carbon fibre disks. A laser alignment system is planned to give the position of each rod within the tracker. In order to know the position of each single MSGC module, its position with respect to the rod has to be known. This is another task the Rod Test Stand has to perform.

<sup>4</sup>One 12.5 cm long module and four single or double sided 25 cm long modules in the case of one-dimensional or small angle stereo read-out, respectively.

<sup>5</sup>As a final version of a rod equipped with MSGCs and the APV electronics will only be available in 2000, this test stand has been designed but is not operating yet.

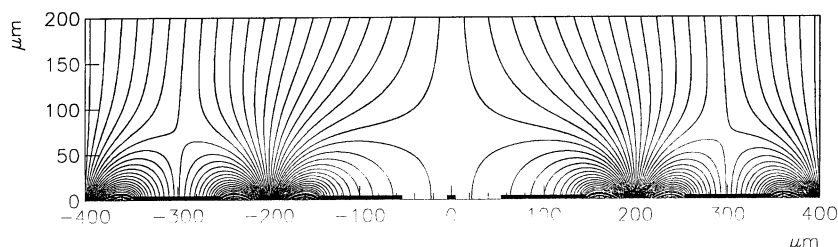


Figure 6.17: Field configuration with a floating strip – still, all field lines end on anodes and hit efficiency is not greatly influenced

### 6.3.1 Description of the Rod Test Stand

The Rod Test Stand is conceptually very similar to the XY-Table. Fixed to a base plate a 1.50 m long arm that can move a radioactive source over the rod which is mounted on a precision support. This support defines the exact position of the rod with respect to the base plate. The measurements the Rod Test Stand has to perform are done as follows:

#### Leak tightness of gas connections and impedance of the rod.

The determination of the gas impedance of the rod is not only important as a check whether the gas connections are done properly, but serves for combining well matched rods when constructing the tracker, where always ten rods will be fed in parallel by a single gas line.

Fig. 6.19 shows the schematic layout of the gas handling circuit. A constant gas flow of  $\sim 3$  l/h is applied to the gas input of the rod. This builds up a certain pressure of a few mbar which can be measured, giving a means to establish the impedance of the rod. The measurement is repeated with different amounts of gas flow. The pressure meter is separated from the gas by a thin membrane of stainless steel with a diameter of  $\sim 20$  cm, as its own membrane must not get in contact with the aggressive DME. The error introduced can be corrected for.

In order to measure the leak tightness of the rod, a pressure of a few mbar is built up in the rod, using two valves at the gas in- and output (Fig. 6.19). The chambers are protected against excessive over-pressure by an over-pressure valve connected in

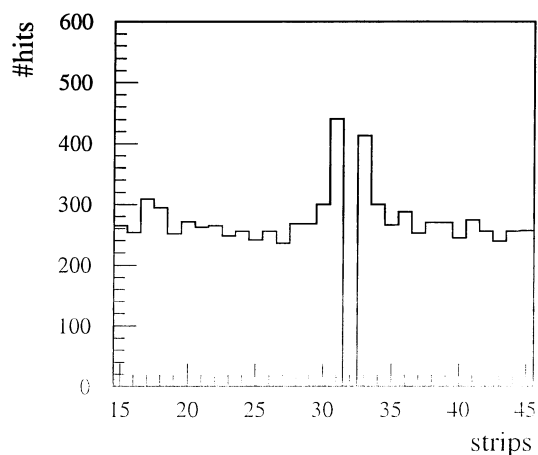


Figure 6.18: Effect of Fig. 6.17 on detection efficiency: When one strip is broken, electrons get 'redirected' to the neighbouring anode. Thus, spatial resolution is slightly affected but all all particles are detected.

parallel with the rod. A change of pressure over time (on the order of minutes) would reveal leaks in the rod.

#### Integrity of electrical connections.

The electrical components are tested by ramping up the high voltage of the chambers to the operating point irradiating the chambers with a radioactive source mounted on motorised arms similar to the mechanism used for the XY-Table, and seeing whether the recorded data reflects the pattern.

### 6.3.2 Alignment Capabilities of the Rod Test Stand

The horizontal alignment, i.e. a shift of a chamber vertical to the carbon beams of the rod and a rotation of the chamber in the plane defined by the two beams (Fig. 6.20), can be measured by using the radioactive source as well. Measurements with the XY-Table (Fig. 6.21) have shown that the centre of gravity of the distribution of hits from the  $\text{Sr}^{90}$  source can be located with a precision of better than 0.06 strips, i.e.  $\sim 12 \mu\text{m}$ . Thus, taking into account the uncertainty in alignment of the rod with respect to the testing equipment, on the order of  $\sim 10 \mu\text{m}$ , and the precision of the mechanical source positioning,  $\sim 5 \mu\text{m}$ , the position of the MSGC chambers in the direction orthogonal to the main axis of the rod can be determined with a precision better than  $20 \mu\text{m}$ .

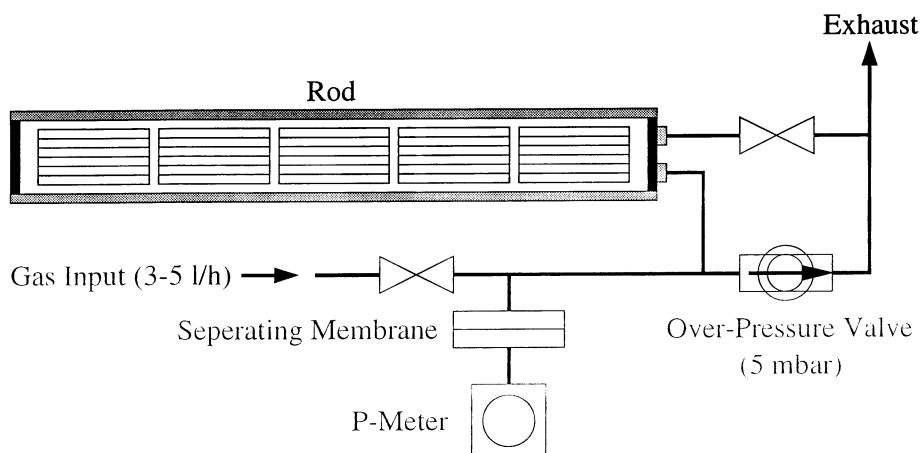


Figure 6.19: The measurement of the rod impedance is done by applying a well defined gas flow and measuring the resulting pressure. An over-pressure valve serves as a safety device.

The position of the MSGC modules in the direction along the rod can similarly be determined for double modules which are assembled in the small angle stereo configuration. For modules with one dimensional position readout, on the other hand, precise alignment in that direction is not relevant, as these modules are not sensitive to that coordinate.

This measurements will give an intermediate level of precision of alignment, which will be complemented by a laser alignment of the rods with respect to the whole CMS architecture. The final alignment of the fully assembled tracker will make use of highly energetic tracks from particles originating in the LHC  $pp$  collisions.

## 6.4 Pulsing

Pulsing is a testing method currently implemented on the XY-Table but can be regarded as a stand-alone technique, useful for quality assurance, online monitoring and calibration of MSGCs. Fig. 6.22 illustrates the working principle, Fig. 6.23 shows its realization on the XY-Table. There, each chamber is mounted on a Vetronite frame to simplify the handling. Onto this support a 1.5  $cm$  wide copper strip is glued, running at 90 degrees angle to the micro-pattern strips, in a distance of  $\sim 6 mm$  to the strips. A NIM pulse (0.8 V,  $\sim 4 ns$  rise time) is injected. By capacitive coupling, a signal is induced on the strips, which are read out in synchronisation with the strips.



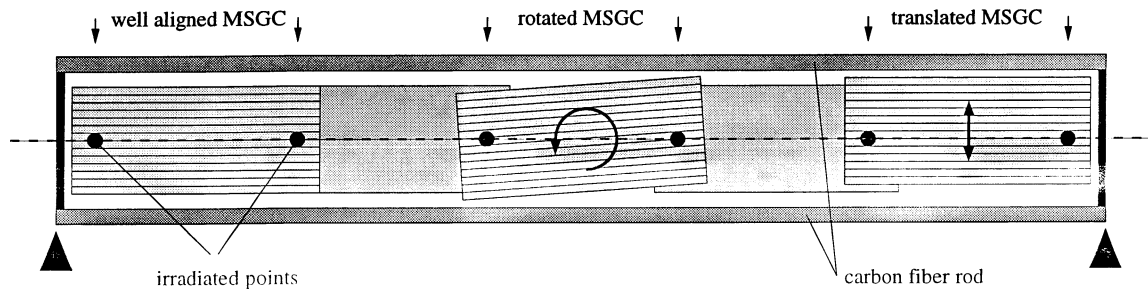


Figure 6.20: Schematic layout of the alignment measurement performed with the Rod test stand. Translation and rotation of the coordinates of each chamber with respect of the rod can be determined.

The response of a chamber to pulsing is shown in Fig. 6.24a and b. Sending a NIM pulse into the pulsing strip induces a signal with an average of around 600 ADC values, fluctuating only by  $< 6$  ADC counts (Fig. 6.26), which includes the electronics noise, typically around 5 ADC counts (e.g. Fig. 6.12).

When a strip is interrupted somewhere along its length the charge collected on its cut-off part is not read out and does not contribute to the measured signal. Therefore, comparing the pedestals from the data taken with the pulser reveals defects in the chamber (Fig. 6.25). Thus, the position of the interruption can be determined assuming a uniform gain of all 512 read out channels. Using data obtained with the XY-Table, one does not even have to rely on this assumption, as the gain of each strip/pre-amplifier can actually be measured (Fig. 6.13). Thus, the position of interruption can be determined with a precision of a few percent of the total strip length, i.e. to better than 2 cm, which is a valuable input to the track recognition algorithms of the CMS tracker.

#### 6.4.1 Calibration of the Read-out Electronics

In order to disentangle the gain of the read-out electronics from the gas gain of the MSGC, it is important to know the conversion factor between charge at the input of the pre-amplifier and the ADC value at the output of the whole readout chain. Pulsing can be used to determine this factor, as every pulse injects a well defined amount of

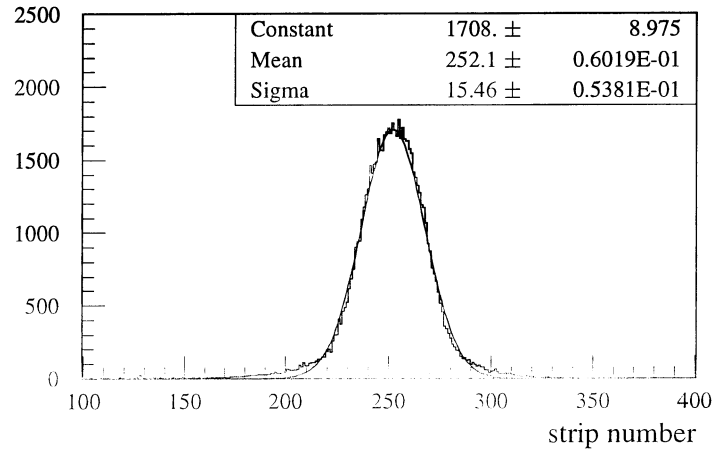


Figure 6.21: Spatial extension of the area irradiated by the  $\text{Sr}^{90}$  source as measured by the MSGC. 100k triggered events show a Gaussian distribution of the emitted particles whose centre of gravity can be determined with a precision of 0.00 strips, i.e.  $\sim 12\mu\text{m}$ .

charge into each pre-amplifier, which is then read out as

$$ADC = k \cdot C_{PS} \cdot V_{in}. \quad (6.1)$$

Knowing the pulse shape at the input of the pulsing strip, the only unknown is the capacitance formed by the pulsing strip and the anode strips,  $C_{PS}$  in Fig. 6.22.

In order to determine  $C_{PS}$ , we put an external capacitance  $C_E$  in series with the strip, as shown in Fig. 6.27. Now Eq. 6.1 must read

$$ADC = k \cdot C_{tot} \cdot V_{in}, \quad \text{with } C_{tot} = \frac{1}{\frac{1}{C_E} + \frac{1}{C_{PS}}}. \quad (6.2)$$

By using different values for  $C_E$  different amounts of charge are injected into the pre-amplifiers and we obtain the curve Fig. 6.28 from which we can determine  $C_{PS}$  and a calibration constant  $k$ . It has to be noted, however, that the value for  $k$  is *not* the conversion factor between electrons collected by a strip and the corresponding ADC output, but is only proportional to it. This is due to the fact that in the current setup the charge is injected as a delta pulse and does not reflect the convolution between arrival time and cluster size distribution of a real signal. Thus the charge collection time and the different reduction of charge visible to the ADC due to shaping (the ballistic deficit) are not taken into account.

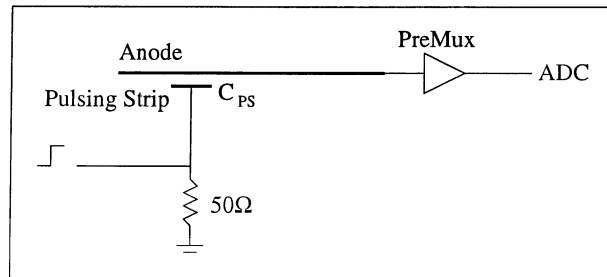


Figure 6.22: Pulsing of an anode strip shown in a simplified schematic diagram. A pulsing strip mounted close to the anode strips forms a capacitance  $C_{PS}$  with the strips. Thus, feeding an electric pulse to the pulsing strip induces a signal on the anode strips which is sensed by the read-out electronics.

## 6.5 Summary of Calibration

The 5540 barrel MSGC modules will be assembled and tested in several centres in Europe, including CERN, before being aligned in the CMS tracker structure at CERN. Collection of the data produced by the various test stations is not an easy task. The Cristal database system developed at CERN [60] will be adapted for the CMS tracker to overlook and coordinate the work flow and store all the analysed data from the testing and calibration systems described above.

Once all the modules and rods have been tested, a subset of this data will be extracted from the database and used for the online event reconstruction. Summarizing, the contributions of the test setups to the online calibration system of the CMS tracker are:

- ) Cosmics setup:
  - leakage currents for different voltage settings,
  - current spike rate for different voltage settings.
- ) XY-table :
  - position of broken and noisy strips, signal-to-noise of each strip,
  - gain as a function of  $V_{cathode}$  and  $V_{drift}$ .
- ) Rod test stand :
  - identification of the modules on each rod,
  - alignment of each module on the rod.
- ) Pulsing :
  - Charge-to-ADC conversion factors of the read-out electronics for each strip.

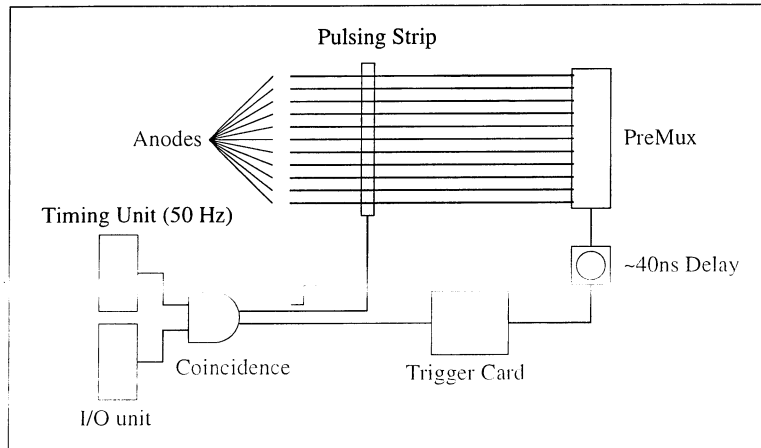


Figure 6.23: Block diagram of the pulsing setup. A 1.5 cm wide copper strip orthogonal to the 512 anode strips is pulsed. The read-out of the strips is synchronised to the pulsing.

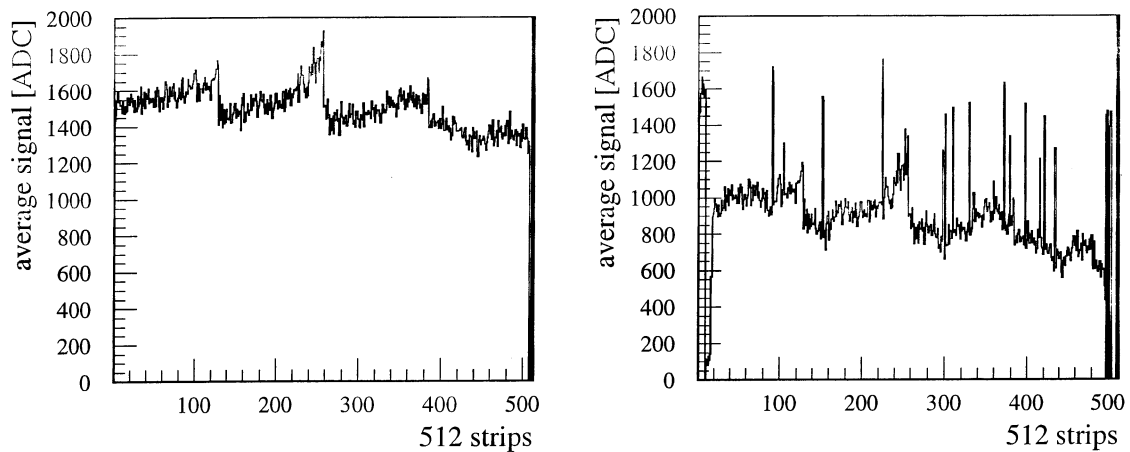


Figure 6.24: Response of strips to pulsing. (a) shows the pedestal of each strip, (b) shows the average response of each strip to a NIM pulse.

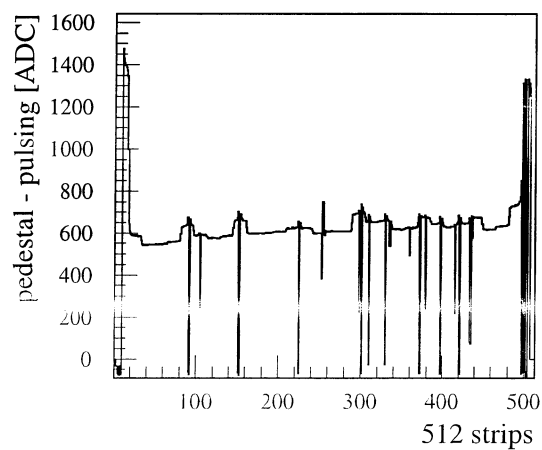


Figure 6.25: Detection of non-functioning strips through pulsing. The figure shows the subtraction of (b) from (a) of Fig. 6.24. Broken strips, i.e. strips that do not pick up a signal are clearly visible.

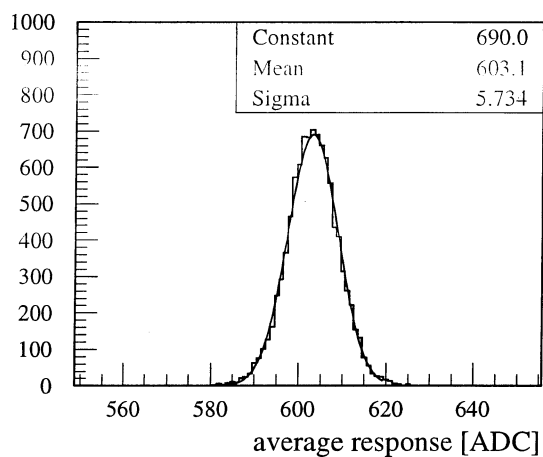


Figure 6.26: Pulse height distribution. A signal of a typical strip when pulsed is  $\sim 600$  ADC counts after pedestal subtraction, with only a 1% fluctuation, mainly due to the intrinsic noise of the strip/pre-amplifier combination.

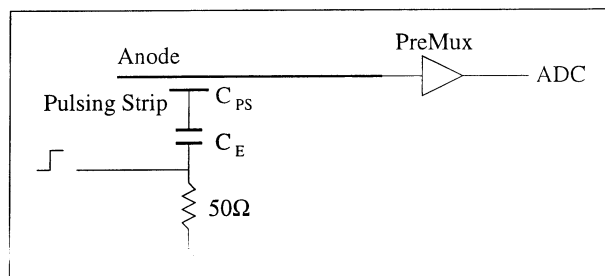


Figure 6.27: Calibration of the pulsing setup. A variable external capacitance  $C_E$  is connected in series with the pulsing strip (cf. Fig. 6.22).

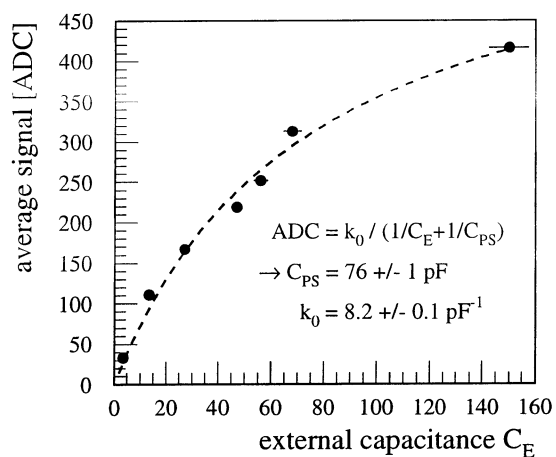


Figure 6.28: Calibration of the read-out electronics. The strip-signal varies with the external capacitance  $C_E$  according to Eq. 6.2. A fit allows to determine  $C_{PS}$ .

# Chapter 7

## Conclusions

Development for the Microstrip Gas Chambers for CMS has been going on for several years by now. During the last two years chambers have been tested in the laboratory and several test-beams, and a technology was established that looks promising for application in the challenging radiation environment at LHC.

These MSGCs feature gold strips on a glass substrate of  $10 \times 25 \text{ cm}^2$  which are 7 and 93  $\mu\text{m}$  wide, for anodes and cathodes, respectively. Using the effect of electron diffusion in the 3 mm gas gap, a resolution of  $\sim 30 \mu\text{m}$  can be obtained.

The choice of a gas mixture Ne/DME in the ratio 40:60 allows to obtain a gain of  $\sim 2000$  at a moderate operating point of ( $V_{cathode} = -520 \text{ V}$ ,  $V_{drift} = -3500 \text{ V}$ ), while sufficiently quenching UV-photons. At this operating point, the signal-to-noise ratio with a read out electronics that is fast enough to disentangle the 25 ns bunch crossings of LHC is such that the maximum efficiency of  $\sim 98\%$  is guaranteed.

Of highest concern is the survivability of this delicate detector technology under the high particle flux that will be present in the region of the CMS tracker during operation. Overcoating the MSGC substrate with a thin layer of semiconductive glass and 'passivating' all the edges of the micro pattern structure with polyimide allows to significantly stretch the domain in which discharge free operation in a high rate heavily ionising environment is possible.

Tests in beams with a particle spectrum comparable to what is expected from the LHC pp-collisions have been performed. Extrapolating the obtained results to a 10 year long operation of the MSGCs in CMS, the amount of strips damaged during this time should not exceed 8% of the total number of strips. Whether the amount is even

less than the 2% necessary to obtain optimal tracker performance will be explored by a further beam test end of 1999.

A good performance of the MSGC tracker containing over 5000 modules can only be obtained with a rigorous quality testing and calibration setup, that is able to investigate all the relevant operating parameters of each single MSGC.

A Cosmics Rack has been designed and is being set up test the robustness of the chambers to high voltages at and beyond the nominal operating point, and detects eventual gas leaks of the modules.

A fully automated XY-Table was constructed which allows to measure the gain of each single strip of a module, thereby detecting broken strips, noisy electronics channels and non-uniform behaviour of the chamber to a precision of a few percent. This information will be used by the track reconstruction algorithms of the CMS tracker in order to assign appropriate weights to the track points measured by the single MSGCs.

A Rod Test Stand is currently being assembled that allows to determine the integrity of the barrel 'rods' – the superstructures that combine several MSGC modules. This station, besides checking the quality of the electrical and gas connections among the modules, measured the exact position of each module with respect to the rod with a precision better than  $20 \mu m$ . This information will be used for obtaining a precise three dimensional picture of where the single modules are located once the CMS tracker is assembled.

In the year 2000 mass production of the Microstrip Gas Chambers will start, and the above chain of sophisticated test benches will try to add its little share to the exciting preparations for the effort to gain understanding in the origin of mass.



# Chapter 8

## Acknowledgements

Within the Doctoral Students Program I had the chance to spend 2 1/2 years entirely at CERN. My supervisor at my home university in Vienna, Prof. Hille, was very kind to accept me as his student and made it possible for me to gain experience in an exciting international research environment. Thank you!

It happened when I met Ariella Cattai that I felt that she should be the person to shout at me whenever I would do something semi-intelligent. And indeed, it was the right choice and being the boss of the group I had the pleasure to work in she had a lot of opportunities to do so. She took an active part in guiding me through the wonderland of detector development and testing and I owe her my deepest gratitude.

'The Boss' Luigi Rolandi took a lot of interest in my work and his questions that always made me very nervous were certainly a big help in making me better understand the intricacies of gaseous detectors.

A big thank you goes to Machi Tsirou for her many encouraging words during endless days of despair and evil that often turned out to be due to a cable I had plugged into the wrong place and to Marco Bozzo of whose broad experience in physics I could profit many times.

Merci beaucoup! to Christiane Bastie and Jean Martin for their help in all mechanical and electrical aspects, from domesticating the wildest 30-pin plugs to providing me with the most refined metallic blue aluminium plate.

I will not forget the numerous wonderful people I met in- and outside CERN, and to Luca I say "Thank you for your friendship".

This thesis is dedicated to my parents who through a quarter of a century brought me up with love and incomprehensible patience and never gave up the hope that maybe one day their son will learn to read and write.

# Appendix A

## Appendix

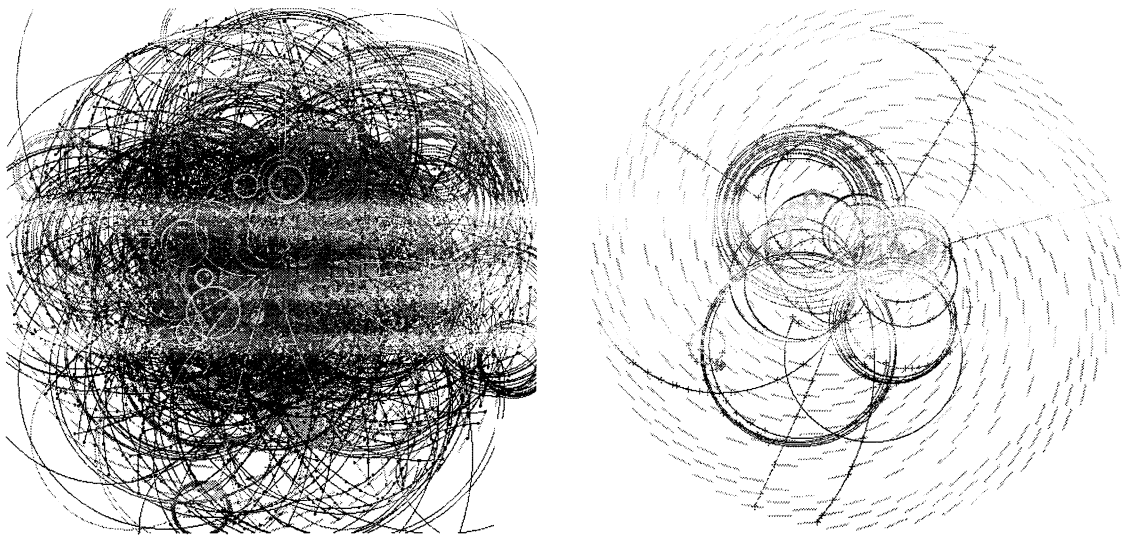


Figure A.1: One simulated LHC bunch crossing as seen by the inner tracker of CMS. (a) shows all particle tracks of 20 minimum bias events which are created on average in one bunch crossing. (b) shows a single event,  $H \rightarrow 4\mu$  decay.

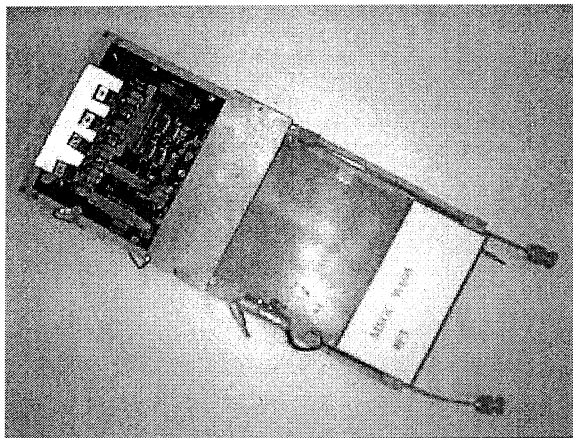


Figure A.2:  $10 \times 10 \text{ cm}^2$  MSGC prototype with Premux electronics.

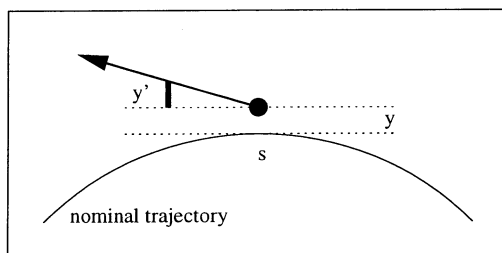


Figure A.3: A particle in an accelerator can be described at any position  $s$  along the nominal beam trajectory by its transverse distance  $y$  from that trajectory and its direction  $y'$  with respect to the latter.

## A.1 Accelerator Physics

### A.1.1 The beta function $\beta(s)$

The transfer matrix  $M$ , which allows to calculate the distance and relative motion  $(y, y')$  of a particle from the nominal orbit at an arbitrary point  $s$  on the orbit (see Fig. A.3) given the respective initial values  $(y_0, y'_0)$  at  $s_0$ ,  $(y, y') = M(s - s_0) \cdot (y_0, y'_0)$ , can be parametrized with only one real valued  $s$ -dependent function, the beta function. It can be shown that wherever the beam envelope has a local minimum or maximum, the beta function is just the ratio of beam size to beam divergence. Since  $\beta$  is typically on the order of  $m$ , a beam of  $\sim mm$  diameter will have a divergence of  $\sim mrad$ .

### A.1.2 The emittance $\epsilon$

At any point  $s$ ,  $(y, y')$  (Fig. A.3) lies on an ellipsis  $ay^2 + 2byy' + cy'^2 = \epsilon$  with  $a, b, c$  defined by the tuning of the beam. Thus, the so-called emittance  $\epsilon$  is the area/ $\pi$  of this ellipsis, and is constant along the whole beam trajectory due to Liouville's theorem of the incompressibility of phase-space. As an accelerator habitually accelerates more than one particle at a time, a suitably average over all  $\epsilon$ 's is chosen to define the average area, i.e. the 'collimatedness', of the beam.

When particles are accelerated, the emittance decreases inversely proportional to the momentum. This is called adiabatic damping. In this case, the *normalized emittance*  $\epsilon_N = \left(\frac{E}{m}\right) \epsilon$  is the invariant of interest.

## A.2 Minimum gain required for MSGC's in CMS

The following is adapted from a calculation done by [61].

Different sources contribute to the Equivalent Noise Charge *ENC*:

$$N_{total} = \sqrt{N_{series}^2 + N_{amp}^2}, \quad (\text{A.1})$$

where  $N_{amp}$  is the noise from the preamplifier and capacitance noise,  $N_{amp} = 450 + 45 \text{ e}^- / pF = 720 \text{ e}^-$ , where we used  $C_{det} = 6 \text{ pF}$ .  $N_{series}$  denotes the "series" noise,

$$N_{series}^2 = 4kTR_{strip}C_{det}^2 \frac{e^2}{8\tau}. \quad (\text{A.2})$$

With  $R_{strip} = 500 \Omega$  and  $\tau = 50 \text{ ns}$  we obtain  $N_{series} = 264 \text{ e}^-$ , and thus

$$N_{total} = 767 \text{ e}^-. \quad (\text{A.3})$$

Deconvolution further increases the noise per strip by a factor  $\sqrt{2}$ . With a cluster size of 1.6 after deconvolution [62] we thus obtain for the cluster noise

$$N_{cluster} = 1.6 \times \sqrt{2} \times 767 = 1372 \text{ e}^-. \quad (\text{A.4})$$

This requires a signal  $S = 27440 \text{ e}^-$  in order to have a  $S/N = 20$ . Two factors decreasing the signal strength are a crosstalk of 6% between strips and thus 9.6% per cluster<sup>1</sup> and the ballistic deficit due to the finite integration time of the electronics,

---

<sup>1</sup>16 cathodes are grouped together, thus,  $1/16^{th}$  of the current needed to generate the signal is 'borrowed' from each cathode, inducing a signal of opposite sign on the corresponding anodes.

reducing the signal by a factor 0.65.

We thus have to require a total of  $27440 \times 1.096 \times 1/0.65$   $e^-$  per avalanche produced by each traversing particle. With  $\sim 40$   $e^-$  of primary ionization this requires a gain of 1172. Introducing a safety factor of  $\sqrt{2}$  for optical link and digitization noise as well as gain variations and possible not yet identified sources of noise we require a gain of  $\sqrt{2} \times 1172 \approx 1600$  for the MSGC.

### A.3 The over-pressure valve

The MSGC modules used in CMS are built on a  $300 \mu m$  thin glass substrate which covers an area of  $10 \times 25 \text{ cm}^2$ . This substrate is very delicate and should not be exposed to sudden mechanical deformations as can be induced by pressure differences between the gas volume enclosed by the MSGC and the outside world. Already a small  $\Delta p$  of a few  $10 \text{ mbar}$  can be sufficient to break a chamber.

Thus, extreme care has to be taken that a gas system that supplies MSGC modules does not create the danger of destroying the chambers with pressure bursts. Also, mechanical mis-manipulation, like accidental blocking of the gas-outlet of an MSGC module should not damage the chamber. Such a security device must not depend on computer programs or even electricity but must work autonomously.

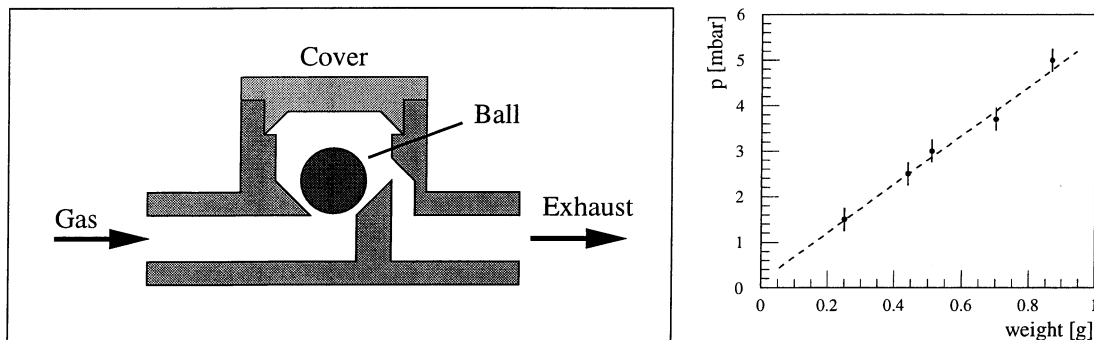


Figure A.4: The over-pressure valve (a). A steel ball closes the connection between the gas in- and output under its own weight of  $\sim 1 \text{ g}$ , acting against the gas pressure at the input. By changing the size, i.e. the weight of the ball, the point at which the valve opens can be changed. The maximum sensitivity is as low as  $2 \text{ mbar}$  (b).

Fig. A.4 shows the simple and fail-safe solution to the above problem. A ball of a few  $mm$  in diameter closes a conical hole. When gas overpressure and gravitational pull on

the ball become equal, the hole opens and the gas can escape. By varying the density and the size of the ball, this release point can be regulated. Pressure thresholds as low as 1 *mbar* can be reached. Advantages of this system over appropriate pressure disks are the infinite reusability, simplicity and no need of (re-)calibration of the device.

#### A.4 Gain Dependence on $V_{cathode}$ and $V_{drift}$

Measurements referred to in chapter 5.5 taken on an MSGC prototype are summarized here. The chamber itself and the DAQ procedure have already been described in that chapter. The gain of the chamber was determined for different drift- and cathode voltages in a number of different Ne/DME concentrations.

△ $V_D = 3000$ V	★ $V_C = 640$ V
□ $V_D = 2600$ V	⊕ $V_C = 620$ V
○ $V_D = 2200$ V	◇ $V_C = 600$ V
▼ $V_D = 1800$ V	△ $V_C = 580$ V
▲ $V_D = 1400$ V	□ $V_C = 560$ V
■ $V_D = 1000$ V	○ $V_C = 540$ V
	▼ $V_C = 520$ V
	▲ $V_C = 500$ V
	■ $V_C = 480$ V

Figure A.5: Legend for Fig. 5.14, A.6 and A.7

The legend explaining the various symbols is shown in Fig. A.5). The figures for the mixture Ne/DME=33/67 (Fig. 5.14) have already been shown in the text (chapter 5.5).

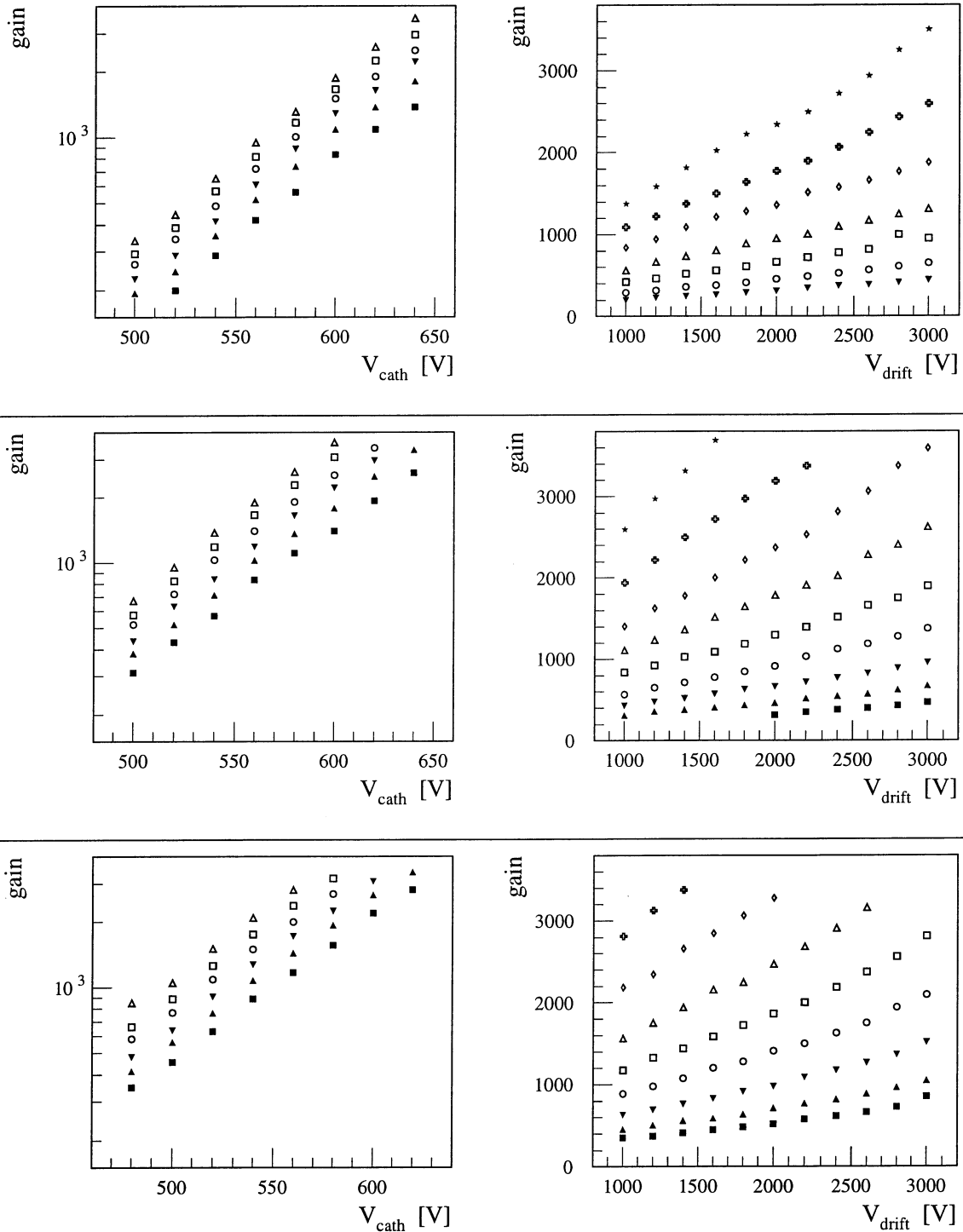


Figure A.6: Gain in Ne/DME mixtures with Ne=25, 42 and 50 %, respectively.

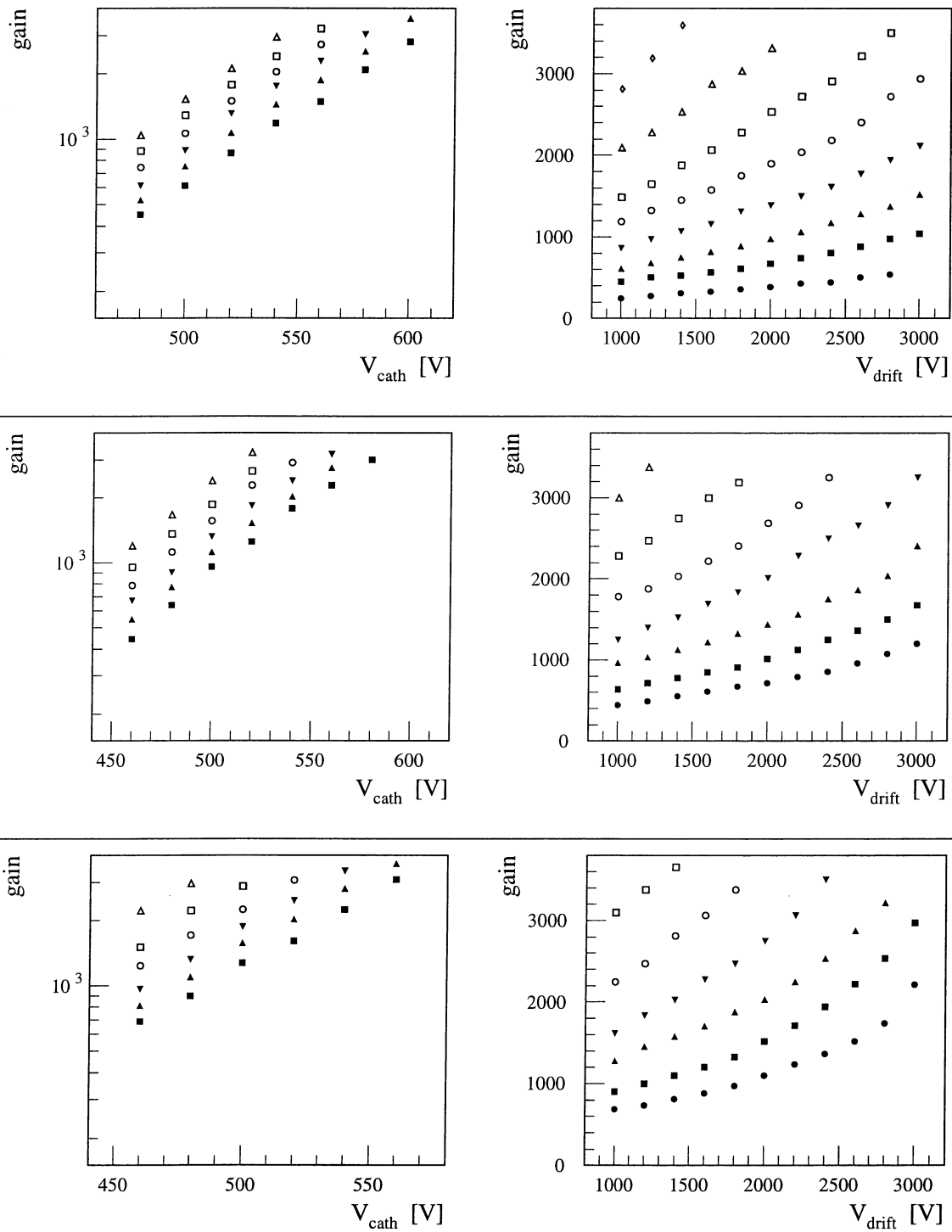


Figure A.7: Gain in Ne/DME mixtures with Ne=58, 67 and 75 %, respectively.



# Bibliography

- [1] S. L. Glashow. Partial-Symmetries of Weak Interactions. *Nucl. Phys.*, 22:579, 1961.
- [2] S. Weinberg. A Model of Leptons. *Phys. Rev. Lett.*, 19:1264, 1967.
- [3] C. Itzykson and J.-B. Zuber. *Quantum Field Theory*. McGraw-Hill, 1985.
- [4] F. Abe et al. Observation of Top Quark Production in  $\bar{p}p$  Collisions with the CDF Detector at Fermilab. *Fermilab-Pub-95*, 022-E, 1995.
- [5] S. Abachi et al. Observation of the Top Quark. *Fermilab-Pub-95*, 028-E, 1995.
- [6] J. Womersley. The LHC Physics Program. *FERMILAB-Conf*, 97/350, 1997.
- [7] M. Kobayashi and T. Maskawa. CP-Violation in the Renormalizable Theory of Weak Interactions. *Prog. Theo. Phys.*, 49:652, 1973.
- [8] L.-L. Chau and W.-Y. Keung. Comments on the Parametrization of the Kobayashi-Maskawa Matrix. *Phys. Rev. Lett.*, 53:1802, 1984.
- [9] A.C. Longhitano. Low-energy Impact of a Heavy Higgs Boson Sector. *Nucl. Phys.*, B188:118, 1981.
- [10] E. Farhi and L. Susskind. Technicolour. *Physics Reports*, 74 No.3:277, 1981.
- [11] S. Spira et al. Higgs Boson Production at the LHC. *CERN TH/95-30*, 1995.
- [12] R.M. Barnett et al. Review of particle physics. *Phys. Rev.*, D55:225, 1996.
- [13] *CMS – Technical Proposal*. CERN LHCC/94-43, 1994.
- [14] D. Denegri. The CMS Detector and Physics at the LHC. *CERN-PPE*, 1995-183, 1995.

- [15] H. E. Haber. The Status of the Minimal Supersymmetric Standard Model and Beyond. *hep-ph*, 9709450, 1997.
- [16] J. Wess and J. A. Bagger. *Supersymmetry and Supergravity*. Princeton Univ. Press, 1992.
- [17] R. Kinnunen and D. Denegri. Expected SM/SUSY Higgs Observability in CMS. *CMS Note*, 1997/57, 1997.
- [18] R. Hagedorn and J. M. Rafelski. Hot Hadronic Matter and Nuclear Collisions. *Phys. Lett.*, 97B:136, 1980.
- [19] M. Bedjidian et al. Physics With Heavy Ions in CMS. *CERN*, CMS TN 92/33, 1992.
- [20] F. Karsch. Heavy Quark Resonances in Heavy Ion Collisions: From SPS to LHC. *Proc. LHC Workshop, Aachen*, CERN 90/10, vol.II:1141, 1990.
- [21] J.D. Cockroft and E.T.S. Walton. Experiments With High Velocity Ions. *Proc. Royal Soc.*, Series A 136, 1932.
- [22] E.O. Lawrence and N.E. Edlefsen. *Science*, 78, 1929.
- [23] E.M. McMillan. The Synchrotron – A Proposed High-Energy Particle Accelerator. *Phys. Rev.*, Letter to the editor 68, 1945.
- [24] J. W. Goethe. *Faust I*.
- [25] E. Brouzet and K. Schindl. Heavy Ions in the LHC. *CERN SL/93-60*, 1993.
- [26] *The Large Hadron Collider – Conceptual Design*. CERN AS/95-05 (LHC), 1995.
- [27] A. Lienard. *L'Eclairage electrique*, 16, 1898.
- [28] D. Warner et al. CERN Heavy Ion Facility Design Report. *CERN 93-01*, 1993.
- [29] *ATLAS – Technical Proposal*. CERN LHCC/94-38, 1994.
- [30] *LHCb – Technical Proposal*. CERN LHCC/98-4, 1998.
- [31] *ALICE – Technical Proposal*. CERN LHCC/95-71, 1995.
- [32] *The Tracker Project – Technical Design Report*. CERN LHCC/98-6, 1998.

- [33] *The Electromagnetic Calorimeter Project – Technical Design Report.* CERN LHCC/97-33, 1997.
- [34] *The Hadron Calorimeter Project – Technical Design Report.* CERN LHCC/97-31, 1997.
- [35] *The Muon Project – Technical Design Report.* CERN LHCC/97-32, 1997.
- [36] *The Magnet Project – Technical Design Report.* CERN LHCC/97-10, 1997.
- [37] G. Charpak et al. The Use of Multiwire Proportional Counters to Select and Localize Charged Particles. *Nucl. Instr. Meth.*, 62:262, 1968.
- [38] G. Petersen G. Charpak, G. Melchart and F. Sauli. High-Accuracy Localization of Minimum Ionizing Particles Using the Cathode-Induced Charge Centre-of-Gravity Read-Out. *Nucl. Instr. Meth.*, 167:455, 1979.
- [39] A. Oed. Photon-Sensitive Detector With Microstrip Anode for Electron Multiplication With Gases. *Nucl. Instr. Meth.*, A263:351, 1988.
- [40] H. Fischle, J. Heintze, and B. Schmidt. Experimental Determination of Ionization Cluster Size Distributions in Counting Gases. *Nucl. Instr. Meth.*, A301:202, 1991.
- [41] L. D. Landau. On the Energy Loss of Fast Particles by Ionization. *J. Phys USSR*, 8:201, 1944.
- [42] B. Rossi. *High Energy Particles.* Prentice-Hall, Inc., Englewood Cliffs, NJ, 1952.
- [43] L. G. Christophorou. *Atomic and Molecular Radiation Physics.* Wiley & Sons, 1971.
- [44] W. Blum and L. Rolandi. *Particle Detection with Drift Chambers.* Springer Verlag, 1994.
- [45] W. Diethorn. A Methane Proportional Counter System for Natural Radiocarbon Measurements. *USAEC Report*, NY06628, 1956.
- [46] R. Veenhof. Garfield, a Drift Chamber Simulation Program, 1997. <http://consult.cern.ch/writeups/garfield/main.html>.
- [47] F. Angelini et al. Operation of MSGC's with Gold Strips Built on Surface-Treated Thin Glasses. *Nucl. Instr. Meth.*, A382:461, 1996.

- [48] R. Bellazzini et al. Technique for the Characterization of Discharges in Micro-Strip Gas Chambers. *Nucl. Instr. Meth.*, A398:426, 1997.
- [49] Y.-X. Wang and G. Godfrey. Study of Dimethyl Ether for Limited Streamer Tubes. *Nucl. Instr. Meth.*, A320:238, 1992.
- [50] GDD group. Study of Materials Outgassing. *CERN-PPE-GDD*, 1996.
- [51] F. G. Sciacca. Analog Readout and Signal Processing for MSGC's of the CMS at LHC. *Imperial College Ph.D. thesis*, CERN, 1999.
- [52] F. G. Sciacca. Readout of an MSGC Prototype with the APV6 Front End Chip. *CMS Note*, 98-093, 1998.
- [53] G. Klaus et al. Strip Detector Read-Out System User's Guide. *CRN, LEPSI Strasbourg, France*, 96-33, 1996.
- [54] A. Mugnai. Finite Element Analysis and Experimental Tests of a Barrel MSGC. *CMS Technical Note*, 96-004, 1996.
- [55] S. Gadomski et al. The Deconvolution Method for Fast Pulse Shaping at Hadron Colliders. *Nucl. Instr. Meth.*, A320:217, 1992.
- [56] F. G. Sciacca. Definition of the Front-end Signal Processing Algorithm for MSGC's in CMS. *CMS Internal Note*, 97-021, 1997.
- [57] E. Albert et al. Performance of a Prototype of the MSGC's for the CMS Experiment at LHC. *Nucl. Instr. Meth.*, A409:70, 1998.
- [58] M. Bozzo, A. Cattai, and A. Tsirou. Tests on MSGC with Advanced Passivation, 1997. <http://cmsdoc.cern.ch/~cattai/alpha/alpha.html>.
- [59] M. Huhtinen. Factors to Scale Highly Ionizing Particle Rates in MSGC Irradiation Tests to the LHC Environment. *CMS Note*, 97-073, 1997.
- [60] A. Bazon et al. The Use of Production Management Techniques in the Construction of Large Scale Physics Detectors. *IEEE Transactions in Nuclear Science in Press*, NSS'98, Toronto, 1998.
- [61] G. Hall. Noise and Gain Evaluation in MSGC's for CMS for a CR-RC Shaping. *MSGC meeting*, CERN, Oct., 1996.
- [62] F. Angelini et al. Study of the Bunch Crossing Identification at LHC Using Microstrip Gas Chambers. *CMS Technical Note*, 95-048, 1995.

## Curriculum Vitae

16.5.1973	born in Vienna
9/1979-6/1983	Primary school, 1130 Vienna
9/1983-6/1991	humanistisches Gymnasium (high school) Wasagasse, 1090 Wien (Greek, Latin; French as option) final exam: 'mit Auszeichnung' (excellent success).
10/1991-12/1996	Study of physics and mathematics at the university of Vienna.
Summer 1994	10 Weeks 'Summer Student' at CERN in the NA44 experiment.
10/1995-12/1996	Diploma thesis on experimental particle physics within the NA44 experiment at CERN. Title: "A New Twist on Particle Correlation".
12/1996	Graduation as 'Mag. rer. nat.' in Physics 'mit Auszeichnung' (excellent success).
1/1997-6/1999	'Doctoral Student' in the CMS experiment at CERN. Ph.D. thesis on detector technologies in elementary particle physics. Envisaged graduation: June 1999.